MODELING THE NONLINEAR ACTIVE COCHLEA:

MATHEMATICS AND ANALOG VLSI

Bo Wen

A DISSERTATION

in

Bioengineering

Presented to the Faculties of the University of Pennsylvania in Partial

Fulfillment of the Requirements for the Degree of Doctor of Philosophy

2006

Kwabena A. Boahen,	Christopher Chen,
Supervisor of Dissertation	Graduate Group Chair

Acknowledgements

This dissertation would not have been possible without the help from many individuals. I would like to acknowledge all of the people who in their own way helped and supported me with the present work.

I am truly indebted to my thesis advisor, Kwabena Boahen, for his outstanding guidance, encouragement, and support, throughout the course of this work. I am grateful for his accepting me in his laboratory, which has opened a door to many exciting opportunities for my career. His exhortations of “develop your intuition” and “keep the faith” are what I will always bear in mind in my future research.

I would like to express my deep appreciation to my thesis committee members, James Saunders, Jan Van der Spiegel, and Daniel Bogen, for their insightful and constructive advice throughout my doctoral studies. I am especially grateful to James Saunders for his continuing encouragement in my career development.

I sincerely thank Elizabeth Olson at Columbia University, Michael Anne Gratton and Virginia Richards at Penn, Paul Fahey at the University of Scranton, for their invaluable suggestions and discussions with my study in the cochlear mechanics.

Special thanks go to my lab fellows, Kareem Zaghloul, Kai Hynna, Brian Taba, John Arthur, Paul Merolla, John Wittig, Rodrigo Alvarez, and Joseph Lin, who helped create an intellectually stimulating and fostering environment. Their companionship has helped make this endeavor enjoyable and rewarding.

I would like to thank my parents for their continuing love and support during my pursuit of a doctoral degree. Finally, I thank my husband, Xinyu Liu, for his positive impact on me by his curiosity and interest in science and engineering, for his belief in me for reaching my research goal, and for his unconditional love and encouragement, before and during our years at Penn.

Abstract

MODELING THE NONLINEAR ACTIVE COCHLEA:

MATHEMATICS AND ANALOG VLSI

Bo Wen

Supervisor: Kwabena A. Boahen

The human auditory system vastly outperforms any machine in efficiency and robustness in perceiving sound. Complex and delicate, its front end, namely the cochlea, senses and processes sound in a nonlinear active fashion, exhibiting remarkable sensitivity and extraordinary frequency discrimination. The mechanism through which the mammalian cochlea achieves its incredible capability is postulated as the cochlear amplifier, which is generally believed to originate from outer hair cells electromotility. However, the detail of the cochlear amplifier remains unclear.

Using both analytic and synthetic approaches, the present work provided a plausible basis for realization of the cochlear amplifier, thus advancing our understanding of cochlear mechanics. We proposed a novel cochlear amplifier mechanism based on the cochlea's microanatomy, as well as outer hair cell (OHC) motility, to account for the cochlea's characteristic behavior. This mechanism, active bidirectional coupling (ABC), considers both the basal tilt of OHCs and the apical tilt of phalangeal processes as critical for feeding OHC motile forces (with saturating property) forward and backward onto the basilar membrane, thereby enhancing the cochlea's functioning. The ABC-based mathematical cochlear model produces responses that are comparable to physiological measurements. Theoretical model analysis reveals that ABC leads to negative damping basal to the response peak over a small longitudinal cochlear region. The tilted structure works as a

spatial filter, amplifying the cochlear traveling wave only when its wavelength becomes comparable to the tilt distance.

Inspired by the biology, we proceeded to build a nonlinear active silicon cochlea—a very large scale integration (VLSI) physical cochlear model—for achieving real-time low-power cochlear processing. Designed in current mode and operating in Class AB, this microchip implements the ABC mechanism, together with a silicon auditory nerve, in 0.25 μm complementary metal-oxide-semiconductor (CMOS) technology. The resultant new architecture addresses the shortcomings of existing silicon cochleae, filter banks in cascade and in parallel. Analog current representing the basilar membrane's velocity drives the silicon auditory nerve, which encodes sound in digital pulses, mimicking neuronal spikes, as the final output of the cochlea.

Contents

List of Tables

List of Figures

Chapter 1

Introduction

The human auditory system exhibits extraordinary ability in sensing sound, distinguishing frequencies, and maintaining satisfactory performance in adverse environments. Its front-end, the cochlea, converts fluid pressure fluctuations into neuronal spikes in the auditory nerve, decomposing the mixture of frequencies, amplifying low-level sound, compressing high-level sound, and producing interferences between different frequencies. For decades, engineers have made efforts to build a hearing machine or computer that can emulate the function and efficiency of the cochlea and the human auditory system. However, no engineered device to date is capable of performing as well as its biological counterpart.

Neuromorphic engineers have taken an unconventional approach in which they reverse engineer the human brain, with the goal to morph or capture both the organization and the function of the nervous system. For about two decades, neuromorphic systems have modeled sensory systems, including the retina [1–4] and the cochlea [5–7], cortical functions, mainly including visual cortex [8, 9], developmental processes, based on axon guidance [10], and memory and learning [11, 12]. While artificial retinomorphic chips have

meticulously copied the detailed neuronal biophysics and complex synaptic organizations in the retina, the silicon cochleas have benefited relatively less from morphing the biology because the cochlear amplifier mechanism that accounts for the cochlea's characteristic behavior still remains a mystery.

Advances in physiological measurements and mathematical modeling in the past few decades have revealed the cochlear mechanics to a larger extent, through much is yet to be uncovered. In the mammalian cochlea, the non-uniform basilar membrane (BM) vibrates in response to fluid pressure, providing broad frequency tuning which is then enhanced and reshaped by the hypothesized cochlear amplifier. Bridging the gap between the dead cochlea's response and that of living cochleas, the postulated cochlear amplifier refers to the selective amplification process occuring within the cochlear partition that enhances active cochlear behavior: exquisite sensitivity, remarkable frequency selectivity, and nonlinearities. Thus, the BM preliminarily detects and filters sound signals and the cochlear amplifier selectively amplifies the BM's responses, resulting in nonlinear active cochlear behavior.

Since the discovery of outer hair cells' (OHCs) electromotility in mammalian cochlea [13, 14], cochlear modeling has been focusing on exploring the detailed manner in which OHCs' motile forces enhance the basilar membrane's vibration. The OHC forces can be transmitted, somehow through the complex organizations of the organ of Corti, onto the BM to affect its motion. Enormous modeling efforts have been made to incorporate the OHC motility in cochlear models, with differing hypotheses to account for the cochlear amplifier [15–17]. Responses to sound in most active models were either unrealistic [18] or missing important characteristic cochlear behaviors, for instance nonlinearity [15, 16].

Our project goal is to build a cochlear model, in mathematics and VLSI circuits, that can reproduce the major characteristic cochlear behavior, including the active amplification

and nonlinear compression. We proposed a novel cochlear amplifier mechanism that takes into account the cochlear micro-anatomy for transmitting OHC forces onto the BM. In this mechanism, two tilted structures transmit OHC motile forces in the basal and apical directions, respectively (namely, feedforward and feedbackward), onto the BM, resulting in active bidirectional coupling (ABC) among BM transverse fibers. We enforced saturation of ABC, which gives rise to nonlinear behavior. We proceeded to build a silicon cochlea based on this nonlinear active cochlear model; the cochlear chip is the first to include the model of cochlear amplifier mechanism, resulting in a novel silicon cochlea architecture that addresses problems of existing designs.

1.1 Organization of the Dissertation

The dissertation thesis is organized as follows. In Chapter 2, we review cochlear modeling efforts in both mathematical models and VLSI implementations. The review emphasizes the models that explore the underlying mechanism of active amplification in the cochlea. The content mainly encompasses the physiology of the cochlea including cochlear microanatomy, outer hair cell (OHC) motility, and mathematical models that incorporate OHC motility. This chapter also discusses advances in silicon cochlea designs and existing problems.

Chapter 3 is dedicated to presentation of our hypothesized cochlear amplifier mechanism, active bidirectional coupling (ABC). We describe unique features of the cochlear microanatomy that we believe play an essential role in manoeuvring OHC motile forces to enhance the cochlea's response gain and frequency tuning and to impart nonlinear processing to the cochlea. We formulate a two-dimensional (2D) nonlinear active cochlear model,

solve it numerically, and present the model's simulation results. Analysis of a linear version of the model follows, which provides insight into the mechanism underlying the selective amplification.

In Chapter 4, we present the silicon cochlea design that is based on our nonlinear active cochlear model. We present first the diffusive network for modeling the cochlear fluid, then the synthesis of the BM filter design. We proceed to describe the transistor-level circuit design of the BM. What follows is a silicon neuron circuit we have included in the silicon cochlea for modeling the spiral ganglion cells, which convert the BM motion to auditory nerve spikes. Last, we present the architecture of the entire cochlear chip.

In Chapter 5, we present chip responses to sound stimuli. The responses include both analog currents that represent the BM's velocity, and digital pulses that represent the auditory nerve's discharge patterns.

Chapter 6 summarizes our efforts in modeling the nonlinear active cochlea, discussing both the analytical and synthetical approaches.

1.2 Original Contribution of Present Work

The cochlear amplifier mechanism, active bidirectional coupling, is novel, the first to take account into the tilted structure of both OHCs and phalangeal processes in a cochlear model. The semi-analytical results of a linear version of the active cochlear model are novel, including the notion of a spatial filter and the negative damping caused by the tilts associated with delivery of outer hair cell motile forces.

The implementation of the nonlinear active cochlea model in analog VLSI is original. The differential mode (Class AB operation) is the first among silicon cochlea designs. The bio-inspired coupling between basilar membrane second-order sections is new, thus the novel architecture of the cochlear chip.

1.3 The Usage of "We"

The personal pronoun "we" is used in a number of places throughout the thesis—though in plural form, it is used with a singular sense. The present work was completed under the guidance of my thesis advisor. However, despite the usage of "we" and/or "our(s)", I performed 99% of the work, if not all, including model development and simulation, circuit design and simulation, and chip layout and test.

Chapter 2

The Cochlea and Cochlear Modeling

The human inner ear, namely the cochlea, functions as the front-end of the auditory system, turning outside-world sound signals into neural impulses transmitted along the auditory pathway for further processing. Complex and delicate, the cochlea does not just transduce mechanical sound into electrical impulses (all-or-none neural spikes); it also processes and amplifies sound by means of its unique structure and the physical properties of its comprising components. In this chapter, we first describe the cochlear anatomy and important findings about the cochlea's outer hair cells (OHCs) that make critical contributions to characteristic cochlear behavior. We then review previous mathematical cochlear modeling efforts. Last, we give a brief summary of existing cochlear models implemented in very large scale integration (VLSI) circuits.

2.1 The Cochlear

2.1.1 Cochlear Anatomy

The periphery of the auditory system includes the outer ear, the middle ear, and the inner ear (i.e., the cochlea) (sketched as in Figure 2.1). How is sound processed at each step of the auditory periphery? As the first steps of sound detection, the sound transmission in the outer and middle ear is basically linear [18]. In general, time-varying sound pressure in the air (condensation and rarefication) is transmitted through the ear canal of the outer ear. The basic role of the outer ear is to collect impinging sound waves and channel them toward the inner ear's sensory cells. The intercepted sound waves travel through the ear canal and cause the eardrum to vibrate. The eardrum vibrations are transmitted through an air-filled middle ear by the ossicles to the acoustic sensor, the cochlea, resulting in the motion of the stapes at the oval window of the cochlea (Figure 2.2). The stapes movement sets the cochlear fluid into motion, causing a traveling wave to form along the cochlear partition through the pressure difference between the two main fluid chambers. The pressure caused by the stapes motion gets released through complementary movement of the round window at the bottom chamber of the cochlear duct due to the incompressibility of the cochlear fluid.

The functional role of the middle ear is to match the acoustic impedance between the end point of the external ear, the eardrum, and the sensor port of the inner ear. Acoustic impedance, Z_{A}, is defined as the ratio of acoustic pressure, P, to volume velocity (velocity V times cross-sectional area, A) [21]:

$$Z_{\mathrm{A}} = \frac{P}{VA} \tag{2.1}$$

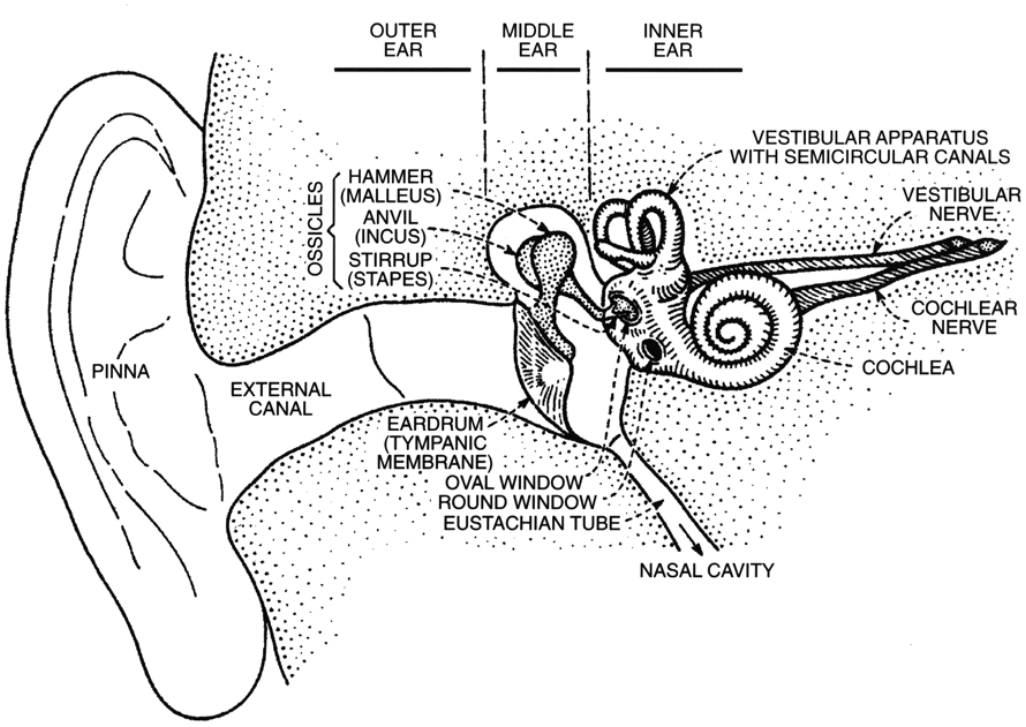

Figure 2.1: Human Ear

The human ear comprises the outer, middle, and inner regions. The outer ear includes the pinna and the external canal. The middle ear consists of three tiny bones, or ossicles, namely hammer (malleus), anvil (incus), and stirrup (stapes). The inner ear, or the cochlea, is snail like and filled with fluid. Cochlear nerve (i.e., the auditory nerve or the VIII th nerve), stems from the central axis of the cochlea and extends to the central auditory system. From [19].

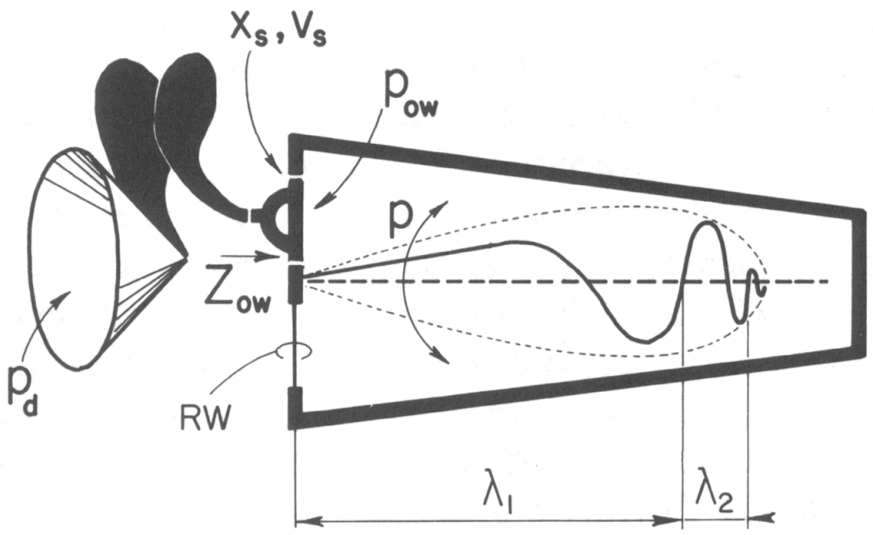

Figure 2.2: Mechanism of the Human Ear

Air pressure at the eardrum (P_{d}) is transformed into stapes displacement (X_{s}) and velocity (V_{s}) by the ossicular chain of the middle ear. Stapes motion creates a pressure in the vicinity of the footplate, P_{ow}, which is related to the cochlea's input impedance, Z_{ow}, and the stapes velocity, V_{s}. In the cochlea, P denotes the pressure gradient across the cochlear partition, which produces a traveling wave in the cochlear fluid and along the cochlear partition. Two full cycles of this wave are indicated by the wavelengths, λ_1 and λ_2. The traveling wave reaches its peak with short wavelength. RW: Round window. From [20].

Impedance matching is of significance because only when the acoustic impedance of two conducting media are identical can a sound wave be passed from one to the other without reflection [18, 22]. Since there is a ratio of 3880:1 between the measured acoustic impedances of water and air, different sizes of the eardrum and the footplate of the stapes come into play. Due to the fact that the velocities of the eardrum and the stapes are the same, and the force acting on the eardrum and the stapes are equal, a ratio of about 62:1 would yield an equal impedance at the eardrum and the stapes [18]. More sophisticated impedance calculations show that this ratio is a function of tonal frequency; it is actually equal to 62 at about 2 kHz [23].

The cochlea is a much more complex and delicate organ than the external and middle ear. Its basic structure is revealed in the cross-sectional sketch of a radial slice taken from the second turn of guinea pig (Figure 2.3). The cochlear partition that separates the cochlear fluid duct into three chambers, comprises the $basilar\ membrane$ (BM), and the $organ\ of\ Corti$ (OC). The BM consists of a number of fibers oriented in radial directions. These transverse BM filers are inserted into the bony $spiral\ lamina$ on the modiolus end and the spiral ligament on the opposite side. The BM is narrower and thicker in the base than it is in the apex, which imparts the stiffness gradient of the BM—This physical property is commonly believed to result in decreasing resonant frequency from the base to the apex along the cochlea.

The OC is a complicated superstructure, containing both sensory cells and supporting cells (Figure 2.4). Supporting cells mainly comprise pillar cells with two kinds, the inner pillar (IP) and the outer pillar (OP) cells, which are the chief structural cells in the OC. The trunks of pillar cells are composed of dense matrices of interlaced microfibrils and microtubules [25]. One IP cell and one OP cell, together with a small portion of the BM, form a relatively rigid structure.

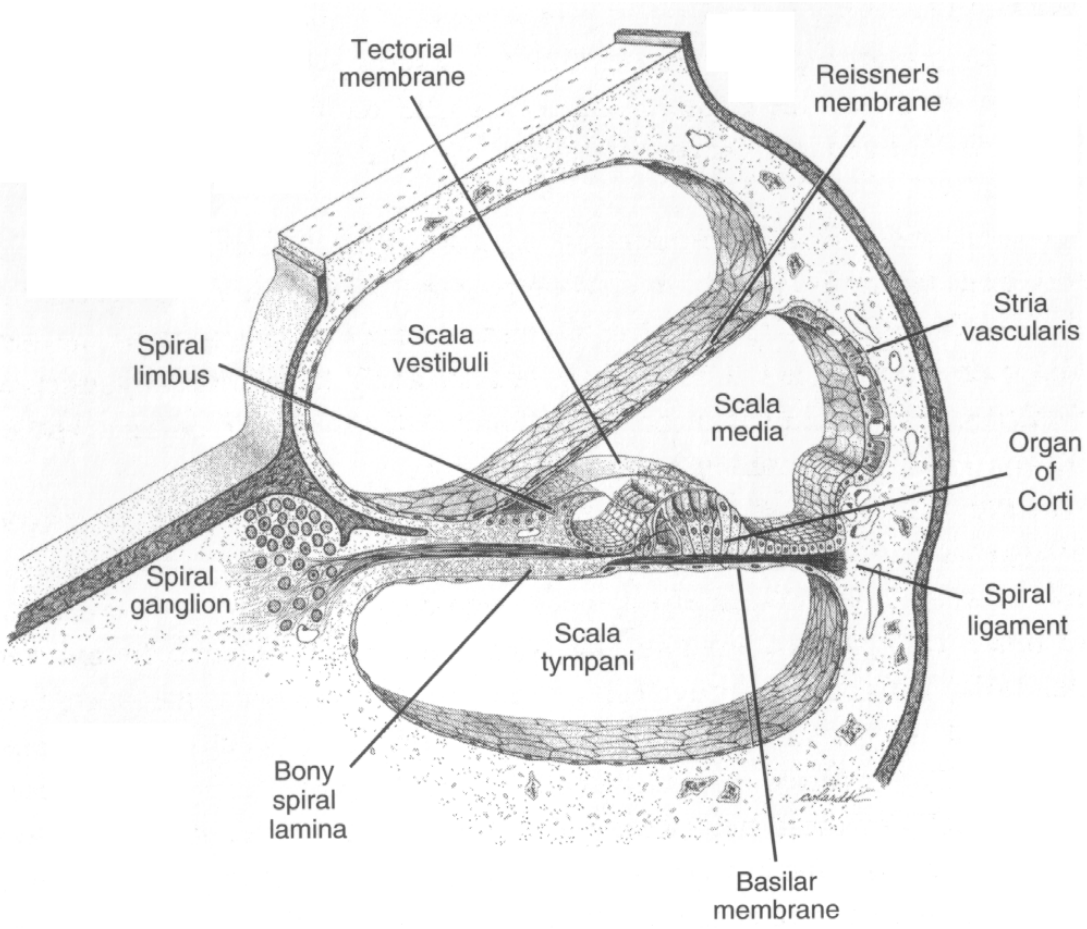

Figure 2.3: Radial Segment of the Cochlear Duct

Filled with fluid, the cochlear duct is divided into three scalae—scala vestibuli, scala media, and scala tympani—by the Reissner's membrane and the cochlear partition. The cochlear partition comprises the basilar membrane and the organ of Corti. The modiolus is to the left. From [24].

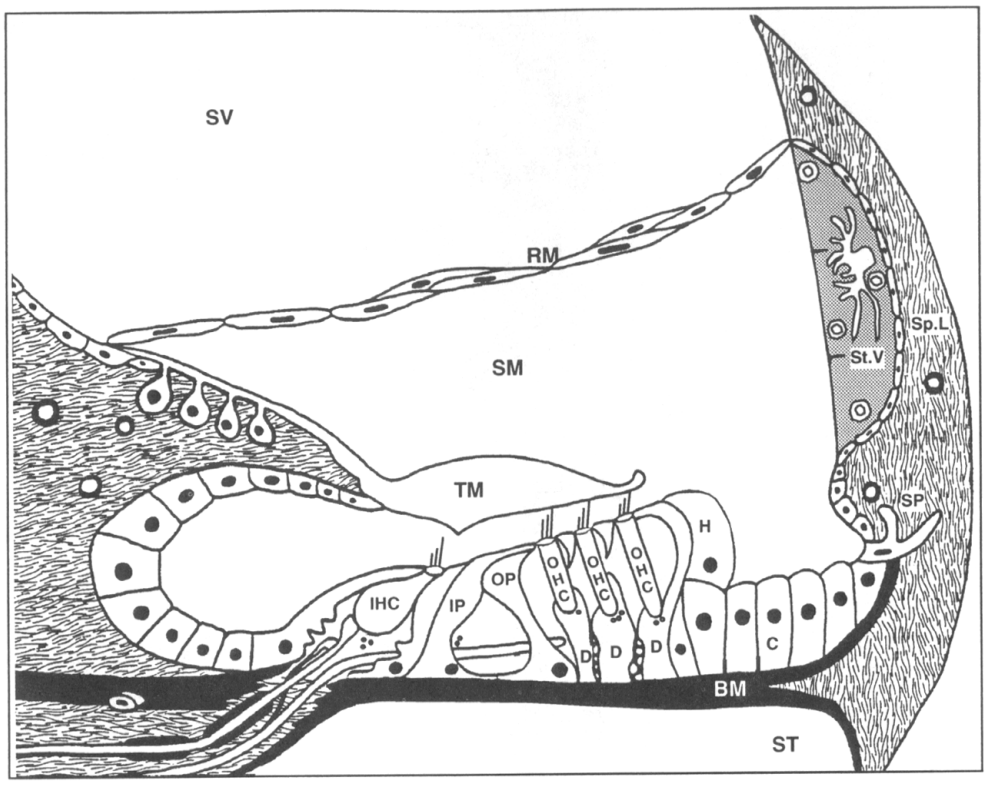

Figure 2.4: Cochlear Partition

Resting on the basilar membrane (BM), the organ of Corti (OC) contains both sensory and supporting cells. In mammal, there are three rows of outer hair cells (OHCs) and one row of inner hair cells (IHCs). The tunnel of Corti is formed by the inner pillar (IP) cell, outer pillar (OP) cell, and a small portion of the BM fiber. Deiters' (D), Hensen (H), and Claudius (C) cells are also constitutional components of the OC. From [26].

The sensory cells are mainly the hair cells, namely outer hair cells (OHCs) and inner hair cells (IHCs). IHCs encode sound information, for example, its frequency components, intensity, timing, and other physical properties, into neuronal electrical discharge patterns, carried to the central nervous system via afferent axons of $spiral\ ganglion$ cells. Meanwhile, efferent axons originate from the brain stem and innervate the hair cells, mainly OHCs.

Hair cells have hairs called stereocilia (Figure 2.4). IHCs, surrounded by supporting pillar cells, have stereocilia that are free to deflect angularly. The deflection of IHCs' cilia is the final mechanical step in the ear's transduction of acoustic signals into neural pulses [18]. In contrast, OHCs have stereocilia that are embedded in the tectorial membrane, particularly their tallest hair called kinocilium [18]. OHCs, supported only at their bases by $Deiters'\ cells$ (DCs) and at their apexes by $reticular\ lamina$ are free of cellular contact on their sides; this is believed to be pertinent to OHC function.

2.1.2 Cochlear Mechanics

Sound stimuli elicit both mechanical and electrical responses in the cochlea. Driven by the pressure difference across it, the BM vibrates at different cochlear locations depending on the input frequency, forming an amplitude peak of its motion at certain cochlear location called the best place, or the characteristic place; the corresponding input frequency is called as the best frequency, or the characteristic frequency for that location [27–29]. The BM responds maximally to high frequencies near the base as it is relatively stiff while it vibrates most near the apex in response to low frequencies [30] as it is floppy there. Acoustic energy is carried by the cochlear fluid, most of which is absorbed by the cochlear partition in the vicinity of the characteristic place (Figure 2.5).

A mechanical traveling wave is formed both along the basilar membrane and in the cochlear fluid, a fundamental discovery in auditory physiology by von Békésy [31]. The traveling wave is a displacement wave on the BM or a pressure wave in the cochlear fluid (near the BM), a wave much slower than the acoustic wave, which transverses the entire cochlea (at a speed of 1,550 m/s) in a few microseconds [32]. The traveling wave propagates at a relatively large speed near the base, with a long wavelength, and slows down near the characteristic place, where the wavelength becomes short [33]. Right after it peaks, where almost all its energy is acquired by the BM, the traveling wave decays rapidly, forming a sharp cutoff.

BM's up-and-down motion is transformed into the stereociliary deflections of OHCs through the structural organization of the OC (Figure 2.6), as summarized in [18]. As the BM is driven downward by acoustic pressure, the relatively rigid triangular pillar-cell-complex keeps its shape and pivots clockwise about the foot of the IP cell, which is situated near the edge of the relatively immobile bony spiral lamina. The OHC, cradled by the Deiters' cell, is carried along with the BM, moving away from the spiral limbus. The tectorial membrane—attached to both the stationary limbus and the stereocilia of the receding OHC—is stretched, resulting in shear force between the tectorial membrane and the reticular membrane. Thus, the downward BM motion deflects the OHC stereocilia in the counterclockwise direction, leading to forward transduction (i.e., a mechanoelectrical process, in which mechanical force results in electrical transduction current in OHCs [34]). Influx of transduction current depolarizes the OHC, causing changes in transmembrane receptor potential, which in turn provide input to OHCs' motor activity.

A further transduction stage in the cochlea occurs at the IHC, from fluid motion to deflection of IHC stereocilia (Figure 2.7). The counterclockwise deflection of the OHC stereocilia displaces the fluid (endolymph) underneath the tectorial membrane and above

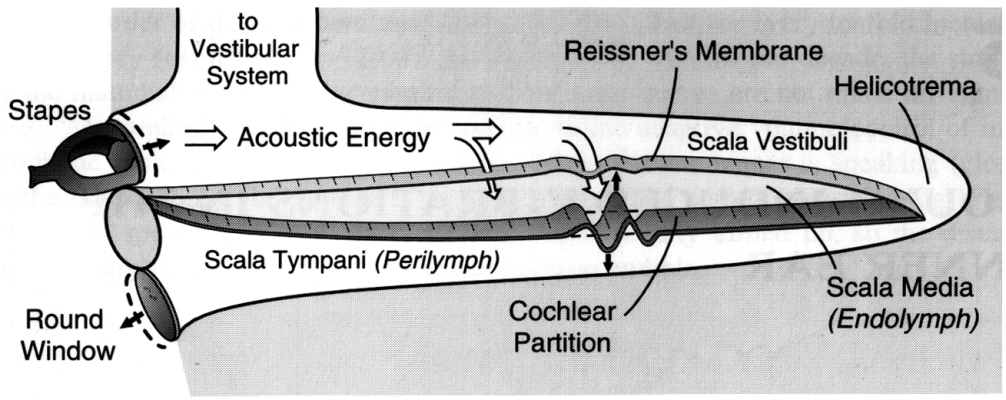

Figure 2.5: Basilar Membrane Vibration

In this sketch of uncoiled cochlea, due to the fluid incompressibility, volume displacement of the round window equals that of the oval window (stapes). Acoustic energy is carried by an acoustic wave that travels from base (stapes) to apex (helicotrema), absorbed by the basilar membrane (BM) where the resistance to the pressure is minimum. Thus, the BM vibrates up and down, driven by the pressure difference across it. From [18].

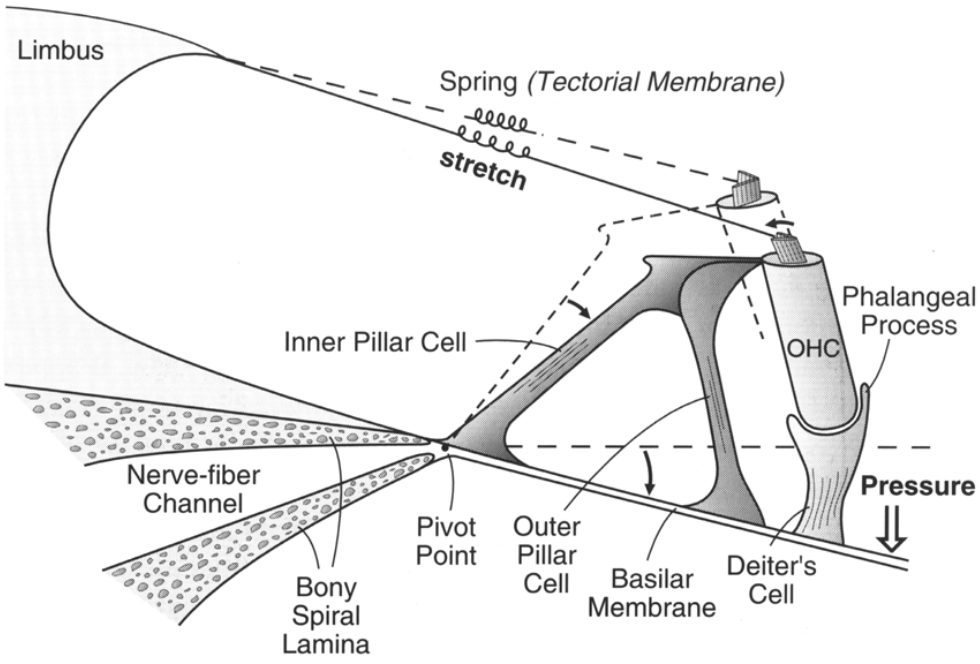

Figure 2.6: Deflection of Outer Hair Cell Stereocilia

Basilar membrane (BM) motion causes deflection of outer hair cells' (OHC) stereocilia through the microanatomy of the organ of Corti (OC). In the diagram, the downward BM motion is transmitted, through the supporting pillar cells in the OC, to deflect the stereocilia to the counterclockwise direction, resulting in hyperpolarization of the OHCs. Similarly, upward BM motion will cause depolarization of OHCs. From [18].

the reticular lamina [35]. Unlike in OHCs, the stereocilia of IHC are not attached to the tectorial membrane, thus they are free to move. Lined up in one row perpendicular to the flow of fluid, the cilia present to it an almost uninterrupted barrier to be efficiently deflected by the fluid motion [18]. The ciliary deflection of IHC leads to transduction currents, which in turn give rise to neurotransmitter release at the IHC-spiral ganglion cell synaptic interface.

Cochlear Amplifier

The cochlea exhibits remarkable acoustic sensitivity, high frequency selectivity and (nonlinear) high-level compression in processing sound signals. The marked differences in vibration amplitude/velocity and frequency tuning, in the measurements between dead and living cochlea strongly suggested that a feedback amplification mechanism, namely the cochlear amplifier, exists within the OC and injects mechanical energy into the BM locally [36], thus enhancing the sensitivity and frequency tuning of the cochlea. In other words, the cochlear amplifier, together with the passive frequency tuning of the BM, accounts for the characteristic behavior of a living cochlea (i.e., large amplitude of motion, sharp tuning at low sound levels).

OHCs have been widely believed to be the amplifying agent, thus the origin of the cochlear amplifier, given their ability to change their cell body lengths under acoustic stimulation [13, 14, 37]. Although the upper limit has not yet been established [18], the speed of electromotility, or at which OHCs alter their length, is as high as 24 kHz [38]. Cell body length change of OHCs are relatively small, which are only a few percent of the cell's length at most, but in the same amplitude range as sound-evoked BM vibrations [18].

Upon their contraction or elongation, OHCs generate fast motile forces [39, 40], and

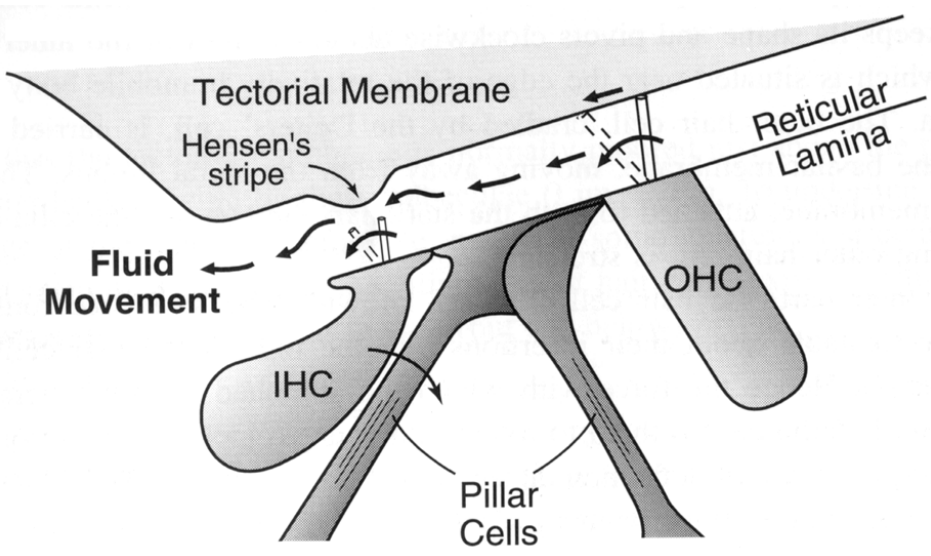

Figure 2.7: Deflection of Inner Hair Cell Stereocilia

Stereocilia deflection of outer hair cells (OHCs) cause the fluid in the gap between stereocilia and the tectorial membrane to flow, which in turn deflects the nearby inner hair cells' stereocilia in the same direction as that of the OHCs' stereocilia. From [18].

these forces are transmitted onto the BM to alter its motion. Deiters cells, which cradle OHCs, most likely deliver these forces as they are formed by closely packed microtubular arrays, thereby exhibiting columnar rigidity [18].

The prevailing view is that there exists a feedback system involving OHC electromotility that enhances the BM motion (Figure 2.8). The process consists of both forward transduction and reverse transduction [41]. Contrary to forward transduction, reverse transduction corresponds to the process from electrical cell membrane voltage to mechanical force, an electromechanical process. However, details of the cochlear amplifier still remains largely unknown as it is not clear in what precise manner the OHC motile forces feedback on the BM so that the BM motion is amplified in a frequency-selective fashion.

Cochlear Nonlinearity

It has been discovered that OHCs have a saturation property, thus yielding nonlinear cochlear responses. The relation measured between sound pressure and receptor voltage for outer hair cells shows the typical $\mathcal{S}$-shape (Figure 2.9A) [42, 43]. Further, the cell body length change of an OHC saturates with its transmembrane potential (Figure 2.9B). Assuming that acoustic pressure causes proportional BM displacement and the OHC length change is proportional to the cells' receptor potential change, a saturation relation can be derived in which OHCs' motile forces saturate with respect to BM displacement produced by acoustic pressure [17].

Cochlear nonlinear behavior includes high-sound-level compression [18], two-tone suppressions [32], distortion-product otoacoustic emissions [46], and more. One of the most prominent nonlinear phenomena in the cochlea is high sound-level compression. Sound signals at low intensities are amplified in frequency-selective fashion at certain cochlear

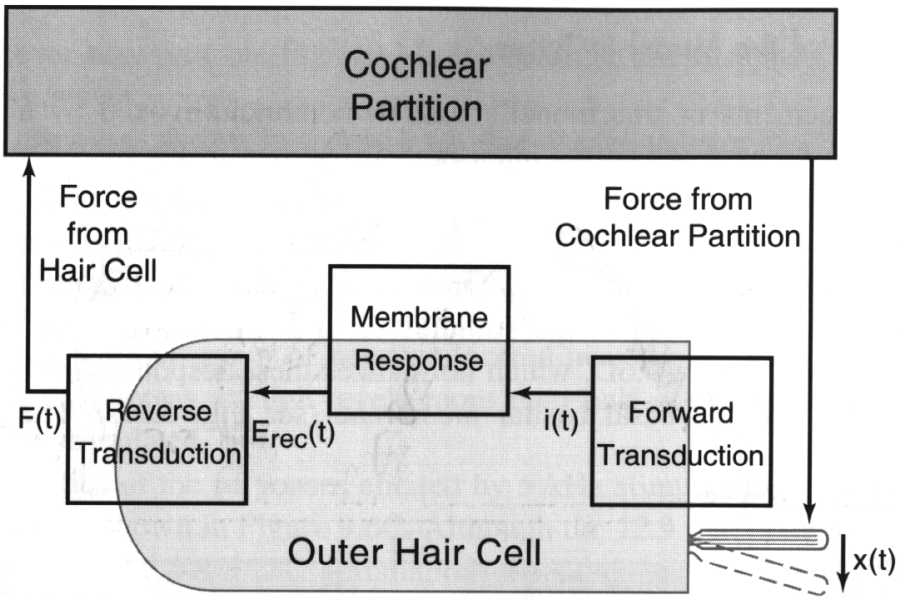

Figure 2.8: Feedback System with Outer Hair Cell Electromotility

This diagram presents a prevailing view of how outer hair cell (OHC) motility affects basilar membrane (BM) motion in general. BM motion causes deflection of OHCs' stereocilia, resulting in a transduction current, $i(t)$, which in turn produces the receptor potential, $E_{\mathrm{rec}}(t)$. The generated receptor potential changes the OHCs' length. Completing the loop, the length change of OHCs exerts a force $F(t)$ on the BM. This feedback system has been postulated as the cochlear amplifier. From [18].

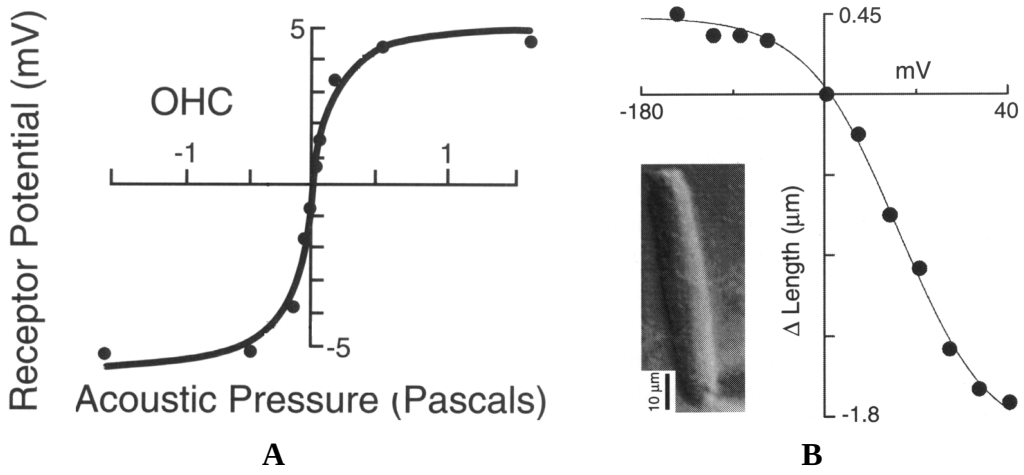

Figure 2.9: Saturating Profile of Outer Hair Cells

A The relation between acoustic pressure and outer hair cells' receptor potential is $\mathcal{S}$-shape, saturating at high pressure levels [44]. **B** Changes in the cell body length of an isolated outer hair cell in response to various transmembrane voltage steps are also $\mathcal{S}$-shape [45]. As can be seen, hyperpolarization elicited elongation while depolarization caused contraction. Dots: Raw data. Solid line: Boltzmann function. Insert: Outer hair cell.

position—the cochlea exhibits large gain, while high-level sound signals are nearly not amplified—the cochlea exhibits small gain (Figure 2.10). Thus, the cochlear responses at the peak show compressive growth with input intensity. From an engineering perspective, the cochlea realizes automatic gain control, in which the gain of the cochlear amplifier becomes attenuated with the increase of input intensity (Figure 2.10).

Two-tone suppression (2TS) is the phenomenon in which the cochlea's response to one tone (i.e., the probe) is suppressed by the presence of a loud tone (i.e., the suppressor). 2TS occurs in the BM's mechanical motion, in the receptor potential of IHCs, and in the electrical discharges on the auditory nerve (AN) [48]. Although there is debate as to whether 2TS at the IHC and AN levels is the direct result of the suppression occuring at the BM level, it is believed that two-tone suppression with the BM's mechanical responses is attributed to saturation of OHC forces [32].

One of the major characteristics of 2TS is its intensity dependence (Figure 2.11). In the absence of a suppressor (or for low suppressor levels) the responses to the CF tone grow at compressive rates. At higher suppressor levels, the responses to low-level CF tones are reduced strongly, but only weakly at high levels. As a result, the BM input-output curve for the CF tones is substantially linearized in the presence of moderately intense suppressor tones. Another feature of 2TS is that it is characteristic frequency specific with regard to both the probe tone and the suppressor tone.

2.2 Mathematical Cochlear Modeling

In the past few decades, enormous efforts in mathematical modeling have been made to help uncover the nature of cochlear mechanics. Since the discovery of OHC electromotil-

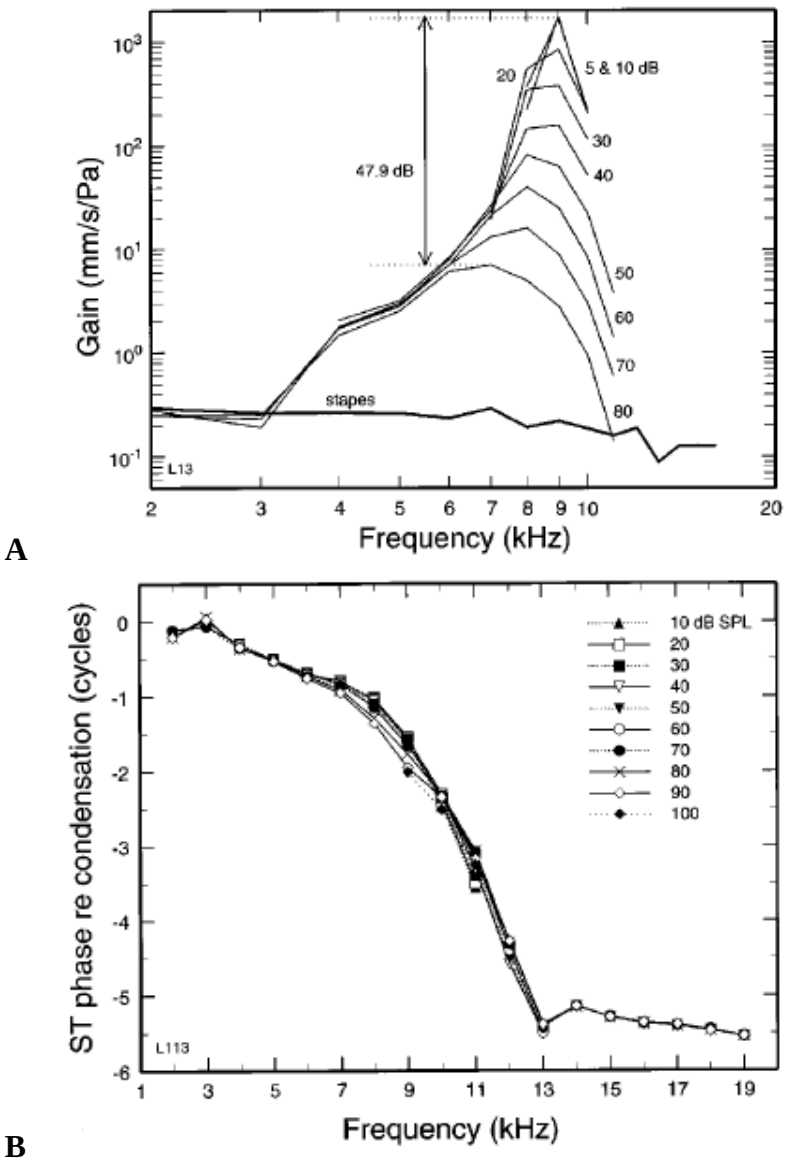

Figure 2.10: Nonlinear Compressions in the Cochlea

Compression, or compressive growth in responses, with input intensity is one of the nonlinear phenomena in the cochlea. **A** Families of isointensity curves representing the gain (velocity divided by stimulus pressure) of basilar membrane responses to tone pips as a function of frequency (abscissa) and intensity (parameter, in dB SPL). The thick line at the bottom indicates the average motion of the stapes. **B** The variations of basilar membrane response phases as a function of frequency. Phases—BM displacement toward scala tympani relative to condensation at the eardrum thus inward ossicular displacement—were computed. Each curve represents data for a single stimulus intensity. From [47].

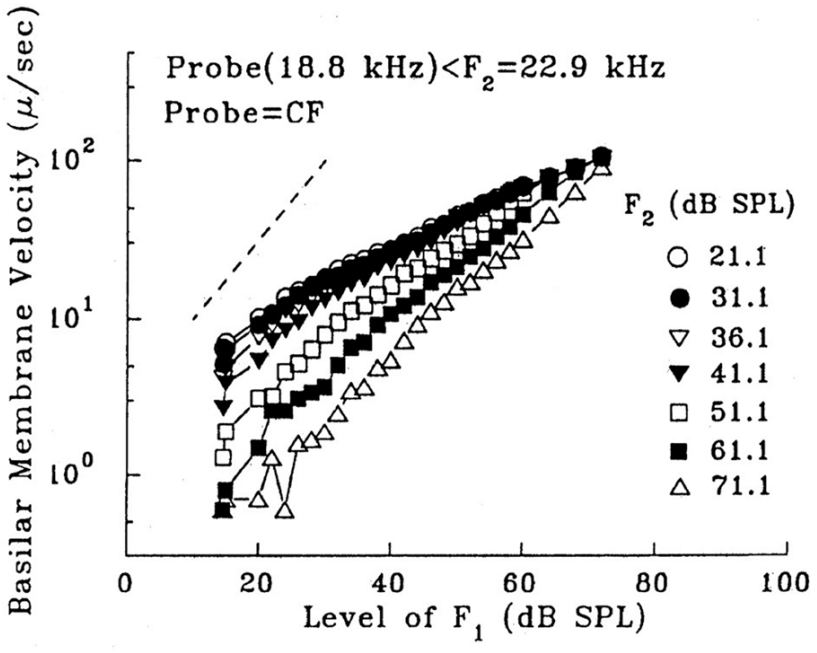

Figure 2.11: Two-tone Suppression in the Cochlea

Two-tone suppression at the basilar membrane's velocity-intensity functions responding to a near-CF tone ($F_1 = 18.8$ kHz) presented simultaneously with a suppressor tone ($F_2 = 22.9$ kHz). The parameter is the intensity of the suppressor tone. These are data measured from Guinea pig cochlea in [49].

ity, cochlear modeling has become focused on incorporating the OHC motile forces in order to reproduce characteristic cochlear behavior. Although the assumptions and mechanisms proposed differ somewhat in explaining how the cochlear amplifier works, all existing models shared a common goal, that is, to obtain BM responses to sound comparable to measured physiological data.

Models have been modified and improved as more physiological findings and measurements have accumulated, especially by including micro-mechanical details within the organ of Corti of the cochlea. Since the discovery of outer hair cell electromotility in the mammalian cochlea [13], cochlear modeling has been focusing on exploring the detailed manner in which OHC forces enhance basilar membrane vibration. It is commonly believed that the OHC motile forces are transmitted, somehow through the complex organizations of the OC, onto the BM to affect its motion.

Cochlear models that include OHC motility are referred to as active cochlear models; those without OHC motility as passive cochlear models [50]. Building active cochlear models have helped understand better how OHC motility contributes to amplification and sharpening of traveling waves along the cochlear partition (CP) at low sound levels [51–53] and nonlinear behavior at high sound levels. A number of active cochlear models have introduced OHC motility into cochlear macromechanics (i.e., interaction between fluid hydrodynamics and BM second-order sections) to account for the active amplification [15–17, 54–59].

It is commonly assumed that OHCs are the origin of the active mechanism in active cochlear models. With the same goal to account for the active amplification, they differ in how the OHCs exert forces on the BM, and in the role of other structures and components (e.g., sensory and support cells) within the CP. A common approach to most of the models

was adding a feedback loop to simulate the OHC motility [18].

The BM fibers are thought to be only weakly coupled to their adjacent neighbors through the cochlear fluid [60] due to transverse (i.e., radial) orientation of these fibers. Most cochlear models ignore the longitudinal elasticity (stiffness) because it is negligible compared to the transverse stiffness. This assumption was mainly justified by the experiments performed by Voldrich [61], in which they probed the BM to study its stiffness. However, the latest experiment carried out by Naidu and Mountain [62] provided consistent results with the earlier experiments done by von Békésy in 1960 [31], in conflict with Voldrich results. These findings support the notion that there exists longitudinal coupling, weak though, between BM transverse fibers and the coupling increases in strength from base to apex.

Several cochlear modelers have implemented this longitudinal coupling, as a novel hypothesis of active mechanism, in order to produce more realistic cochlear responses. However, perspectives on how to include the coupling differ. Hubbard [55] included a second traveling wave mode that is coupled to the traveling wave formed along the BM, thus coupling BM segments in the longitudinal direction. Wong [63] took a straightforward approach by including weak stiffness between BM transverse fibers to generate distortion product otoacoustic emission.

A few recently developed active cochlear models took into account the OHCs basal tilt [15–17, 58, 59]; this arrangement was first pointed out by Voldrich [64]. These models considered longitudinal coupling based on the observed anatomical structure of OC, in a way that is compatible with the prevalent opinion on the contribution of OHC motility. This perspective is that the motile OHC forces are delivered to neighboring cochlear locations, thus coupling the adjacent BM fibers longitudinally. Along this line of modeling activity,

Sang and Geisler [15] proposed a feed-forward mechanism that considers the basal tilt of OHCs, in which OHC forces affect the motion of the downstream neighboring BM; there were also other models based in this idea [16, 65].

These models hypothesized, counter-intuitively, that this tilt sharpens tuning and amplifies BM motion through feedforward OHC forces that act on the downstream BM segment. These models with feedforward OHC forces produce larger amplification than that in a passive model, but the overall responses are not realistic compared to physiological data (e.g., too much phase accumulation). As one of the remedies for the problem, the tectorial membrane was modeled as an additional resonant system in the feedforward model proposed in [15].

Although Karavitaki and Mountain argued that this feedforward mechanism is not supported by the experimental results that the longitudinal component of OHC motion in the apex is about ten times smaller than the radial component [66], we believe that OHC does not really need to move in the longitudinal direction to a large extent, to give rise to the feedforward OHC forces given the unique tilt arrangement.

Another striking anatomical feature within the organ of Corti, which has not been explicitly taken into account in a cochlear model, is the oblique orientation of the phalangeal processes (PhPs) (Figure 2.12). PhPs are extended from Deiters' cells, tilted toward the apex along the longitudinal axis [26]. This PhP's tilt has been only considered for its constitutional role in the complex; its possible role in transmitting OHC forces onto the BM in the process of cochlear amplification was left unexplored. Brownell and his coworkers [13] observed that an OHC, the PhP of the DC on which it sits, and the portion of the RL between the apical end of the PhP and the stereocilia end of the OHC constitute a mechanical unit within the CP, and pointed out that increases in OHC length would

make this unit more rigid whereas decreases would make it more compliant. Our proposed cochlear amplifier mechanism takes into account both tilts in the OC, which we shall present in detail in Chapter 3.

Cochlear nonlinearity is believed to originate from the nonlinear behavior of the OHC [68], which was described in Section 2.1. Some nonlinear cochlea models focused on finding an efficient numerical method for solving nonlinear equations [16, 69–75]. Modeling efforts have been made to model the nonlinearity of the cochlear behavior, including compressive growth at high sound levels, two-tone suppression, and distortion product otoacoustic emissions [18, 76–79]. In most nonlinear models, the nonlinearity was obtained by introducing a nonlinear element, through certain nonlinear functions (e.g., the hyperbolic tangent $\tanh$).

2.3 Cochlear Modeling in VLSI

Engineers have long attempted to build physical cochlear models that behave similar to the biological cochlea. The major motivation of this approach stems from its great potential for a myriad of sound-processing related applications, for example, acoustic front-end of automatic speech recognition systems and signal processing component of auditory prosthetic devices. Meanwhile, these physical models also function as real-time computational tools due to their neuromorphic nature, complementary to physiological measurements and mathematical modeling, to help uncover the cochlear mechanics. When built for such purpose, they share common goals with mathematical simulations, which is to emulate the nonlinear active cochlear behavior in order to shed light on how the cochlea works. Among physical cochlear models, silicon cochleas, particularly analog VLSI (very large scale in-

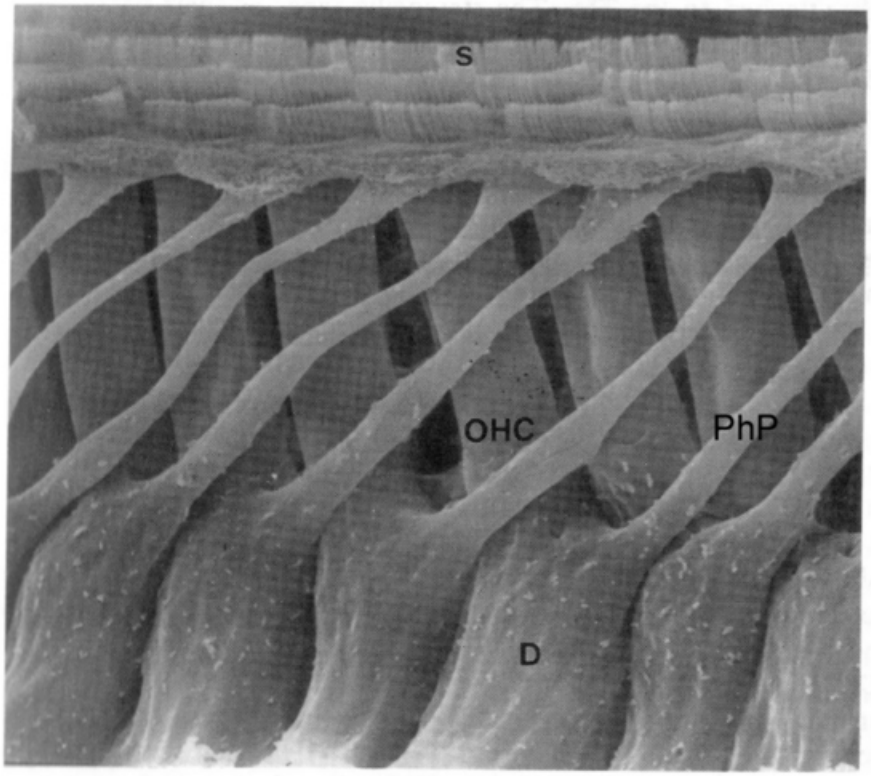

Figure 2.12: Cochlear Microanatomy

Scanning electron micrograph of the organ of Corti of the mole rat cochlea. Each outer hair cell (OHC) is cupped at its base by a Deiters' (D) cell. Each Deiters' cell extends a stalk up and expands into a phalangeal process (PhP), inserted into the reticular laminar (not labeled) at some distance from the base of the Deiters cell. The outer hair cells are tilted toward the base (on the left) while the phalangeal process is titled toward the apex (on the right). From [67].

tegration) implementations, have exhibited advantages over computer software simulations in computation efficiency and over digital cochlear chips based on analog to digital converter and digital signal processor in power consumption [6, 80].

We shall only review analog VLSI cochlear models in this thesis due to the nature of our present work. Several generations of silicon cochleas have been built since Lyon and Mead developed the first analog electronic cochlea [5]. The first silicon cochlea modeled the biological cochlea as a one-dimensional bank of second-order low-pass filters (LPFs) whose resonant frequencies decreased exponentially. The design employed transconductance amplifiers [81] and capacitors to implement the second-order sections and these second-order sections were cascaded; the output of one section was fed as input to the following section. With exponentially increasing time constants along the cascade, the silicon cochlea was able to generate the characteristic frequency-position map in the biological cochlea.

Despite improvements by other researchers [82, 83], the silicon cochlea based on a cascade structure continues to suffer from several shortcomings, which have been found to be mainly associated with the cascaded structure [6, 84]. In this design, the peak gain (at a certain position in the cascade) is obtained through accumulation along the cascade, which imposes a constraint on the number of filters that can be included in a cascade because too much accumulated peak gain would drive filters out of their linear operating range. In addition, phase accumulates along the cascade, resulting in too much phase delay at the resonant peak, which is unrealistic compared to biology. Meanwhile, noise and distortion with the output of preceding filters undesirably propagate along the cascade. It is also obvious that the cascade structure has poor fault tolerance because dysfunction of one second-order section caused all of its following sections to fail.

Adopting a more biology-inspired approach, Watts built a silicon cochlea with parallel

structure to address these shortcomings of the cascade structure [6]. This parallel structure was based on the biological cochlea's mechanics in which the basilar membrane interacts with the cochlear fluid. Recent designs have improved Watts original design through circuit innovation [84–86]. The cochlear chip with a parallel structure integrated the cochlear fluid model using a resistive network, resulting in a two-dimensional passive cochlea design. The basilar membrane sections are coupled through the fluid resistive network, thereby eliminating the problems of phase delay and poor fault-tolerance. The inclusion of cochlear hydrodynamics reproduced the transition from long-wave to short-wave propagation in the cochlear duct.

Nevertheless, the parallel structure of silicon cochleae elicited a new problem. In a second-order system, a high (desirable) quality factor (Q) corresponds to phase frequency responses that have a steeper slope, resulting in phase differences close to π among neighboring basilar membrane sections (due to the inherent frequency-position map). Coupling among basilar membrane sections through the fluid network, therefore, counteracted one another eliminating the response gain due to their out-of-phase motion [7]. In other words, this interference has destructive nature, leading to little response gain.

Advances in analog VLSI circuit design technique has also been employed to design better silicon cochleas. These mainly include the transition from voltage mode [5, 6, 82] to current mode [80, 84, 85]. Using current to represent signals instead of voltage, current-mode circuits offer the advantages of larger dynamic range, lower power consumption, and smaller chip area, over their voltage-mode counterparts [87]. The recently proposed log-domain filter design approach has also been adopted to design a silicon cochlea [84], which uses the logarithmic characteristic of the weak-inversion MOSFET (metal-oxide semiconductor field effect transistor) to extend dynamic range.

Despite all the progress that has been made in developing silicon cochleas, responses of existing designs fall short in achieving responses comparable to their biological counterpart. None of existing silicon cochleas was able to reproduce all the characteristic cochlear behavior, including large dynamic range, large gain and sharp tuning at low sound levels, and low gain and broad tuning at intense sound levels. The major factor to account for poor model responses is that none of the designs include implementation of the cochlear amplifier mechanism—an indispensable component for generating characteristic cochlear behavior. In addition, the constraints imposed by the physical medium for a silicon cochlea, for example, device (transistor) mismatch, cause discrepancy between the model implementation and the biological cochlea properties. It is obvious that the biological cochlea also has mismatch (i.e., variations in its biophysical properties), however, it somehow preserves its extraordinary ability in sensing and processing sound signals. Discovering the biology's secret or trick for fighting mismatch and variation will no doubt lend itself to improving artificial cochlea-like sound processing system. Building a better silicon cochlea requires a physiologically plausible cochlear amplifier mechanism and desires advanced circuit technique. In order to match the brain's power efficiency, lowering the power consumption in a silicon cochlear design should also be taken into account as one of the design goals.

Chapter 3

The Active Cochlea: Mathematical Model

In Chapter 2, we have reviewed existing cochlear modeling effort in both mathematics and VLSI circuits. Complementary to physiological measurements, these cochlear models have made enormous contributions to help uncover the cochlear mechanics, providing explanation for physiological measurements. In this chapter, we present a nonlinear active cochlear model that implements a novel cochlear amplifier mechanism. The idea of our proposed mechanism stems from the assumption that the cochlea's micro-architecture serves its functioning effectively.

We shall focus our modeling effort on numerical simulation and mathematical analysis as follows. We first describe the cochlear microanatomy and the active mechanism, then we formulate a two-dimensional (2D) mathematical cochlear model, followed by model simulation carried out through both numerical and semi-analytical methods. To verify the proposed cochlear amplifier mechanism, we compare the simulation results obtained

through both solution methods with physiological data measured from mammalian cochlea. Through mathematical analysis, we further characterize the traveling wave formed along the basilar membrane (BM) and in the cochlear fluids. Last, we extend this linear active model to a nonlinear active one to simulate the nonlinearity of cochlear responses, including the compression at high sound levels and two-tone suppression. The mathematical model described in this chapter serves as a blueprint for the design of a physical model using analog VLSI techniques, which will be discussed in Chapter 4.

3.1 The Linear Model: Numerical Simulation

In this section, we first discuss the outer hair cell (OHC) forces, including their generation, property, and its possible role in cochlear mechanics. Then we describe our cochlear amplifier mechanism that is based on both cochlear microanatomy and outer hair cell motility.

3.1.1 Outer Hair Cell Motile Forces

OHCs have unique cortical structure in the lateral surface [36], which are believed to be somehow responsible for their ability of mechanical deformation—changing their cell body length—at acoustic frequencies when they are acoustically or electrically stimulated. Roughly speaking, the lateral surface of an OHC consists of three layers, the outmost plasma membrane, the innermost lateral cisternae, and the helical circumferential filaments in the middle [36]. The array of cytoskeletal filaments are crosslinked by thinner strands and attached by pillars to the outmost lateral cistern and to large particles in the inner leaf of the plasma membrane.

It is widely held that among various cortical elements of OHCs, the array of large particles bound in the plasma membrane plays an important role in OHC motility [88]. The idea is that the membrane-bound particles undergo conformational changes when the transmembrane voltage changes thereby causing the cell to hyperpolarization or depolarization. Upon depolarization, the effective diameters of the particles are reduced or their packing density becomes increased, resulting in shrink of the surface area of the OHC. Similarly, hyperpolarization causes expansion of OHCs. The change of surface area of OHCs are then translated into a change in its cell body length.

Deformation of OHCs can be deemed to be "rapid" although the upper limit to the speed of OHC electromotility has not yet been determined [18]. Therefore, it is reasonable to assume that OHC forces can be generated following acoustic frequency and on a cycle-by-cycle basis. In other words, we assumed that OHC force are exerted onto the BM instantaneously and not selective with input frequency.

3.1.2 Active Bidirectional Coupling

It has been widely accepted that OHCs are the origin of the cochlear amplifier and that they make essential contributions to characteristic cochlear behavior. However, the exact manner or details about how OHC motile forces lead to active amplification in the cochlea still remains a mystery due to the difficulties in accessing and exploring the functional roles of different components in the cochlear partition. In our effort pursuing the cochlear amplifier mechanism, we believe that the complexity and uniqueness of organization and architecture of the cochlear partition, especially of the organ of Corti (OC), play a direct role in transmitting OHC forces onto the BM, thus enhancing the BM's motion.

We hypothesized a novel cochlear amplifier mechanism in which we considered the exquisite microstructure of the OC. However, this mechanism did not intend to include every anatomical details of the OC. Instead, it postulated a possible mean of implementing the feedback of OHC forces to account for the active cochlear amplification.

The basic idea of the mechanism is that OHC forces, due to OHC mechanoelectro motility, can be delivered bidirectionally in the longitudinal direction through the cochlear micro-architecture; if this additional energy is applied at the appropriate cochlear location, it will enhance the vibration of the basilar membrane (BM), thus generating desired amplification. These forces are exerted by the OHC on the BM segment through the Deiters' cell (DC), realizing active bidirectional coupling (ABC), which results in high sensitivity, high frequency selectivity, and nonlinear compression.

We hypothesized that the mechanical unit, consisting of the OHC, the phalangeal process (PhP) and the reticular membrane (RL), plays a direct role in transmitting OHC forces onto the BM, thus actively amplifying BM responses. As the main vibrating organ within the cochlea, the BM is composed of transverse fibers that are weakly coupled longitudinally [18]. The weak coupling is From the base to the apex, BM fibers increase in width and decrease in thickness. The resulting exponential decrease in stiffness gives rise to the passive frequency tuning of the cochlea.

The cochlear partition is divided into a number of radial segments from the base to the apex with OHCs and PhPs arranged within the OC (Figure 3.1). For simplicity, we define each BM segment as consisting of one DC sitting on the BM, the apical end of one PhP, and the stereocilia end of one OHC—the latter two both attached to the RL. The stereocilia end of one OHC lies in one segment, say segment $i-1$, while its basolateral end lies in the immediately apical segment i. The DC in segment i sends a PhP that angles toward the

apex of the cochlea, with its apical end inserted just behind the stereocilia end of the OHC in segment $i+1$. The RL is made up of the stereocilia end of the OHCs and the apical end of PhPs of DCs.

Our hypothesized cochlear amplifier mechanism comprise effect of two distinct OHC forces due to the tilted structure, namely the feedforward and feedbackward mechanism. The general idea of the feedforward mechanism is that the motile OHC force due to OHCs' contraction or expansion is exerted onto an adjacent downstream BM segment due to the tilt of the OHC. And the novel insight of the feedbackward mechanism is that the OHC force is delivered onto an adjacent upstream BM segment due to the tilt of the PhP. Downstream and upstream represent the longitudinal direction with respect to the forward (i.e., from base to apex) traveling wave—downstream corresponds to apicalward while upstream corresponds to basalward.

In the case of rigid OHCs (without motility), each BM segment moves up and down as the cochlear fluids' pressure difference between the scala vestibuli (SV) and the scala tympani (ST) acts on the BM. Figure 3.1B depicts a transverse view of the cochlear partition, which reveals a critical structure called arches of Corti. The arches of Corti are formed by the inner pillar cell (IPC), the outer pillar cell (OPC), and part of the BM transverse fiber. The base of the IPC works as a rigid pivot point when the BM fiber vibrates up and down. Given the micro-architecture, the movement of the BM segment $i-1$ causes the stereocilia of the same segment to deflect due to the radial shear motion between the RL and the TM.

In the case of OHCs with electro-motility, the deflection of the stereocilia in turn results in the contraction or expansion of the OHC because ion flow across the membrane depolarizes or hyperpolarizes the OHC. Due to its longitudinal tilt, the OHC in segment $i-1$ exerts a force on the BM (through the DC) that sits in the downstream segment i, which is

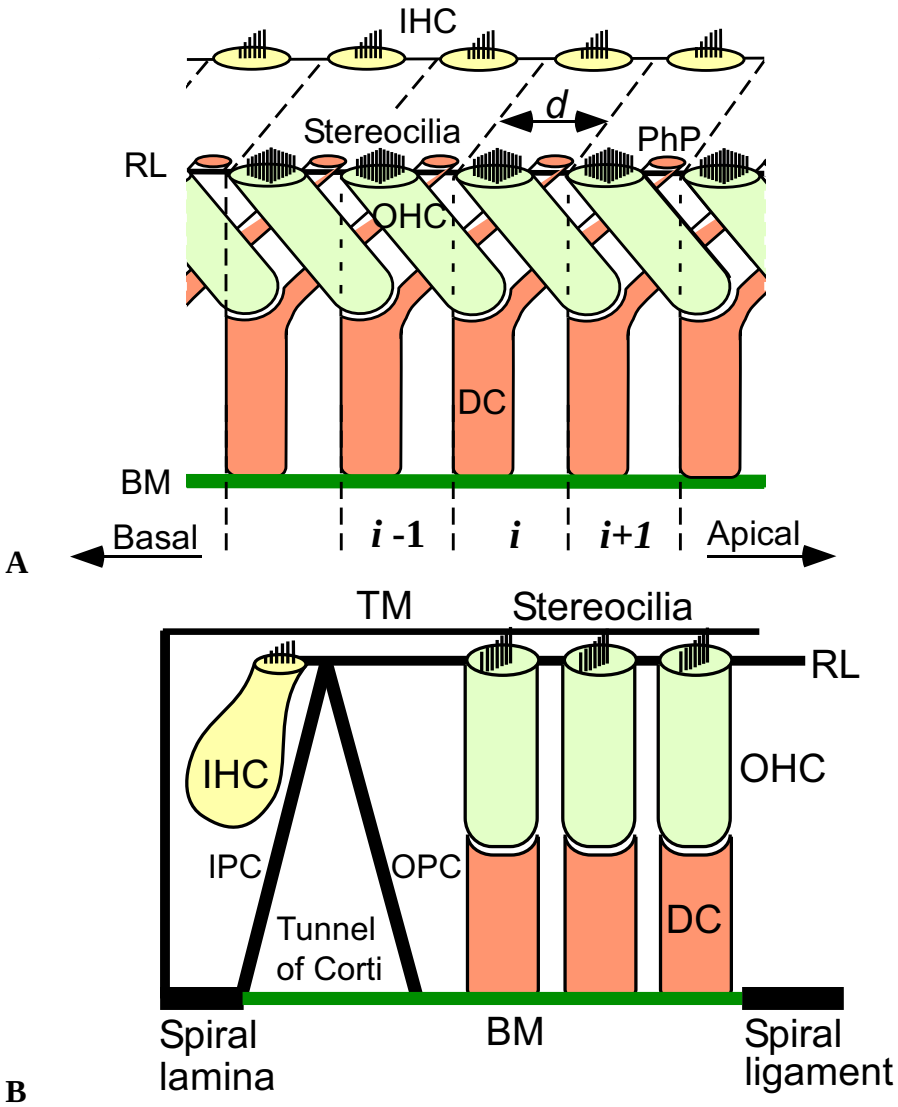

Figure 3.1: Active Bidirectional Coupling Mechanism

A Longitudinal view. **B** Transverse view of the Organ of Corti. In **A**, three segments are labeled (i.e., $i-1$, i, and $i+1$) for illustration. Only the outermost (from the modiolus) row of OHCs is shown; the tectorial membrane (TM) is not shown. In **B**, the TM is included. d denotes the longitudinal tilt distance.

pulled to or pushed away from the RL. Thus, the vibration of BM segment i amplifies the displacement of its upstream neighbor, segment $i-1$, due to the feedforward OHC force.

Besides this feedforward mechanism, our model features a novel feedbackward mechanism, which is implemented through the PhP extending from each DC's main trunk [89]. Similar in structure to pillar cells within the OC, the DCs and their PhPs are presumably rigid. As a result, with the apical end of each PhP immediately adjacent to that of an OHC, it is reasonable to propose that the PhP transmits mechanical forces effectively—both tensile as well as compressive.

An pertinent phenomenon about the RL is the premise for the feedbackward mechanism. At a step of current injection, both the BM and the RL moved toward each other, which is consistent with the relationship between the direction of BM's motion and the property of OHC forces (i.e., tensile or compressive). In other words, when the BM is driven upward, corresponding to depolarization of OHCs, thereby contraction of the OHCs, which in turn pull down the RL, resulting in opposite direction of motion of the BM and the RL. More importantly, it was reported that the RL moves 5 to 10 times farther than the BM [90]. This not only showed clearly that the OC is indeed deformable to a physiologically significant extent [18], but also provided us a rather useful hint on the relative magnitude of feedbackward OHC forces to that of feedforward OHC forces.

Process of feeding back OHC forces is described as follows. In segment $i+1$ of the cochlear partition, the deflection of stereocilia due to the upward or downward displacement of BM segment $i+1$ causes the OHC whose stereocilia end lies in the segment $i+1$ to contract or expand, thus pulling down or pushing up the RL to some extent (meanwhile, BM segment $i+2$ (not labeled in Figure 3.1) is pulled up or pushed down due to the feedforward OHC force). The driven RL segment $i+1$ then pushes down or pulls up the rigid

PhP and the whole DC, exerting a force on the BM segment i. Thus, BM segment i is additionally pushed or pulled by the upward or downward displacement of the downstream BM segment $i+1$, due to the feed-backward OHC force.

In summary, the micro-architecture of the cochlear partition gives rise to feedforward and feedbackward OHC forces that introduce active bidirectional longitudinal coupling between BM segments. The motion of BM segment $i-1$ reinforces that of segment i while the motion of segment $i+1$ opposes that of segment i.

3.1.3 Formulation of a Two-Dimensional Linear Model

We implemented a two-dimensional (2D) cochlear model in which the cochlear fluids are included. This physical model is illustrated in Figure 3.2A. In the 2D model, both the length of the uncoiled cochlea and the finite height of the cochlea duct (i.e., the scala vestibuli (SV) and the scala tympani (ST)) are discretized into a number of sections with the original aspect ratio of the cochlea maintained. The stapes movement sets the cochlear fluid into motion and causes a vibratory deformation of the cochlear partition.

In the 2D model (Figure 3.2B), both the length of the uncoiled cochlea and the height of the cochlea duct (i.e., the SV and the ST) are discretized into a number of sections with the original aspect ratio of the cochlea maintained. The variable x represents the distance from the stapes along the cochlear partition, with $x = 0$ at the stapes and the round window and $x = L$ (uncoiled cochlear duct length) at the apex and the helicotrema. And y represents the vertical distance from the wall, with $y = 0$ at the top/bottom wall of cochlear duct and $y = h$ (cochlear duct radius or height) at the BM.

We first describe the formulation of a linear 2D mathematical model based on our

cochlear amplifier mechanism—active bidirectional coupling (ABC), and present its numerical solution. Next, we shall extend the linear model to a nonlinear model that simulates cochlear nonlinear responses by incorporating OHCs' saturation property.

Assuming incompressibility of the cochlear fluids, we modeled only the bottom cochlear chamber (ST) in our 2D model, which is mathematically equivalent to modeling both chambers because the fluid movements in the SV and ST are complementary (Figure 3.2B). Now let $\phi(x, y, t)$ represent the difference between the velocity potentials in the SV and ST:

$$\phi(x, y, t) = \phi_{\mathrm{SV}}(x, y, t) - \phi_{\mathrm{ST}}(x, 2h - y, t), \tag{3.1}$$

where ϕ_{SV} is the velocity potential in the SV while ϕ_{ST} is the velocity potential in the ST.

From here on, we omit the time variable t in the expressions and equations for the linear version of the model so that we will deal with the model in the frequency domain.

Due to the assumed incompressibility of the cochlear fluid, the velocity potential difference ϕ of the fluids is required to satisfy

$$\bigtriangledown^2 \phi(x, y) = 0, \tag{3.2}$$

where $\bigtriangledown$ is the Laplacian operator. This potential is related to fluid velocities in the x and y directions:

$$V_{\mathrm{x}} = -\frac{\partial \phi(x, y)}{\partial x}, \quad \text{and} \quad V_{\mathrm{y}} = -\frac{\partial \phi(x, y)}{\partial y}. \tag{3.3}$$

Considering the pressure difference, $P_{\mathrm{d}}(x, y)$, thereby the force, imparted on a small element of fluid and its resultant velocity, V_{x} and V_{y}, we obtain the following relations

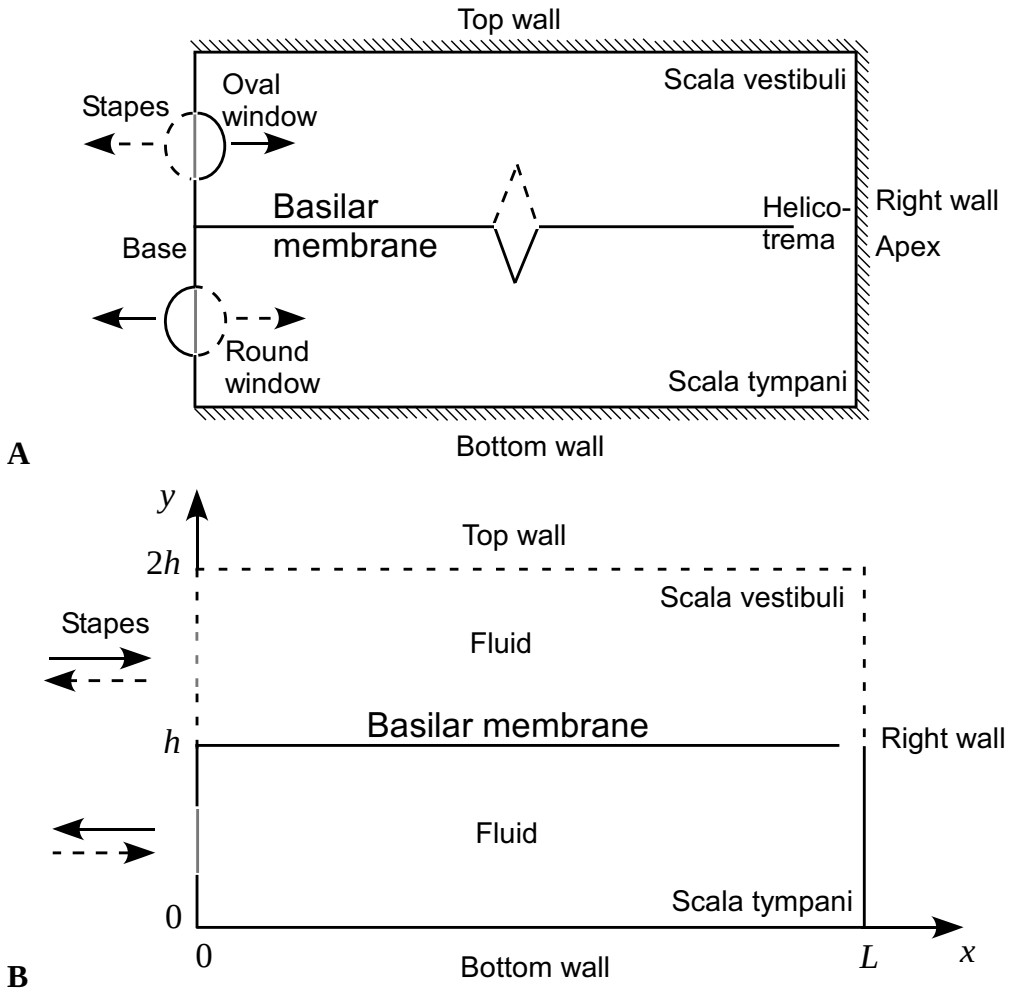

Figure 3.2: Two-dimensional Cochlear Model

The uncoiled cochlea is represented by a rectangle, which includes the two major fluid ducts, scala vestibuli (SV) and scala tympani (ST). As an approximation for the passive-cochlea case, the cochlear partition was reduced to only the basilar membrane. **A** The stapes motion causes the oval window moves inward (solid-line half circle) and outward (dashed-line half circle), which in turn pushes or pulls the round window due to the incompressibility of the fluid. **B** In the two-dimensional (2D) cochlea model, because the fluid movements in the SV and ST are complementary (i.e., equal in magnitude but with opposite directions), only the bottom compartment was considered in order to reduce simulation time and computation load as well as taking advantage of simpler coordinates. Thus, the basilar membrane forms one of the boundaries at $y = h$. The longitudinal length of the cochlea at the apex is denoted by L.

according to the Newton's second law:

$$-\frac{\partial P_{\mathrm{d}}(x,y)}{\partial x} = 2\rho\frac{\partial V_{\mathrm{x}}}{\partial t} \quad \text{and} \quad -\frac{\partial P_{\mathrm{d}}(x,y)}{\partial y} = 2\rho\frac{\partial V_{\mathrm{y}}}{\partial t}, \tag{3.4}$$

where ρ is the fluid density and the factor 2 accounts for the same amount of fluid mass in both SV and ST. Combining the relation with Equation 3.3 yields the relation between pressure difference P_{d} and velocity potential ϕ:

$$P_{\mathrm{d}}(x,y) = 2\rho\frac{\partial \phi}{\partial t} \tag{3.5}$$

The BM's vibration is in the vertical direction, with downward displacement (i.e., towards the ST) being positive. The BM has mass, damping, and stiffness. Its motion is directly driven by the pressure difference across it, which can be described as follows.

$$\begin{aligned} P_{\mathrm{d}}(x,y) + F_{\mathrm{OHC}}(x) &= S(x)\delta(x) + \beta(x)\dot{\delta}(x) + M(x)\ddot{\delta}(x), \quad \text{at } y = h, \\ F_{\mathrm{OHC}}(x) &= \alpha S(x)(\gamma\delta(x-d) - \delta(x+d)), \end{aligned} \tag{3.6}$$

where $M(x)$ is the mass, $S(x)$ is the stiffness, and $\beta(x) = \zeta\sqrt{S(x)M(x)}$ is the damping, per unit area, of the BM, and ζ is the damping ratio; δ is the downward displacement of the BM while the first time-derivative of δ is its velocity and the second is its acceleration. $P_{\mathrm{d}}(x,y)$ at $y = h$ is the pressure difference at the BM. $F_{\mathrm{OHC}}(x)$ combines feedforward and feedbackward OHC forces, expressed as a fraction α of the BM stiffness (i.e., OHC motility factor). γ is the ratio of the feed-forward to the feed-backward coupling, representing relative strengths of the OHC forces exerted on the BM segment through the DC, directly, and through the tilted PhP. d denotes the tilt distance, which is the horizontal displacement between the source and the recipient of the OHC force, assumed to be equal for feedforward

and feedbackward cases.

The stapes and the round window at the base are assumed to move identically except in opposite directions. The basal boundary condition is described as follows.

$$-\frac{\partial \phi}{\partial x} = f(t), \quad \text{at } \ x = 0, \tag{3.7}$$

where $f(t)$ is the velocity of the stapes (defined to be positive for inward velocity).

At the apex, the horizontal velocity is zero due to the existence of hard wall. Therefore, the apical boundary condition is described as follows.

$$\frac{\partial \phi}{\partial x} = 0, \quad \text{at } \ x = L. \tag{3.8}$$

At the bottom wall, the fluids do not have a vertical motion, thus the velocity in the y direction is zero, which is described as follows.

$$\frac{\partial \phi}{\partial y} = 0, \quad \text{at } \ y = 0. \tag{3.9}$$

3.1.4 Model Simulation Results Using Finite-Difference Method

Having obtained the mathematical formulation of an active cochlear model, we shall explore its responses or behavior in responding to any sound stimulus. We first employed a numerical approach to obtain model responses, or simulating the model on a digital computer. The major advantage of numerical simulation is that it provides a straightforward and stereotyped means for obtaining model behavior—discretization in space and/or time,

transformation/approximation of the original set of governing equations, and solving the equivalent equation set for responses.

The numerical method we used is Neely's finite difference (FD), which has been most widely employed in solving linear cochlear models [73, 91, 92]. Other numerical methods in the frequency domain included integral-equation method proposed by Allen [93] and Sondhi [94]. In the FD method, derivatives in the ordinary differential equations that describe the fluid hydrodynamics and all the cochlea's boundary conditions were approximated by their finite-difference counterparts. Thus, a set of differential equations becomes a set of linear algebra equations, which can be solved at moderate computational cost with digital computers.

Specifically, we simulated the linear active model numerically in the frequency domain and a nonlinear active model in the time domain. In order to investigate the effect of OHC motility on the BM motion, we simulated the model using different OHC motility factors α. The model parameter used in our simulations are listed in Table 3.1.4. Part of the parameters are chosen to match the empirical data of frequency-position map of cat [95]. In this simulation, the cochlea is discretized into 350 segments longitudinally, amounting to radial segments approximately 71 μm long (for a cochlear duct length of 25 mm). In the vertical direction, 13 segments were used to represent the fluids at each cochlear position.

We obtained the BM displacement responses—amplitude (normalized by the stapes displacement) and phase (with respect to the stapes motion)(Figure 3.3). The input excitation was a 2 kHz pure tone. The OHC motility factor α varied from 0.0 (passive case) to 0.20 (active case), resulting in different values of amplitude gain in the BM displacement.

Response characteristics were summarized in Table 3.1.4 in terms of peak gain (BM

Parameters and denotation	Values	Unit
Cochlear duct height h	1.0	mm
Cochlear duct length L	25.0	mm
Fluid density ρ	1.0×10^{-3}	$\mathrm{g/mm^3}$
BM mass per unit area $M(x)$	3.0×10^{-5}	$\mathrm{g/mm^2}$
BM stiffness per unit area $S(x)$	$5.0 \times 10^{6} e^{-0.4x}$	$\mathrm{g/(mm^2 s^2)}$
BM damping ratio ζ	0.2	
Tilt distance d	71.0×10^{-3}	mm
Segment length $\triangle$	1.0×10^{-2}	mm
OHC motility factor α	$0.0 - 0.2$	
Forward-to-backward ratio γ	0.3	

Table 3.1: Mathematical Model Parameters

This set of parameters were chosen for simulating the cat cochlea.

response peak amplitude normalized by the stapes motion amplitude), peak phase (phase lag relative to the stapes motion), Q_{10} (Q_{10} is used to quantify the sharpness of tuning, calculated as the ratio between the CF and the frequency span of the curve 10 dB below the peak. In other words, the larger the Q_{10}, the sharper the tuning.), and peak location, or characteristic place (CP).

With the varying α from 0.0 to 0.20, the response peak became larger and tuning gets sharper. When $\alpha = 0.15$, the amplitude of the BM displacement was realistic while the phase accumulation at the peak was larger compared to the physiological data (around -1 to -6π radians [32]).

As was evident in the simulation, inclusion of OHC motility in the passive cochlear model elicited active behavior of the cochlea. As can be seen from Figure 3.3A and Table 3.1.4, amplitude amplification of BM motion only occured in the vincinity of peak, giving rise to frequency-selective amplification of BM vibration. Phase response curves almost overlap with one another (see Figure 3.3B): phase accumulation did not change much near the base while phase lag at the peak varied a little simply due to the shift of peak loca-

α	Peak gain (dB)	Peak phase (π radians)	Q_{10}	Peak location (mm)
0	17.6	-5.1	0.6	11.4
0.1	46.2	-18.7	3.5	14.6
0.15	79.5	-19.2	6.1	14.6
0.2	114.6	-22.0	6.1	14.6

Table 3.2: Mathematical Model Responses with Varying Outer Hair Cell Motility

This table summarizes the characteristics of the basilar membrane responses in the cochlear model with different values of outer hair cell motility factor.

tion with the varying OHC motility factor α. This further suggested the restricted property of the location of the ABC-based cochlear amplifier.

3.1.5 Bidirectional versus Uni-Directional Coupling

In our model, a forward-to-backward ratio, γ, is used to describe the contribution of feedforward and feedbackward OHC forces to the BM's motion. Researchers have previously shown how an active cochlear model behaves with feedforward forces [15,17]. It is then instructive to investigate what roles of forward and backward OHC forces play in enhancing the BM's motion.

In order to demonstrate the effects of adding feedforward and/or feedbackward OHC forces into a passive model (without OHC motility), we simulated three variations of a linear active model (i.e., with only feedforward, with only feedbackward, and with both forces). The same parameter values were used for these simulations; the OHC motility factor α was 0.15 and the ratio between feedforward coupling and feed-backward coupling γ was 0.3 (in the case that feedforward OHC forces were present).

Peak amplitude, phase accumulation, and Q_{10} are used to evaluate the model response quantitatively. Figure 3.4 shows the amplitude and phase of the BM displacement, nor-

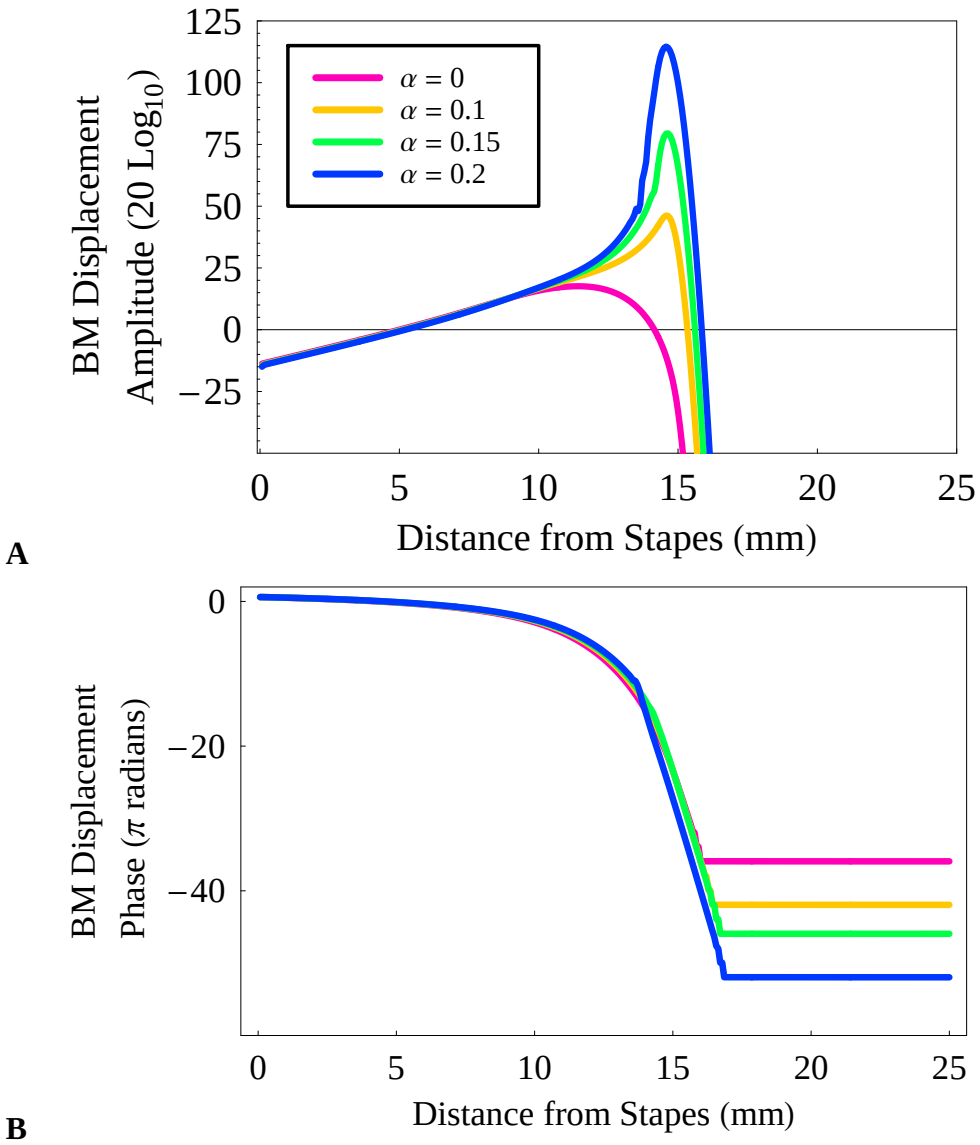

Figure 3.3: Effect of Outer Hair Cell Motility

BM displacement, normalized by the stapes displacement, for different outer hair cell motility factor (α) values, to a 2 kHz pure tone. **A** Amplitude. **B** Phase. When $\alpha = 0.0$, the model shows responses of a passive cochlea; as α increases, the model generally shows larger amplification, sharper tuning and more phase lag at peak. The parameter values used for the model simulation are listed in Table 3.1.4

malized by the stapes displacement, when driven by a 2 kHz tone for the three different configurations as well as the passive case. The BM response is least amplified (peak $<$ 20 dB) and broadest (Q_{10} is as small as 0.6) in the passive case, where the cochlear amplifier mechanism—ABC—is absent; feedforward forces alone increase the amplification (peak reaches around 54 dB) and sharpen the tuning (Q_{10} is about 2.6) to a limited extent; feedbackward forces alone increase the amplification a little more (peak reaches about 57 dB) and sharpen the tuning to a much larger extent (Q_{10} is 7.0); the BM displacement is largest (peak above 80 dB) and more realistically tuned (Q_{10} is 6.1) when both feedforward and feedbackward forces are included.

Regarding the phase, the four cases show different phase accumulation at the peak. The passive case and the feed-backward forces result in the smallest phase lag, and the case with both forces has moderate phase lag at the peak, while the feedforward forces causes the largest phase accumulation at -25.6 π radians. Thus, feedforward OHC forces alone result in too much phase shift, feedbackward OHC forces alone give rise to too sharp tuning with a not-large-enough peak, and when both of them, feedforward and feedbackward OHC forces are present with different strengths (i.e., when the cochlear amplifier mechanism—ABC—is included), the model produces the most realistic response in terms of peak amplitude, phase, and frequency tuning of the BM responses compared to physiological measurements [32].

3.1.6 Comparison with Physiological Data

The responses of the 2D linear active model at different input frequencies separated by octave intervals are shown in Figure 3.5. Due to the logarithmic frequency-position relation, the peak locations corresponding to each input frequency are spaced evenly at 3.5

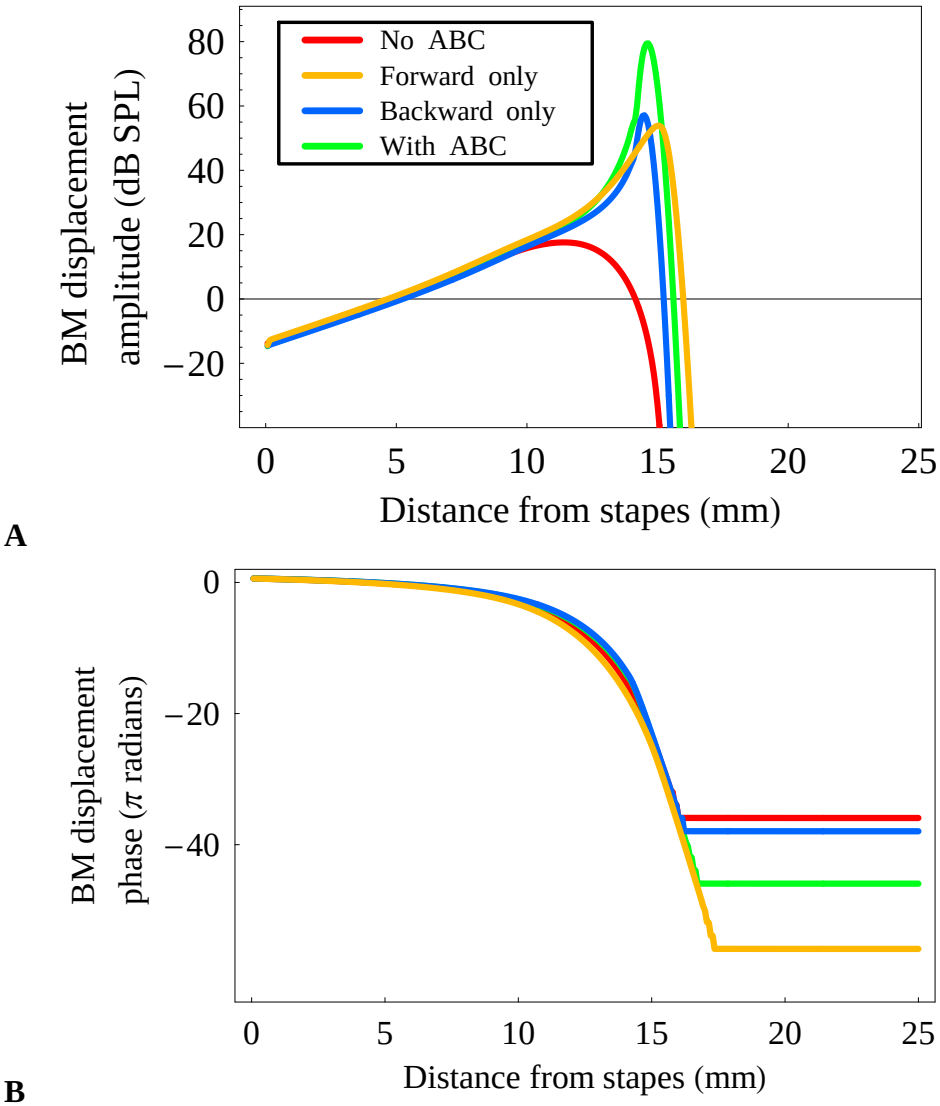

Figure 3.4: Comparison between Uni- and Bidirectional Coupling

Basilar membrane displacement responses, normalized by the stapes displacement, at 2 kHz pure tone. **A** Amplitude. **B** Phase. Four cases are simulated for comparison: No ABC, Feedforward only, Feedbackward only, and with ABC. ABC: Active bidirectional coupling.

Model	Peak gain (dB)	Peak phase (π radians)	Q_{10}	Peak position (mm)
No ABC	17.6	-5.1	0.6	11.4
Forward only	53.9	-25.6	2.6	15.1
Backward only	57.1	-17.4	7.0	14.5
With ABC	79.5	-19.2	6.1	14.6

Table 3.3: Bidirectional versus Uni-Directional Coupling: Simulation Results

This table compares the simulation results in the passive cochlea model (No ABC), the active cochlea model that includes unidirectional outer hair cell (OHC) forces (Forward only and Backward only), and the active cochlea model that include bidirectional OHC forces (With ABC). ABC: Active bidirectional coupling.

mm, which is just the octave span of cats (14% of cochlear length [95]). As the damping ratio ζ remains the same, the tuning for different input frequencies are the same across the cochlea.

A frequency-position map can be obtained from the peak locations for different input frequencies. The frequency-position map extracted from the model responses was plotted in Figure 3.6 and compared with the empirical function regressed from cat physiological data [96]. The model data are in reasonable agreement with the regressed function (their slopes are fairly similar), especially in the medium and high frequency region near the base. The model data demonstrated a near-linear relationship between cochlear positions and their corresponding CF in the base and middle of the cochlea. Discrepancy in slope between the model responses and the physiological data mainly lied in the apical low-frequency region, which may be attributed to the fact that differences between the apical and other regions of the cochlea was not included in the present model. It has been observed that the tuning curves of low-frequency and high-frequency fibers have different shapes [97, 98]. The factors to account for the basal-apical differences is yet to be discovered.

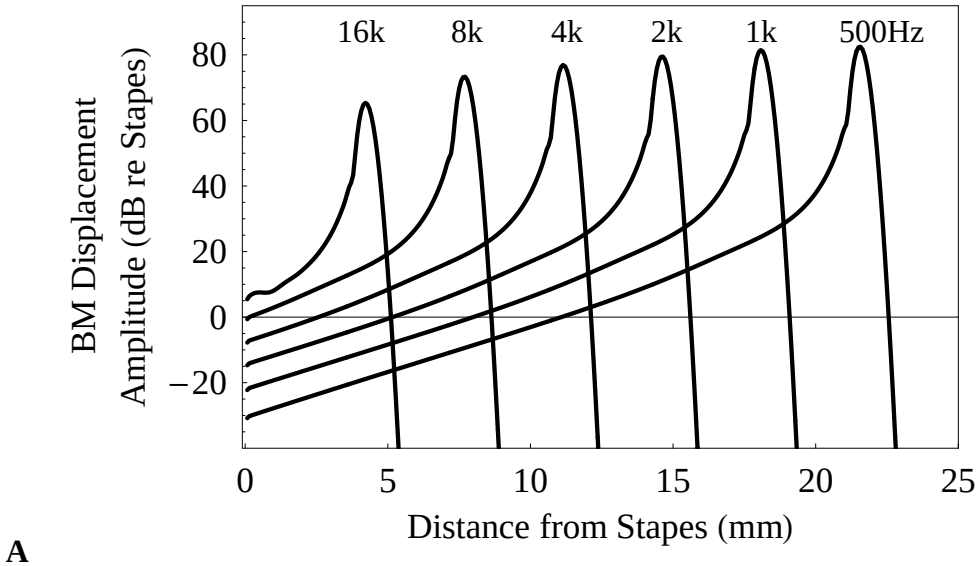

A

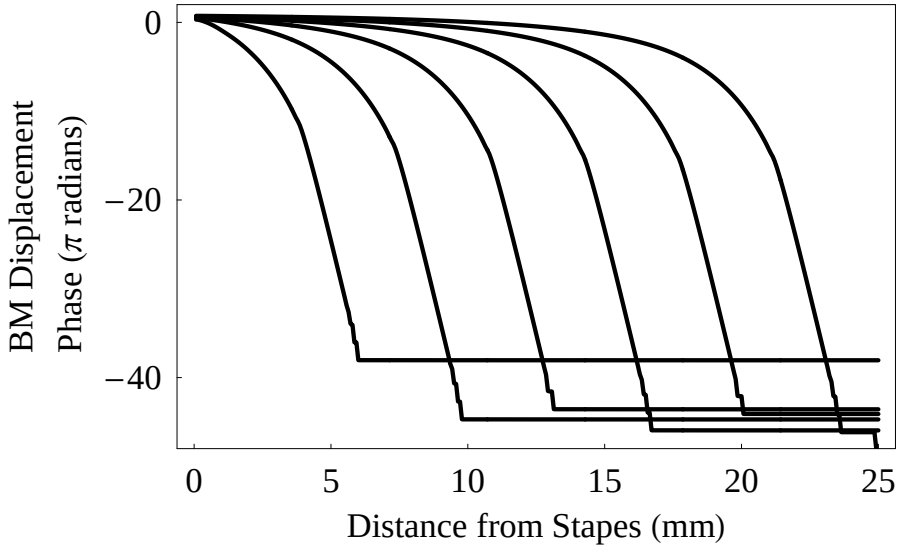

B

Figure 3.5: Basilar Membrane Displacement Responses

Longitudinal patterns of basilar membrane displacement to six octave-intervaled frequencies. **A** Amplitude. **B** Phase. The outer hair cell motility factor α was set to 0.15 for all the simulations in the plot.

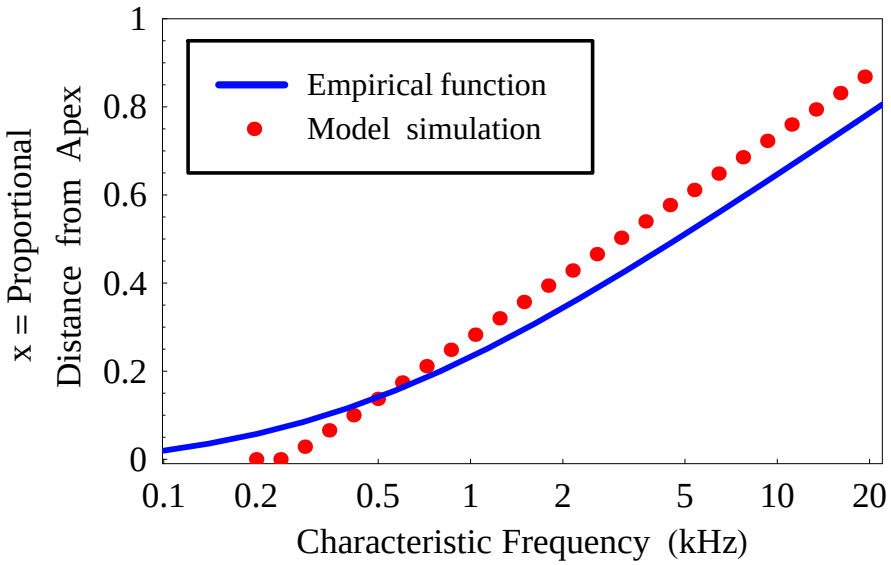

Figure 3.6: Frequency-Position Map

The red dots denote generated from simulation results the two-dimensional (2D) linear active model. The blue curve is the regressed function based on physiological data of cat; the empirical function is $f(\mathrm{Hz}) = 456(10^{2.1x} - 0.8)$ (x is the proportional distance from apex) [95].

3.1.7 Frequency Responses

We obtained the frequency responses of the BM velocity gain and phase at a cochlear position around 6.9mm from the stapes; its CF was around 9.3 kHz. The OHC motility factor was set to 0.17. The amplitude response compares favorably to the biological data, while the phase accumulation at the peak (-6.7 cycles) is larger than biological data (-0.5 to -3 cycle) [32].

3.2 The Linear Model: Semi-Analytical Solution

While numerical methods can solve for model responses, they do not provide much insight into the cochlear mechanics and the role of OHC motility in the active amplification; they also require prohibitive computation time and resource, especially in time-domain simulations of nonlinear cochlear models and for computation with fine discretization which is always desirable in the short-wave region to reduce the discretization error.

An alternative to numerical simulations is to solve the model analytically—that is, to obtain explicit mathematical form or expression to describe the fluid and/or BM's motion. However, since transcendental equations were involved in the problem, our analytical approach had to incorporate numerical calculation at certain point in the solution process, resulting in a semi-analytical solution (SAS). In addition, due to the difficulty in obtaining approximation in solving the nonlinear version of the model, our analytical approach only dealt with the linear version of the active cochlear model.

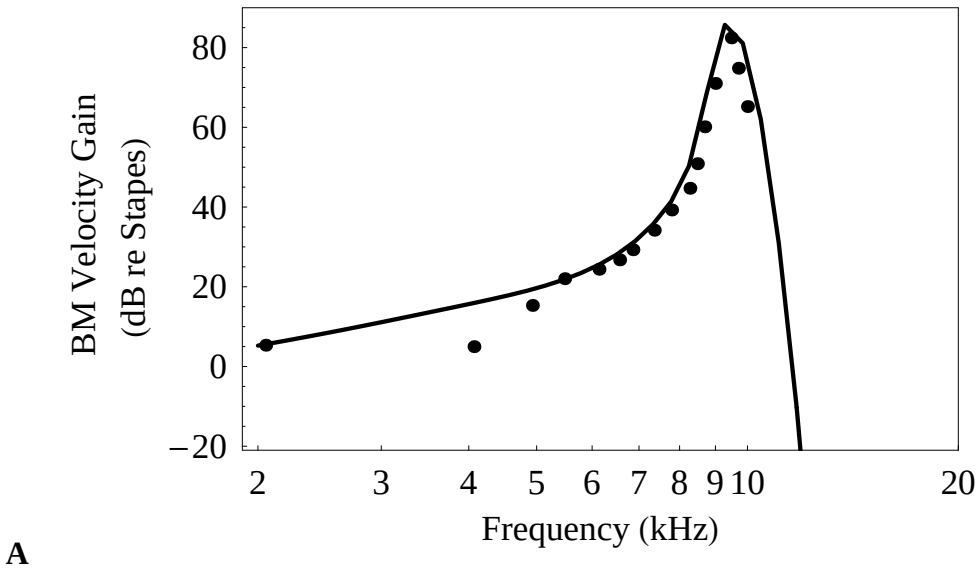

A

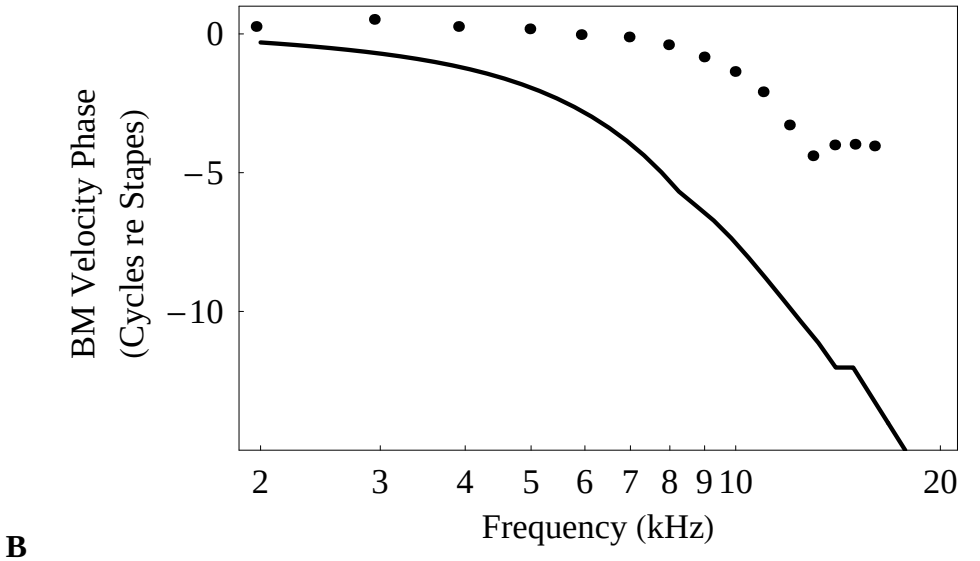

B

Figure 3.7: Frequency Responses of Basilar Membrane Velocity

A Response gain. **B** Phase. Both were relative to the stapes motion. The outer hair cell motility factor α was set to 0.17 to match the peak amplitude in the physiological data. Solid line: model simulation results. Dots: Physiological data [47].

3.2.1 Solution Procedures

Our analytical approach employed the LG (Liouville-Green), or WKB(Wentzel-Kramers-Brillouin) or WKBJ (Wentzel-Kramers-Brillouin-Jeffereys) method, a well-known approximation for describing wave behavior on shallow canals. Steele and Taber [99] and de Boer and Viergever [100] first applied this approach for solutions to cochlea models.

The WKB method is based on the idea that the wavelength can be estimated based on the properties of the medium in which the wave travels; it deals with the nonuniformity along the cochlear duct due to the varying BM boundary properties. WKB assumes that when the wavelength is short enough, the properties of the medium can be treated as uniform within the span of a wavelength [101]. As Steele and Taber pointed out [99], this short-wave approximation can still be applied to the long-wave region of the cochlea because the long wavelength region is defined relative to the height of the cochlear duct, and for the cochlea, the wavelength must be very long before the WKB solution becomes invalid. Further, the comparison that Zweig [102] made between the WKB and direct numerical integration solutions for a one-dimensional (1D) model confirmed that it is reasonable to use only exponentials in the analytical approximations.

Following the approach in [6], we assumed a solution form of the velocity potential ϕ that represented a wave traveling in the $+x$ direction with y dependence:

$$\phi(x, y, t) = Y(y)e^{i(\omega t - kx)}, \tag{3.10}$$

where k is the complex wavenumber and ω is the real angular frequency of the wave. This solution form must satisfy Laplace's equation (Equation 3.2) and the bottom wall boundary

condition (Equation 3.9). Thus, the solution form can be further determined as:

$$\phi(x, y, t) = B(x)\cosh(ky)e^{i(\omega t - kx)}, \tag{3.11}$$

where $B(x)$ varies with cochlear position x. The form of ϕ applies to any cochlear position (x, y) and time t while B and k take on different values due to the varying stiffness and damping of the BM along the cochlea, which forms one boundary of the fluid body. In other words, the wavenumber and wave amplitude are mainly determined by the physical properties of the BM.

As $V_{\mathrm{y}} = \partial\delta/\partial t = -\partial\phi/\partial y$ at $y = h$, the BM displacement δ can be computed as

$$\begin{aligned} & \delta(x, y, t)|_{y=h} = -\int \partial_y \phi(x, y, t)dt|_{y=h} \\ \implies \quad & \delta(x, t) = iB(x)e^{i(\omega t - kx)}k\sinh(kh)/\omega. \end{aligned} \tag{3.12}$$

By substituting these forms in Equation 3.12 and their corresponding derivatives, together with Equation 3.5, into the BM boundary condition (Equation 3.6), we derived a dispersion relation, which describes the relation between the wave's energy (i.e., input frequency ω) and its momentum (i.e., wavenumber k).

$$\frac{k\tanh(kh)}{1 + \alpha S(x)k\tanh(kh)(\gamma e^{ikd} - e^{-ikd})/(2\rho\omega^2)} = \frac{2\rho\omega^2}{S(x) + i\omega\beta(x) + (i\omega)^2 M(x)}. \tag{3.13}$$

Given any input frequency, we can solve this dispersion relation for k, which leads to the solution of fluid velocity potential ϕ as well as the BM displacement δ.

Furthermore, we had $V_{\mathrm{stapes}} = -\partial\phi/\partial x$ at $x = 0$ and we can derive the stapes displace-

ment as follows.

$$\delta_{\text{stapes}}(y,t) = \int V_{\text{stapes}} dt, \tag{3.14}$$

And the average stapes displacement is the integration over the height of the oval window (i.e., from $y = 0$ to $y = h$ as an approximation and simplification). That led to

$$\delta_{\text{stapes}}(t) = \frac{1}{h}\int_0^h \delta_{\text{stapes}}(y,t) dy \tag{3.15}$$

This gives a stapes displacement expression, which is a function of the input frequency ω and the wavenumber at $x = 0$ (denoted by k_0):

$$\delta_{\text{stapes}}(\omega, k_0) = |\frac{B_0 \sinh(k_0)}{\omega}|, \tag{3.16}$$

where B_0 is $B(x)$ at $x = 0$. And for simplicity, we assume the phase of the stapes displacement is zero. This stapes displacement will be needed for calculating the gain of BM responses (i.e., BM amplitude normalized by stapes motion).

3.2.2 Wavenumber Loci of the Traveling Wave

Now we can solve the dispersion relation for the wavenumber k at different cochlear position x. The parameters used for the semi-analytical solution is exactly the same as the numerical method (Table 3.1.4). Since the dispersion relation is transcendental, we have to solve it numerically. The solution is the loci of k along the cochlea, starting from $x = 0$ to $x = L$. During this process, we trace the locus of k by using the value of k at the previous position as the initial value.

For wave propagation in the $+x$ direction, the real part of the wavenumber, k_{r}, is in-

versely related to the wavelength, whereas the imaginary part, k_{i}, is related to the wave-amplitude. These relations are evident if we rewrite the Equation 3.12 by replacing k with $k_{\mathrm{r}} + ik_{\mathrm{i}}$ as

$$\delta(x,t) = iB(x)e^{k_{\mathrm{i}}x}e^{i(\omega t - k_{\mathrm{r}}x)}(k_{\mathrm{r}} + ik_{\mathrm{i}})\sinh((k_{\mathrm{r}} + ik_{\mathrm{i}})h)/\omega. \tag{3.17}$$

Thus, wave propagation in the passive and active models may be compared by plotting the real and imaginary parts of the wavenumber. As the wave propagates, it transitions from long wave to short wave, where its wavelength becomes much smaller than the cochlear duct's height.

Different OHC motility factor α in the simulation corresponded to strikingly different loci of k, especially in the short-wave region where k_{r} is large (Figure 3.8). The input was a 2 kHz pure tone. The wavenumber locus stayed in the fourth quadrant in the passive case where the OHC motility factor $\alpha = 0$ (Figure 3.8A; only the fourth quadrant was shown), while in the active cases where the OHC motility factor $\alpha > 0$, the wavenumber loci entered the first quadrant, right before the peak position at different extent with different OHC motility factors, and then returned to the foruth quadrant (Figure 3.8B; only the first and the fourth quadrants were shown). It is this positive value of k_{i} that produces large amplification of BM displacement in the active case.

We plotted k_{r} and k_{i}, scaled by the tilt distance d, seperately (i.e., k_{r}d and k_{i}d), with respect to the distance from the stapes x, to understand more clearly the relation between wavenumber loci and BM responses (Figure 3.9). Only the passive case and one active case ($\alpha = 0.15$) were shown for clear illustration.

In both passive and active case, k_{r} started from a near-zero value and gradually in-

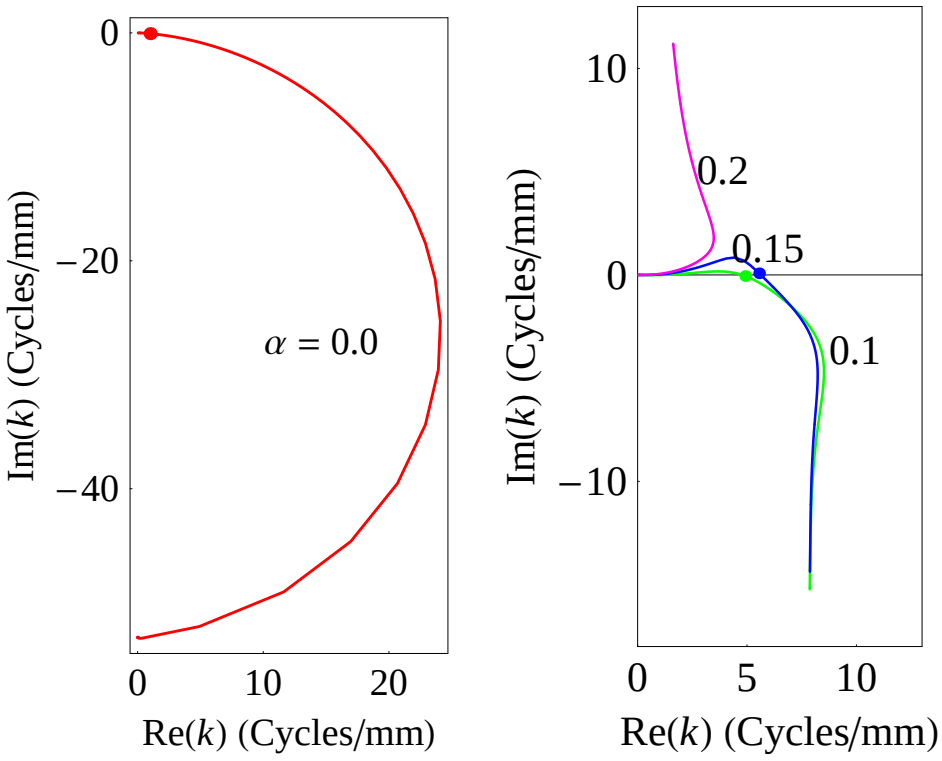

Figure 3.8: Wavenumber Loci of Traveling Wave

Wavenumber loci are different at different OHC motility factors. The input is 2 kHz pure tone. **A** When the outer hair cell motility factor $\alpha = 0.0$. **B** When $\alpha = 0.1$, 0.15, and 0.2. The dots mark the characteristic place, where the BM vibration peaks.

creased, indicating that the wave travels at a high speed, then gradually slows down at cochlear positions where the peak occurs. A dramatic difference between the passive and the active cases occurs after the peak: in the passive case, k_{r} increases to a large value then drops to a near-zero value, while in the active case, it asymptotes at non-zero value—indicating that while the wavelength remains short in the active case it becomes long again in the passive case. As for k_{i}, whereas it keeps negative in the passive case, we observed positive values right before the peak location in the active case.

Having obtained the locus of the wavenumber k, we shall now investigate other characteristics of the TW. The traveling velocity v of the wave can be calculated as ω/k and the wavelength λ is equal to $2\pi/k_{\mathrm{r}}$ or $2\pi v/\omega$ (i.e., v/f); it is proportional to the velocity. (Figure 3.10) shows the TW velocity for both a passive and an active case. The velocity at the CP is 1.94, and 0.36 $\mathrm{m/s}$ for these two cases, respectively. The corresponding wavelengths are 969, and 180 μm for the passive and active cases, respectively.

To visualize the traveling wave behavior, we plot the velocity potential in the fluid and the BM displacement, obtained using the wavenumber k we just solved for. Figure 3.11 shows the traveling wave for both the passive and an active cases. In the passive case, the BM amplitude is only about 23 dB, and the Q_{10} is calculated to be 0.6, while the active response reaches 85 dB and the Q_{10} is about 5.4. The wavelength decreases as the wave travels; near the peak (in the short-wave region), the wave also becomes more localized in the vertical direction, which cannot be simulated in a long-wave approximation model. In particular, the wave extends from the BM for about 77 μm into the fluids (from model semi-analytical simulation), which is comparable to its longitudinal wavelength.

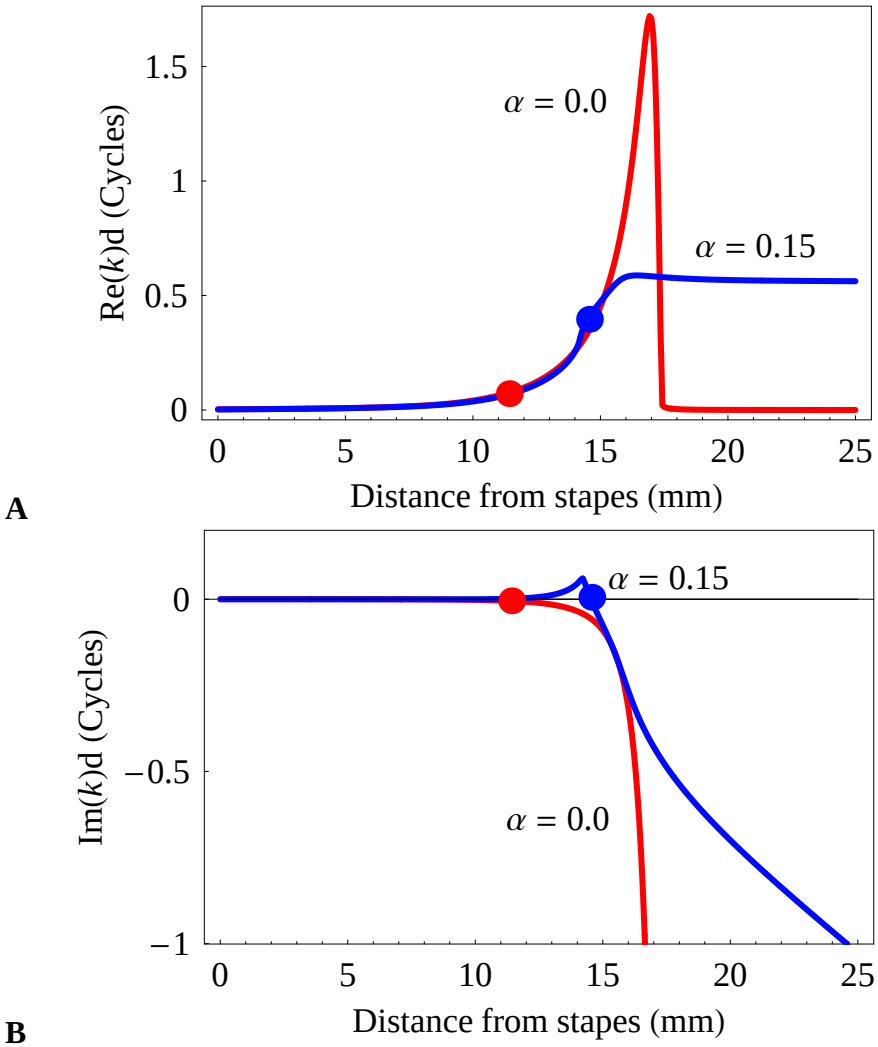

Figure 3.9: Real and Imaginary Parts of Wavenumber

The plots show the loci of k_{r} and k_{i} multiplied by the tilt distance d. The passive case ($\alpha = 0$) and the active case ($\alpha = 0.15$) are compared. **A** Real part of k. **B** Imaginary part. Input frequency is 2 kHz. Dots mark the peak locations.

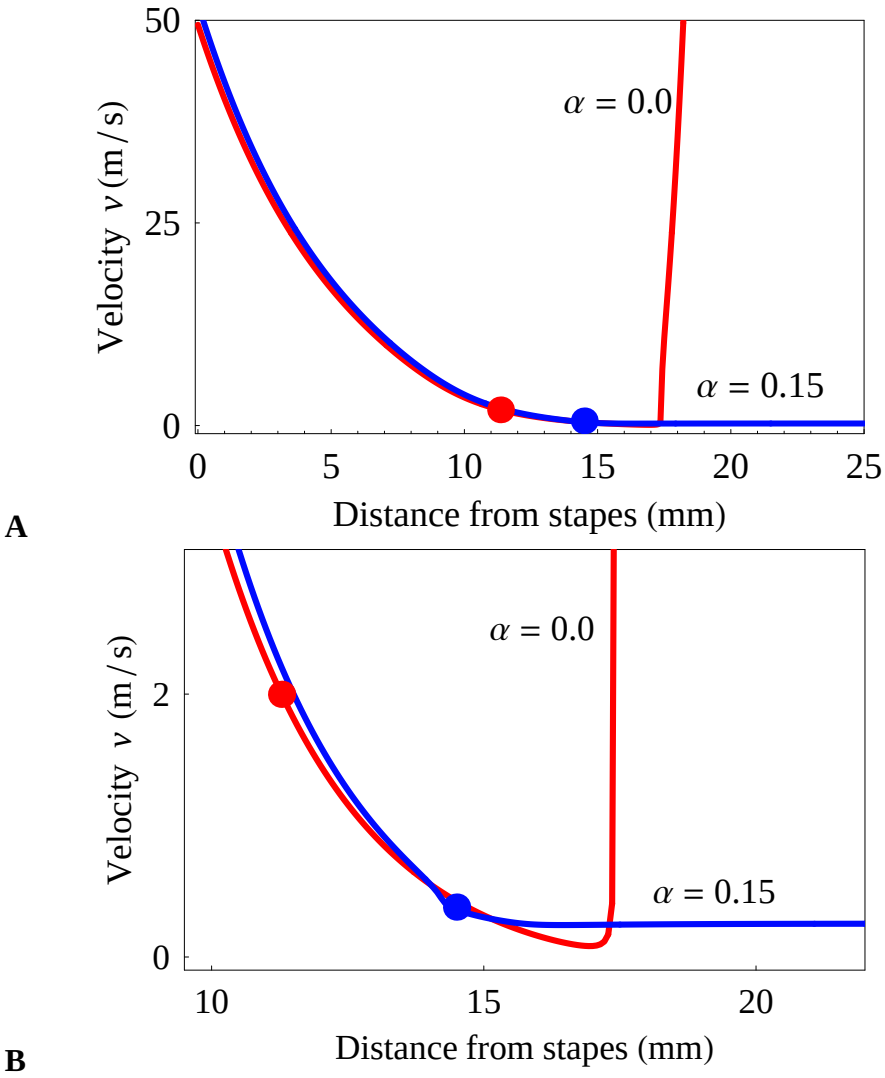

Figure 3.10: Velocity of Traveling Wave

Model simulation result using semi-analytical solutions for passive and active cases are shown. **A** Traveling wave velocity for 2 kHz pure tone input. **B** Zoom-in around the characteristic place. Red curve represents the passive case ($\alpha = 0.0$), while blue curve represents the active case ($\alpha = 0.15$). Dots mark the peak locations.

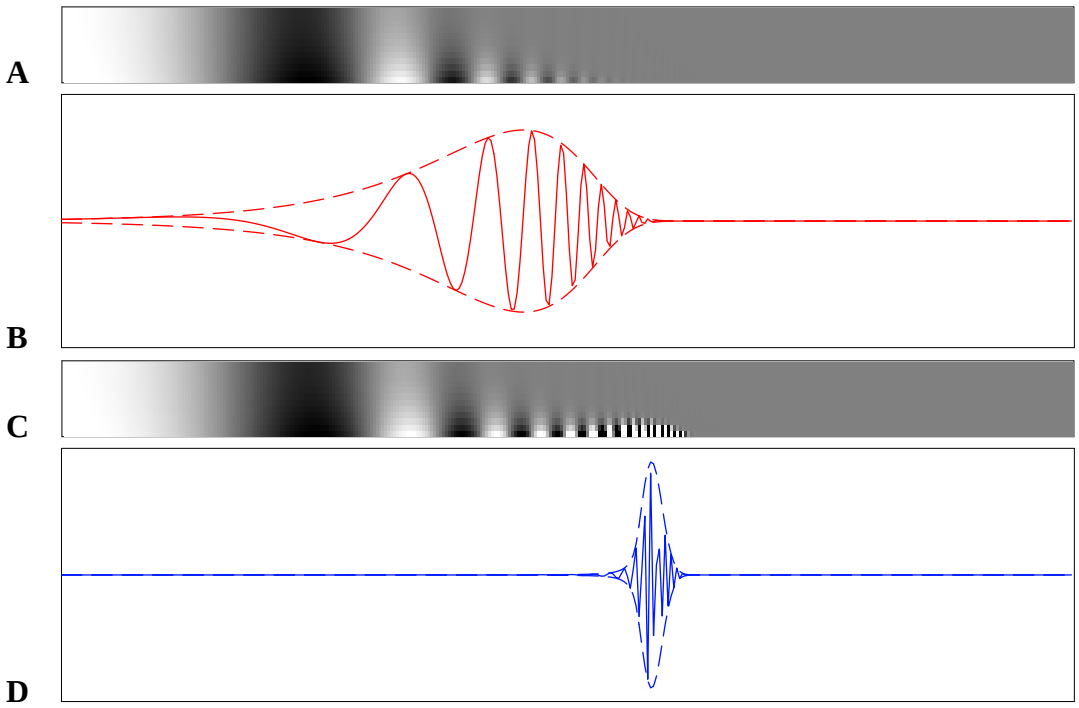

Figure 3.11: Simulated Traveling Wave in the Passive and Active Cochleae

The input frequency is 2 kHz. Passive case ($\alpha = 0$): **A** & **B**. Active case ($\alpha = 0.15$): **C** & **D**. Traveling wave (TW) in the fluid: **A** & **C**. TW along the basilar membrane: **B** & **D**. The plots for the passive and active cases are on different scale.

3.2.3 Semi-Analytical Solutions

We now proceed to perform further analytical treatment to the model in order to derive closed-form expressions that relate the traveling wave behavior, namely the wavenumber k, to cochlea's biophysical parameters. This effort will no doubt lead to more insight about the contribution of the active mechanism, ABC, to the active amplification in the cochlea.

The analysis shall focus on seeking answers to three questions that highlight the characteristic features of the wavenumber locus in the active case. First, why does the wavenumber enter the first quadrant before the peak? Second, what is the asymptotic value of the real part of the wavenumber (i.e., in the cut-off region)? Last, when is the imaginary part equal to zero? Answer to the first question will shed light on how active amplification arises. The second addresses why the wavelength remains short in the cut-off region, unlike the passive case. The third reveals how the CP depends on the model's parameters.

For convenience, we repeat here the dispersion relation (Equation 3.13) of the cochlear traveling wave in the active case (i.e., with ABC):

$$\frac{k\tanh(kh)}{1+\alpha S(x)k\tanh(kh)(\gamma e^{ikd}-e^{-ikd})/(2\rho\omega^2)}=\frac{2\rho\omega^2}{S(x)+i\omega\beta(x)+(i\omega)^2M(x)}. \quad (3.18)$$

We shall now seek solutions to the dispersion relation in the three characteristic regions of the traveling wave, namely the long-wave, short-wave, and the cut-off region. In these three regions, different assumptions and approximations will be introduced due to the varying properties of the traveling wave in order to simplify the solution process.

Long-Wave Region

The dispersion relation (Equation 3.18) can be transformed into

$$\frac{k\tanh(kh)}{1+\alpha\sqrt{\gamma}S(x)\sinh\left(ikd+\log\sqrt{\gamma}\right)k\tanh(kh)/(\rho\omega^2)} = \frac{2\rho\omega^2}{S(x)+i\omega\beta(x)+(i\omega)^2M(x)}. \tag{3.19}$$

where the term in the denominator on the left $\sqrt{\gamma}\sinh\left(ikd+\log\sqrt{\gamma}\right)$ replaced the term $\gamma e^{ikd}-e^{-ikd}$ in Equation 3.18.

The wave in the cochlear fluid and along the BM travels at a large speed near the stapes, corresponding to a long wave length. When the wave length is larger than the cochlear duct height, the cochlea region is referred to as the long-wave region. Therefore, in the long-wave region, we have $hk \ll 1$ since wavenumber k is small. Therefore, $\tanh(hk)$ can be approximated to be hk. In addition, the relation $|kd| \ll |\log\sqrt{\gamma}|$ holds in this region due to the small k and the choice of d and $gamma$ (see Table 3.1.4). Thus, Equation 3.19 is simplified as:

$$\frac{k^2h}{1+\alpha\sqrt{\gamma}S(x)\sinh\left(\log\sqrt{\gamma}\right)k^2h/(\rho\omega^2)} \approx \frac{2\rho\omega^2}{S(x)+i\omega\beta(x)+(i\omega)^2M(x)}. \tag{3.20}$$

Also, the term $\sqrt{\gamma}\sinh\left(\log\sqrt{\gamma}\right)$ is equal to $(\gamma-1)/2$. Substituting this into Equation 3.20 yields an expression of the wavenumber k:

$$k \approx \omega\sqrt{\frac{2\rho/h}{S(x)+i\omega\beta(x)+S(x)\alpha(1-\gamma)-\omega^2M(x)}}. \tag{3.21}$$

As the BM impedance in the long-wave region is dominated by its stiffness (far away from the resonance), ignoring the damping and mass gives the approximate solution:

$$k \approx \omega\sqrt{\frac{2\rho/h}{S(x)(1+\alpha(1-\gamma))}} \tag{3.22}$$

As we can see, the wave number k is proportional to the input frequency ω at any position in the long wave region. In the passive case where $\alpha = 0$, the solution of k reduces to:

$$k \approx \omega \sqrt{\frac{2\rho/h}{S(x)}}. \tag{3.23}$$

Even in the active case, since α is much less than 1 (< 0.2 given the chosen model parameters), the effect of the term $\alpha(1-\gamma)$ is rather minor—evidence that ABC does not take much effect in the long-wave region.

In terms of traveling velocity, the group velocity of the fluid is equal to the phase velocity c:

$$c = \omega/k \approx \sqrt{\frac{S(x)(1+\alpha(1-\gamma))}{2\rho/h}}, \tag{3.24}$$

which corresponds to a non-dispersive wave.

Short-Wave Region

Switching to the short-wave region, we shall seek the answer to the question of why the wavenumber locus enters the first quadrant. In the short-wave region, in the vicinity of the peak location, we observed that the real part of the wavenumber, k_{r} is far greater than the imaginary part, k_{i}. In addition, since $|k_{\mathrm{r}}h| \gg 1$, we have $\tanh(kh) \approx \tanh(k_{\mathrm{r}}h) \approx 1$. Therefore, Equation 3.18 can also be tranformed into:

$$\frac{k}{1 + i\alpha\sqrt{\gamma}S(x)\sin\left(kd - i\log\sqrt{\gamma}\right)k/(\rho\omega^2)} = \frac{2\rho\omega^2}{S(x) + i\omega\beta(x) + (i\omega)^2 M(x)}. \tag{3.25}$$

In the following derivations, we replace Ω for $\omega/\omega_{\mathrm{n}}$, where $\omega_{\mathrm{n}}(x)$ is the resonant angular frequency at the cochlear location x ($\omega_{\mathrm{n}} = \sqrt{S(x)/M(x)}$). In addition, we have

$\beta = \zeta\sqrt{S(x)M(x)} = \zeta M(x)\omega_{\mathrm{n}}$. With these substitutions, Equation 3.25 becomes:

$$(1 + i\zeta\Omega - \Omega^2)k = \frac{2\rho}{M(x)}\Omega^2 + i2\alpha k\sqrt{\gamma}\sin(kd - i\log\sqrt{\gamma}). \tag{3.26}$$

Since $|kd - i\log\sqrt{\gamma}|$ is close to 0, we have $\sin(kd - i\log\sqrt{\gamma}) \approx kd - i\log\sqrt{\gamma}$. In addition, $\Omega < 1$ as the peak occurs well before the resonance and ζ is chosen to be 0.2, so we have $\zeta\Omega \ll 1$. Thus, Equation 3.26 becomes:

$$2\alpha d\sqrt{\gamma}k^2 + i(1 - \Omega^2 - 2\alpha\sqrt{\gamma}\log\sqrt{\gamma})k - i2\rho\Omega^2/M(x) = 0, \tag{3.27}$$

Further, we ignore the term $\alpha\sqrt{\gamma}\log\sqrt{\gamma}$ since it is far less than 1 based on our parameter choice. Since $\Omega^2 \ll 1$, we ignore the $1 - \Omega^2$ term, and we have

$$2\alpha d\gamma k^2 + ik - i\frac{2\rho}{M(x)}\Omega^2 = 0. \tag{3.28}$$

Hence, we find the solution to the wavenumber in the short-wave region as:

$$k = \left(\sqrt{i16\alpha\sqrt{\gamma}\rho d/M(x)\Omega - 1} - i\right)/4\alpha d\sqrt{\gamma}. \tag{3.29}$$

From the expression of k above, we obtain its imaginary part, k_{i} as follows.

$$k_{\mathrm{i}} = \frac{\frac{\sqrt{2}}{2}\sqrt{1 + \sqrt{1 + 256\gamma d^2\alpha^2\rho^2\Omega^4/M(x)^2}} - 1}{4\alpha d\sqrt{\gamma}}. \tag{3.30}$$

Ω increases as the wave propagates, due to the decrease in ω_{n}. Thus, if $\alpha > 0$, the imaginary part of the wavenumber k, k_{i}, becomes positive, pushing the wavenumber locus into the first quadrant. Therefore, it is evident that a positive OHC motility factor is the source of active amplification.

Cut-Off Region

Now we shall look at the cut-off region, for which we transfrom Equation 3.18 into:

$$\frac{k\tanh(kh)}{1+i\alpha\sqrt{\gamma}S(x)\tanh(kh)\sin(kd-i\log\sqrt{\gamma})k/(\rho\omega^2)}=\frac{2\rho\omega^2}{S(x)+i\omega\beta(x)+(i\omega)^2M(x)}. \tag{3.31}$$

Substituting k with $k_\mathrm{r}+ik_\mathrm{i}$ in Equation 3.31 yields:

$$\alpha\sqrt{\gamma}S(x)\left(i\cosh(k_\mathrm{i}d-\log(\sqrt{\gamma}))\sin(k_\mathrm{r}d)-\cos(k_\mathrm{r}d)\sinh(k_\mathrm{i}d-\log(\sqrt{\gamma}))\right) + \frac{\rho\omega^2}{k_\mathrm{r}^2+k_\mathrm{i}^2}(k_\mathrm{r}-ik_\mathrm{i})=(S(x)-\omega^2M(x)+i\omega\beta(x))/2 \tag{3.32}$$

Substituting Ω for ω/ω_n and decomposing Equation 3.32 into the real and imaginary part yield:

$$\frac{\rho\Omega^2}{k_\mathrm{r}^2+k_\mathrm{i}^2}k_\mathrm{r}-\alpha\sqrt{\gamma}M(x)(\cos(k_\mathrm{r}d)\sinh(k_\mathrm{i}d-\log(\sqrt{\gamma})))=(M(x)(1-\Omega^2))/2, \tag{3.33}$$

and

$$\frac{\rho\Omega^2}{k_\mathrm{r}^2+k_\mathrm{i}^2}k_\mathrm{i}-\alpha\sqrt{\gamma}M(x)(\sin(k_\mathrm{r}d)\cosh(k_\mathrm{i}d-\log(\sqrt{\gamma})))=-(\zeta\Omega M(x))/2. \tag{3.34}$$

These two equations can be further reorganized as:

$$2\sqrt{\gamma}\alpha(\cos(k_\mathrm{r}d)\sinh(k_\mathrm{i}d-\log(\sqrt{\gamma})))=\Omega^2+\frac{2\dfrac{\rho}{M(x)}k_\mathrm{r}}{k_\mathrm{r}^2+k_\mathrm{i}^2}\Omega^2, \tag{3.35}$$

and

$$2\sqrt{\gamma}\alpha(\sin(k_{\mathrm{r}}d)\cosh(k_{\mathrm{i}}d-\log(\sqrt{\gamma})))=\zeta\Omega+\frac{2\frac{\rho}{M(x)}k_{\mathrm{i}}}{k_{\mathrm{r}}^2+k_{\mathrm{i}}^2}\Omega^2. \tag{3.36}$$

Dividing Equation 3.36 by Equation 3.35 results in

$$\frac{\tan(k_{\mathrm{r}}d)}{\tanh(k_{\mathrm{i}}d-\log(\sqrt{\gamma}))}=\frac{\frac{\zeta}{\Omega}+\frac{2\frac{\rho}{M(x)}k_{\mathrm{i}}}{k_{\mathrm{r}}^2+k_{\mathrm{i}}^2}}{1+\frac{2\frac{\rho}{M(x)}k_{\mathrm{r}}}{k_{\mathrm{r}}^2+k_{\mathrm{i}}^2}} \tag{3.37}$$

Since $|k_{\mathrm{i}}d|\gg 1$ in the cut-off region, and $\log(\sqrt{\gamma})\approx -0.6$, we have $\tanh(k_{\mathrm{i}}d-\log(\sqrt{\gamma}))\approx -1$. Thus, we have:

$$-\tan(k_{\mathrm{r}}d)=\frac{\frac{\zeta}{\Omega}+\frac{2\frac{\rho}{M(x)}k_{\mathrm{i}}}{k_{\mathrm{r}}^2+k_{\mathrm{i}}^2}}{1+\frac{2\frac{\rho}{M(x)}k_{\mathrm{r}}}{k_{\mathrm{r}}^2+k_{\mathrm{i}}^2}} \tag{3.38}$$

Since $\Omega\gg 1$ near the apex, $\zeta/\Omega\approx 0$. Also because $|k_{\mathrm{i}}|\gg|k_{\mathrm{r}}|$ near the apex, we have:

$$\frac{\frac{\zeta}{\Omega}+\frac{2\frac{\rho}{M(x)}k_{\mathrm{i}}}{k_{\mathrm{r}}^2+k_{\mathrm{i}}^2}}{1+\frac{2\frac{\rho}{M(x)}k_{\mathrm{r}}}{k_{\mathrm{r}}^2+k_{\mathrm{i}}^2}}\approx 0. \tag{3.39}$$

Therefore, Equation 3.38 leads to:

$$\tan(k_{\mathrm{r}}d)\approx 0, \tag{3.40}$$

which gives the asymptotic value of k_{r} as π/d. This result predicts that the wavelength gets

no shorter than twice the tilt distance d, and explains why k_{r} asymptotes to the same value independent of α. For a tilt distance $d = 71\ \mu m$, this estimate yields the value of 44.2, which is close to the simulation result of 36.1.

At the Characteristic Place

It is also instructive to investigate the model's responses at the CP as both the magnitude and phase of the BM response at the CP reflect the characteristics of the cochlear mechanics, as well as encode the input signal's property. As we already know, $k_{\mathrm{i}} = 0$ corresponds to the peak in the active case. Therefore, Equation 3.33 and Equation 3.34 become:

$$\frac{\rho\Omega^2}{k_{\mathrm{r}}} - \alpha\sqrt{\gamma}M(x)(\cos(k_{\mathrm{r}}d)\sinh(-\log(\sqrt{\gamma}))) = (M(x)(1-\Omega^2))/2, \tag{3.41}$$

and

$$\alpha\sqrt{\gamma}M(x)\sin(k_{\mathrm{r}}d)\cosh(-\log(\sqrt{\gamma})) = \zeta\Omega M(x)/2. \tag{3.42}$$

Around the peak, we have $\sin(k_{\mathrm{r}}d) \approx \pi - k_{\mathrm{r}}d$ since $k_{\mathrm{r}}d \approx \pi$ (by linearization $\sin(x)$ around π). Also, we have $\sqrt{\gamma}\sinh(-\log\sqrt{\gamma}) = (1-\gamma)/2$ and $\sqrt{\gamma}\cosh(-\log\sqrt{\gamma}) = (1+\gamma)/2$.

Substituting $m = M(x)/2\rho d$ (the ratio between the BM mass and fluid mass of depth d), Equation 3.41 becomes

$$\begin{aligned} \frac{\rho\Omega^2}{k_{\mathrm{r}}} - \alpha M\frac{1-\gamma}{2}\cos k_{\mathrm{r}}d &= (M(x)(1-\Omega^2))/2, \\ \Longrightarrow \alpha(1-\gamma)\cos k_{\mathrm{r}}d &= \Omega^2(1+\frac{1}{mk_{\mathrm{r}}d}) - 1 \end{aligned} \tag{3.43}$$

for the real part and Equation 3.42 becomes

$$\alpha(1+\gamma)(\pi - k_{\mathrm{r}}d) = \zeta\Omega \tag{3.44}$$

for the imaginary part of the dispersion relation.

Solving Equation 3.44 for k_{r}, we obtained its solution at the peak position:

$$k_{\mathrm{r}} = \frac{\pi}{d} - \frac{\zeta\Omega}{\alpha d(1+\gamma)}. \tag{3.45}$$

With $\cos(k_{\mathrm{r}}d) \approx -1$, Equation 3.43 becomes:

$$\frac{\Omega^2}{d} + \alpha m k_{\mathrm{r}}(1-\gamma) = m k_{\mathrm{r}}(1-\Omega^2). \tag{3.46}$$

Substituting the expression of k_{r} at the peak (Equation 3.45) into Equation 3.46 yields:

$$-\zeta\Omega^3 + \alpha(1+\gamma)(\pi + 1/m)\Omega^2 + \zeta(1-\alpha(1-\gamma))\Omega + \pi(\alpha(1-\gamma)-1) = 0 \tag{3.47}$$

Ignoring the Ω^3 term due to $\Omega \ll 1$ at the CP, we obtained a second-order polynomial equation in Ω:

$$\alpha(1+\gamma)(\pi + 1/m)\Omega^2 + \zeta(1-\alpha(1-\gamma))\Omega + \pi(\alpha(1-\gamma)-1) = 0 \tag{3.48}$$

Solving Equation 3.48 for Ω, we then obtained:

$$\Omega = \frac{\zeta(\alpha(1-\gamma)-1) + \sqrt{(\alpha(1-\gamma)-1))^2\zeta^2 + 4\pi\alpha^2(1+\gamma)^2(1-\gamma(1-\gamma))(\pi+1/m)}}{2\alpha(1+\gamma)(\pi+1/m)} \tag{3.49}$$

Substituting model parameters in the expression of Ω above gives values of Ω at the CP:

0.48, 0.49, and 0.49 when α is chosen to be 0.1, 0.15, and 0.20, respectively. These values verified the assumption we made earlier that $\Omega^2 \ll 1$ at the CP. Since $\alpha(1-\gamma) \ll 1$ and $\gamma(1-\gamma) \ll 1$, the solution above can be further simplified as:

$$\Omega = \frac{\sqrt{\zeta^2 + 4\pi\alpha^2(1+\gamma)^2(\pi + 1/m)} - \zeta}{2\alpha(1+\gamma)(\pi + 1/m)} \tag{3.50}$$

This simplified solution of Ω yields 0.49, 0.52, and 0.53 for α is chosen to be 0.1, 0.15, and 0.20, respectively. On the other hand, the results from the semi-analytical simulation approach described in the previous section (Figure 3.9) were 0.51, and 0.51 for $\alpha = 0.1$ and 0.15, respectively (diverged at $\alpha = 0.2$). Therefore, the predictions in Equation 3.50 are in good agreement with the simulation based on numerical solution of the wavenumber k.

Substituting the expression of Ω in Equation 3.50 into the expression of k_{r} (Equation 3.45) yields:

$$k_{\mathrm{r}} = \frac{\pi}{d} - \zeta\frac{\sqrt{\zeta^2 + 4\pi\alpha^2(1+\gamma)^2(\pi + 1/m)} - \zeta}{2\alpha^2 d(1+\gamma)^2(\pi + 1/m)}. \tag{3.51}$$

Qualitatively speaking, Equation 3.51 clearly shows that at the CP, the wave propagation speed is determined by the BM-to-fluid mass ratio m, BM's damping ratio ζ, the tilt distance d, the OHC motilty factor α, and the forward-to-backward ratio γ. Quantitatively, k_{r} is a little smaller at the CP than the asymptote value of k_{r} (i.e., π/d in the cut-off region). This solution for k_{r} evaluates to 23.8, 26.5, and 27.4 when the α is set to be 0.1, 0.15, and 0.20, respectively. In comparison, the semi-analytical simulation gives 23.6 and 25.9 for α = 0.1 and 0.15, which indicates that the approximations in Equation 3.51 are quite good.

We have solved a linear version of the active cochlear model that includes our cochlear

amplifier mechanism, ABC, using a semi-analytical approach. The analysis provided answers to several important questions about how the parameters of ABC, namely the OHC motility factor α and the forward-to-backward ratio γ, give rise to distinctive locus of the wavenumber k, thereby the active amplification in the cochlea. We shall now proceed to investigate the impedance of the BM based on some of the results we have obtained through the SAS.

3.2.4 Impedance of the Basilar Membrane

Impedance quantifies resistance to motion. While mechanical impedance is defined as the ratio of the driving force to the velocity it imparts, effective acoustic impedance of the BM is calculated as the pressure difference acting on a BM segment divided by the velocity of that segment. For a passive BM (without OHC forces exerted on it), the real part of the acoustic impedance is the BM damping and the imaginary part is the difference of BM mass and stiffness. In contrast, for an active BM (with OHC forces exerted on it), the real part and the imaginary part of the impedance will be altered due to the additional OHC forces. Thus, exploration of the acoustic impedance of the BM shall give us more insight about the property of OHC forces, or what contribution OHC forces would make to the BM's vibration, which eventually leads to large amplification and sharp tuning.

We derived the expression of the effective impedance of BM, z_{m}, based on its definition. For convenience, we repeated the solution form of the velocity potential of the fluid ϕ:

$$\phi(x, y, t) = B(x) \cosh(ky) e^{i(\omega t - kx)}, \tag{3.52}$$

where all the variables have the same physical meaning as that in the previous section.

From here, we obtained the BM velocity, V_{BM}, in the vertical axis as:

$$\begin{aligned} V_{\mathrm{BM}}(x,y,t) &= -\frac{\partial\phi(x,y,t)}{\partial y}|_{y=h} \\ &= B(x)\sinh(kh)e^{i(\omega t-kx)}. \end{aligned} \tag{3.53}$$

Also, based on Equation 3.5, we obtained the pressure difference that is applied to the BM as:

$$\begin{aligned} P_{\mathrm{d}}(x,y,t) &= 2i\rho\omega B(x)\cosh(ky)e^{i(\omega t-kx)}|_{y=h} \\ &= 2i\rho\omega B(x)\cosh(kh)e^{i(\omega t-kx)}. \end{aligned} \tag{3.54}$$

Then we derived the expression of z_{m} as:

$$\begin{aligned} z_{\mathrm{m}} &= \frac{P_{\mathrm{d}}}{V_{\mathrm{BM}}} \\ &= -\frac{2i\rho\omega}{k\tan(kh)}. \end{aligned} \tag{3.55}$$

Based on the loci of wavenumber k that we have obtained previously, we obtained and plotted the real and imaginary components of the BM impedance (Figure 3.12) at 2 kHz pure-tone input. The reactive components of the effective BM impedance in the passive and active cases are almost the same (Figure 3.12B), indicating that BM stiffness and mass are not altered by OHC motility. Meanwhile, the major difference between the passive and the active case lies in the resistive component of the BM impedance (Figure 3.12A), which implies that the inclusion of ABC actually modifies the damping. Specifically, compared to the passive case, the damping in the active case is reduced (by half) before the characteristic place and is increased after the CP. Furthermore, close to the peak location, at about 14.6 mm, the damping becomes negative, then rises abruptly to a positive value at the CP. As a

result, the BM gains its large peak amplitude around this position and then the vibration's amplitude is cut off sharply.

We plotted the normalized impedance (Figure 3.13) by dividing it by the critical damping (i.e., mass and stiffness component at resonance; $\sqrt{S(x)M(x)}$). The resistive component of the normalized impedance yields the damping ratio. Clearly, the damping ratio in the active case is no longer constant; instead, it reduced from 0.2 to a value closer to zero and becomes negative right before the CP. In contrast, the reactive components of the impedance in both cases are very similar—their CPs are far from the mass-dominated region.

3.2.5 Comparison of Numerical and Analytical Solutions

We have solved the linear active model using both numerical and semi-analytical methods. It is helpful to check how well the results of the two methods agree with each other. Comparing the results in Section 3.1.4 and in this section, the BM responses obtained using the finite-difference (FD) method and the semi-analytical (SA) method are quite close to each other (Figure 3.14).

While the BM's amplitude responses are quite close to each other, the major difference between the two approaches is in the phase responses. The FD method results in phase plateau in the cut-off region while the SA approach does not. This is because of the fact that in our SA method when solving the wavenumber k, we only track the traveling wave mode while in the FD simulation, all the modes were found through solving the set of differential equations. In an attempt to seek quantitative agreement between numerical simulation and analytical solution, Watts concluded that inclusion of an additional degree

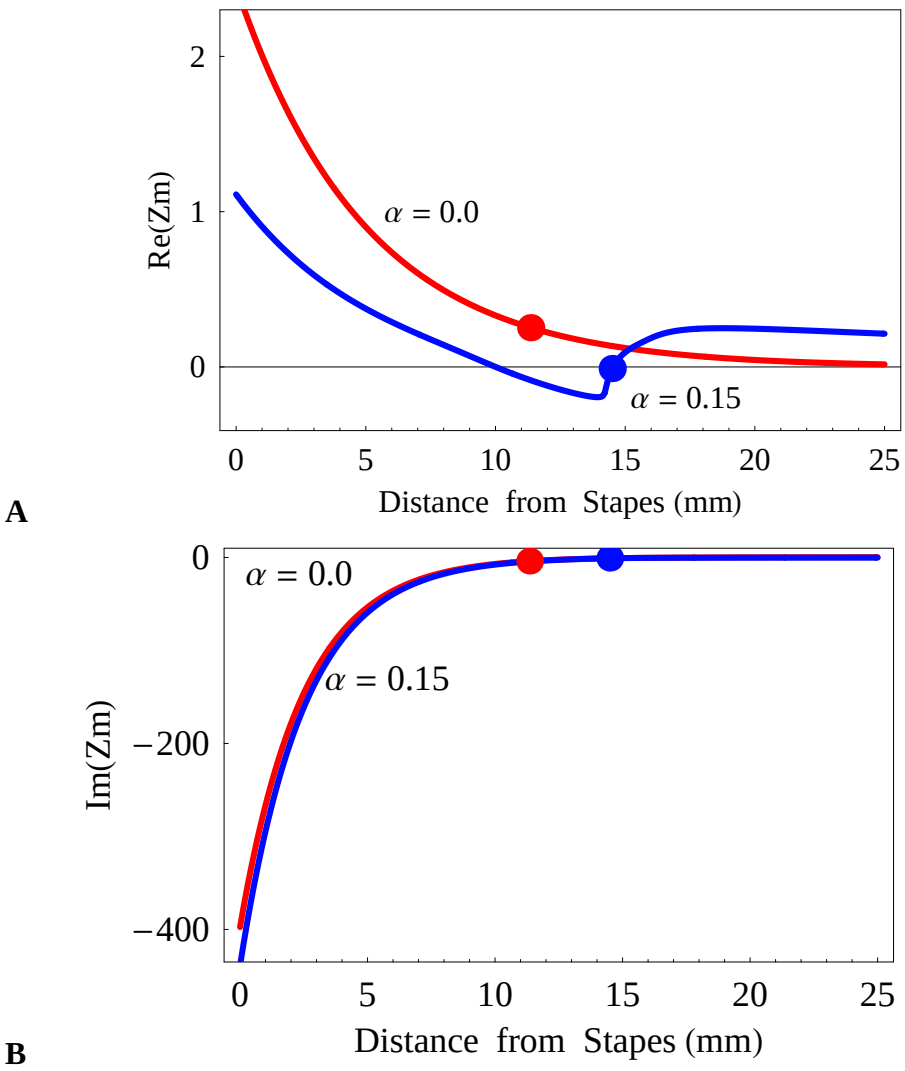

Figure 3.12: Basilar Membrane Effective Impedance

The basilar membrane impedance at 2 kHz pure tone input. **A** $\mathrm{Re}(\mathrm{z_m})$, the resistive component of the impedance. **B** $\mathrm{Im}(\mathrm{z_m})$, the reactive component of the impedance. *Red*: the passive case ($\alpha = 0.0$). *Blue*: the active case ($\alpha = 0.15$). The dots mark where the peak occurs in both cases. The difference between passive and active cases mainly lies in the resistive component of the impedance, in which negative damping is responsible for the active cochlear responses.

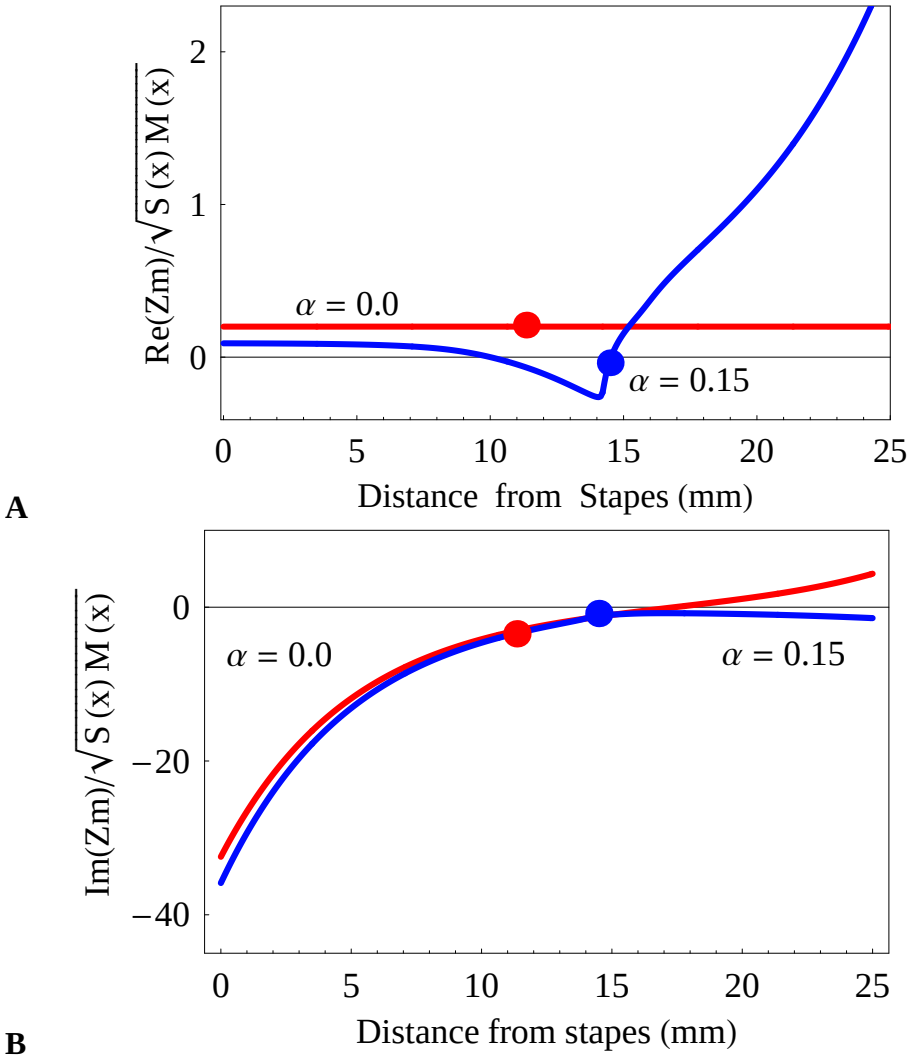

Figure 3.13: Basilar membrane Effective Impedance (Normalized)

The basilar membrane impedance normalized by the ctritical damping, $\sqrt{(S(x)M(x))}$. The input and data are the same as that in Figure 3.12. **A** Resistive component, or the damping ratio. **B** Reactive component. Red curve represents the passive case (α = 0.0), while blue curve represents the active case (α = 0.15). The dots mark where the peaks occur. As expected, the damping ratio in the passive case is a constant (i.e., 0.2). In contrast, the damping ratio in the active case becomes negative right before the peak while it is only affected slightly near the base by the inclusion of ABC.

of freedom, a second wave mode, addresses the issue effectively [6].

Using the SA method, we observed a bifurcation at $\alpha = 0.2$ (see Figure 3.8). The wavenumber locus goes into the first quadrant and does not return to the fourth quadrant, corresponding to an exploding BM displacement response. Our numerical simulations, however, do not show this bifurcation at larger values of α. When α increases, the numerical solution simply gives rise to increased peak height. We think that the bifurcation in the SA solution might be due to the way the roots of the dispersion relation are found, which is very sensitive to initial values.

3.2.6 Spatial Filter

An instructive perspective on the ABC mechanism is to think of ABC as a spatial filter that is imposed on the traveling wave along the BM (Figure 3.15). The basal tilt of outer hair cells and the apical tilt of phalangeal processes help selectively amplify the traveling wave along the basilar membrane. Near the base, the wavelength is long relative to the cochlear duct height and also the tilt distance. Positive feedforward outer hair cell forces and negative feedbackward forces tend to cancel each other, and no extra energy is pumped into the traveling wave. In contrast, near the characteristic place, the wavelength is short and comparable to the tilt distance, thus forward and backward outer hair cell forces more or less reinforce each other, enhancing the basilar membrane motion, thereby producing amplification near the peak.

To validate the spatial filter concept, we investigated the phase difference between the source and the target BM segments of OHC forces. In our simulation, this corresponds to the phase difference between adjacent stages (Figure 3.16A). Clearly, when the traveling

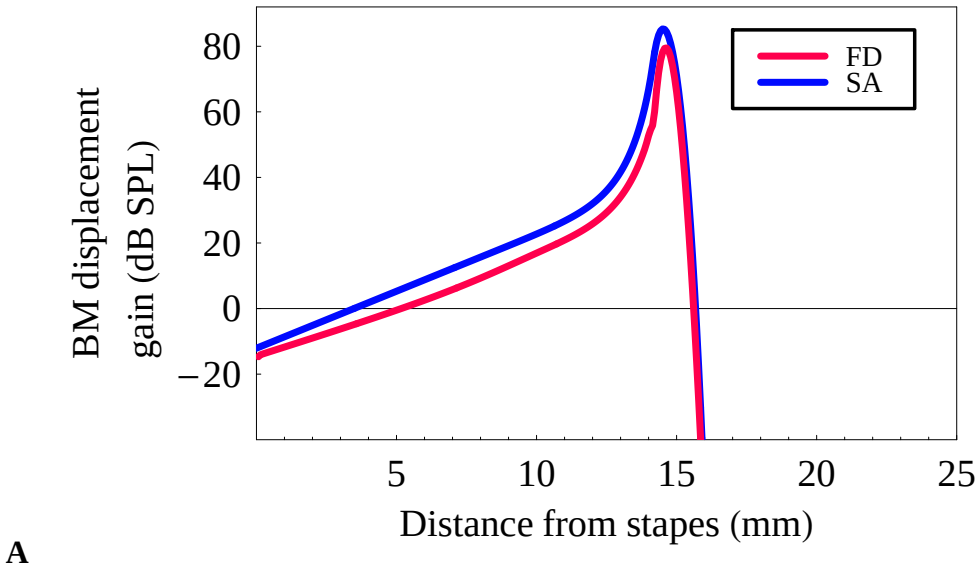

A

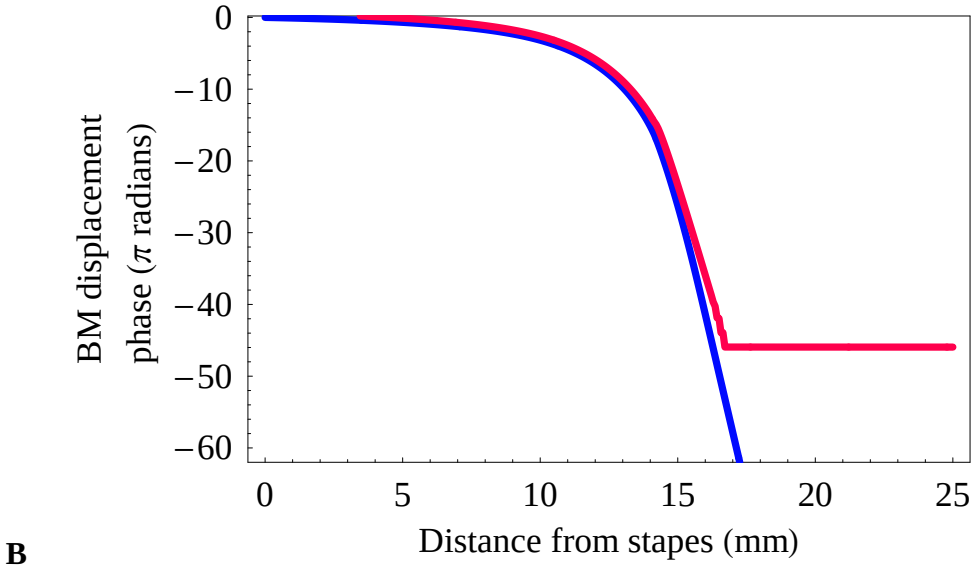

B

Figure 3.14: Comparison Between Numerical and Semi-Analytical Solutions

The basilar membrane responses are in good agreement with each other using the two approaches. FD: Finite-difference. SA: Semi-analytical.

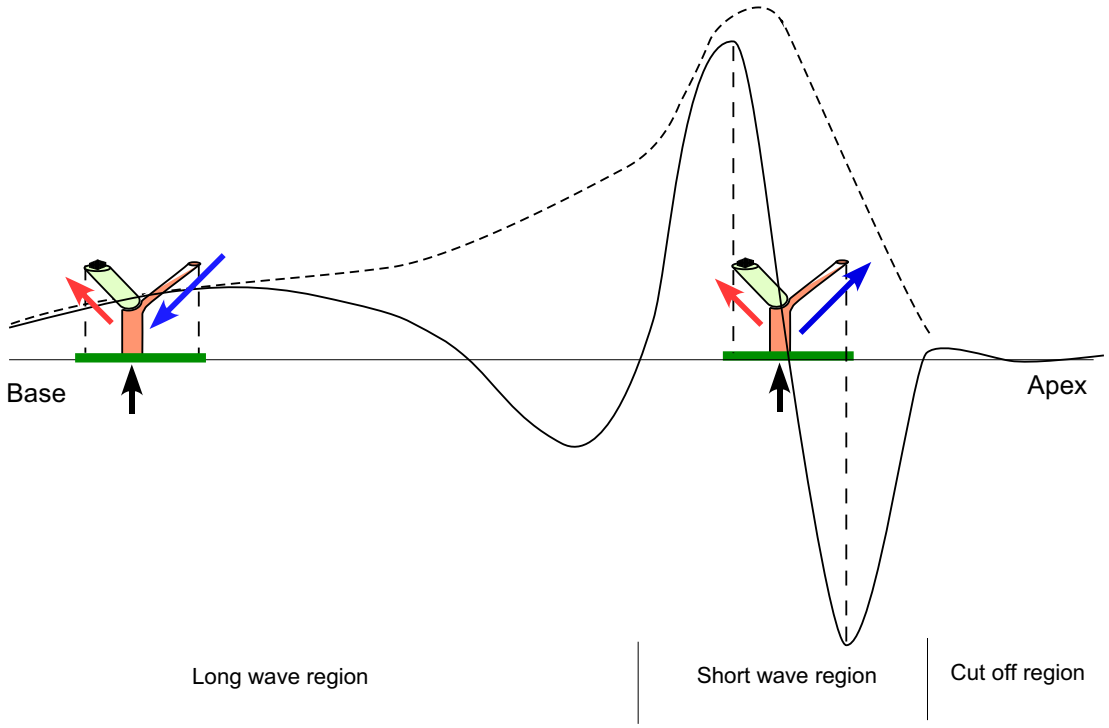

Figure 3.15: Concept of Spatial Filter

The tilts of both outer hair cells and the phalangeal process (see Figure 3.1 for structure details) is shown, overlapping with a snapshot of the traveling wave (its envelop is denoted by the dashed line). In the long-wave region near the base, feedforward and feedbackward forces due to outer hair cell motility tend to oppose or cancel each other, resulting in no amplification. In the short-wave region, they tend to reinforce each other, resulting in large amplification. In other words, feedforward and feedbackward forces work in concert to amplify the traveling wave, only when the wavelength is short and comparable to the tilt distance. Therefore, the tilt along the cochlea work as a spatial filter.

wave is short, the phase difference between neighboring BM segments increases, reaching about $\pi/2$. This increasing phase difference activates the ABC because feedforward and feedbackward OHC forces now act in concert, instead of in opposition, such that the BM receives net positive energy. Note that the $\pi/2$ phase difference does not occur at the peak position, but a little basal to it, which concurs with the notion that this energy boosts the BM's motion. Moreover, the $\pi/2$ phase difference occurs in the region where negative damping is achieved in the cochlea. In addition, it is worth noting that the phase difference becomes closer to π at cochlear positions away from the peak toward the apex (Figure 3.16A), thus feedforward and feedbackward forces will oppose each other and get canceled again.

Figure 3.16B plots the damping ratio (normalized real part of the BM effective impedance) with the two zero-crossing points indicated. The region between the two lines, exhibiting negative damping, delimits the region where the cochlear amplifier takes effect.

3.3 The Nonlinear Model: Formulation and Simulation

In order to model nonlinear cochlear behavior, we extend the linear active model to a nonlinear active model by incorporating the saturating property of OHC forces. The saturation of OHC forces is assumed to be the origin of the cochlear nonlinearity. The assumption that the OHC forces have a saturation property is supported by the physiological data presented in Chapter 2: the OHC's receptor potential saturates with the acoustic pressure and the OHC's cell body length change saturates with the receptor potential. Based on these observations, we use the saturating profile shown in Figure 3.13 to model the relation between OHC force and BM displacement.

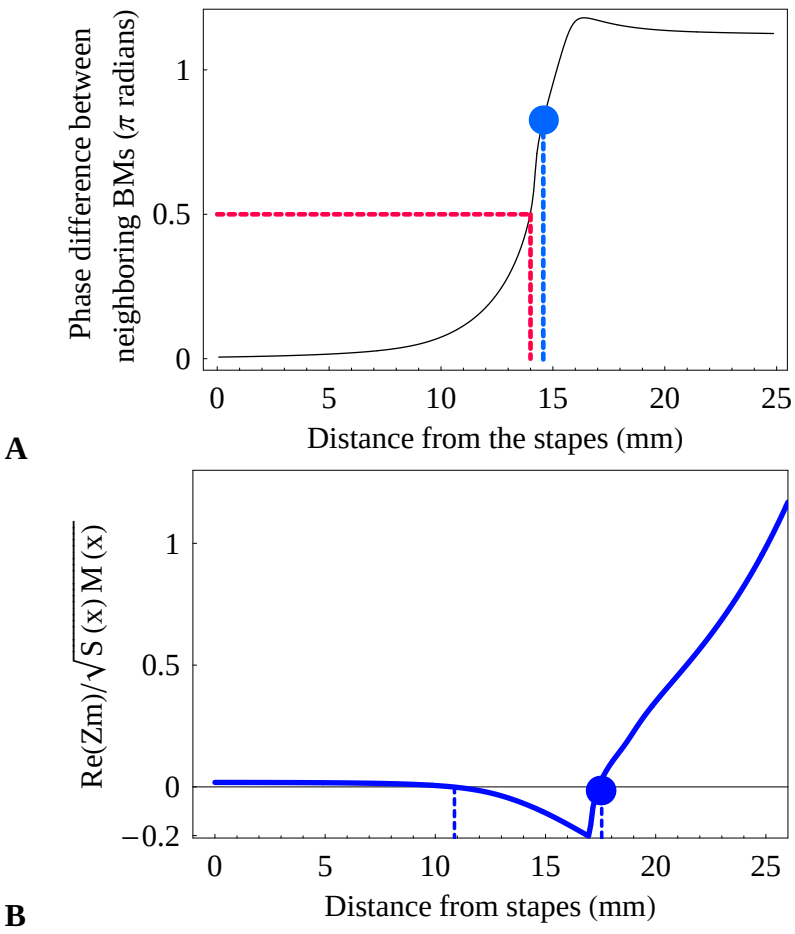

Figure 3.16: Phase Difference and Damping ratio

A Phase difference between neighboring stages. Dashed lines label $\pi/2$, the basilar membrane (BM) characteristic place, and the peak location. **B** Damping ratio (Real part of the BM effective impedance, normalized by critical damping) with the zero-crossings labeled. The longitudinal span between the two dashed lines is where the cochlear amplifier mechanism, active bidirectional coupling (ABC), takes effect.

For simplicity, the present model assumes that OHC forces saturate with a symmetric profile for both contraction and elongation. This curve is a hyperbolic tangent ($\tanh$). It is applied to both the feedforward and feedbackward OHC force terms in Equation 3.6. Thus, the saturated OHC force was modeled as:

$$F_{\mathrm{OHC}}(i) = A(\tanh(\frac{\alpha S(i)\gamma\delta(i-d)}{A}) - \tanh(\frac{\alpha S(i)\delta(i+d)}{A})), \tag{3.56}$$

where A determines the saturation level of OHC forces.

3.3.1 Compressive Growth

In our nonlinear active model, we investigated the compressive growth of BM responses at high input levels, a phenomenon that is intensively studied, and accounted for by the saturation of OHC forces. We stimulated the model with a 5 kHz pure tone at various intensities and obtained BM velocity responses (Figure 3.18). The input level was increased in 20 dB steps. Only 150 BM segments were used to save computation time. The integration time and the size of the integration step were chosen to be 40 ms and 4 μs (i.e., 10,000 steps), respectively, such that the transient responses decayed, at least within the region concerned (i.e., from the base to the position a little apical to the peak).

Clearly seen from Figure 3.18A, the BM responses becomes more broadly tuned with increasing input levels. With input level at 0 or 20 dB (corresponding to stapes displacement at 1 pm), the BM velocity response shows a large peak and sharp tuning ($Q_{10} = 4.2$ and 5.3, respectively); as the input increases, the BM response grows in a compressive manner and becomes more broadly tuned. When input level is 100 dB, the BM response resembles the passive cochlea's response ($Q_{10} = 1.6$). As a result, the input dynamic range

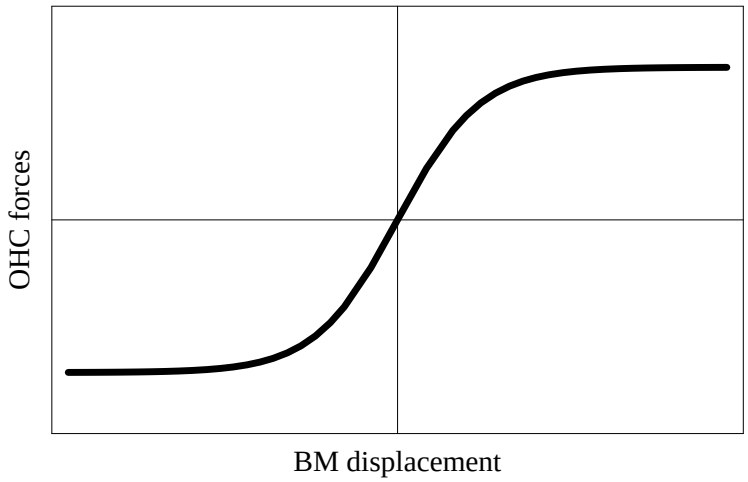

Figure 3.17: Saturating Profile of Outer Hair Cell Force

This profile between outer hair cell (OHC) forces and basilar membrane (BM) displacement approximates physiological data: the OHC receptor potential saturates with acoustic pressure and the OHC's cell body length change saturates with the receptor potential. For simplicity, a symmetric form was used for the saturation profile.

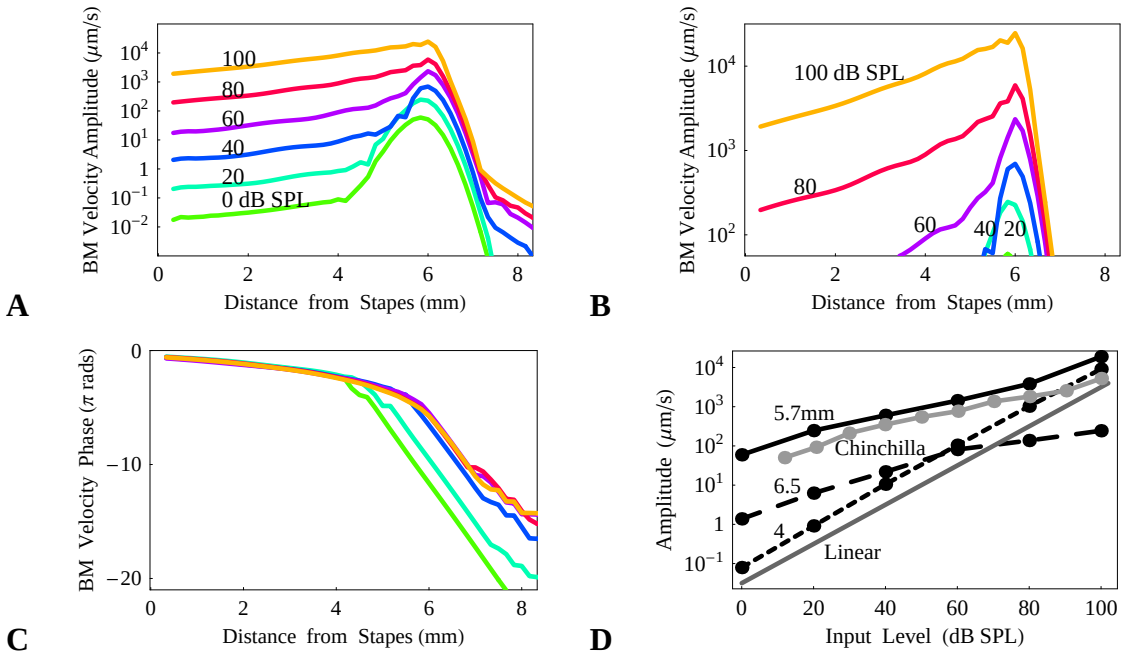

Figure 3.18: Cochlear Nonlinearity—Compressive Growth in the Model

Basilar membrane (BM) velocity responses at various input intensities. **A** BM velocity amplitude grows in a compressive manner, exhibiting sharp tuning at low input levels while showing broad tuning (passive behavior) at high levels. Only part of the cochlea (0-8mm) is shown. **B** Partial plots that highlight the small localized cochlear region that is stimulated by low-level sound, compared to much broader activity at high sound levels. **C** BM velocity phase responses. They are almost independent of input levels. **D** BM velocity amplitude versus input level at three different cochlear locations: 4 mm, 5.7 mm (where the BM peaks at 0 dB SPL), and 6.5 mm. Near the base, the BM shows linearly increasing responses with input levels; at and apical to the peak, the BM shows nonlinear (saturating) responses (i.e., compression at high input levels).

of 100 dB is compressed by the cochlea, yielding 50.1 dB compression, which is comparable to physiological data [47]. Note that in the region basal to the peak location, the BM response increases proportionally with the input level.

This peak-specific high-level compression is further evident when BM responses at three different cochlear positions were plotted against the input intensity (Figure 3.18D). These cruves are also called the input-output function of the BM. At a cochlear location before the peak where $x = 4$ mm (near the base), the input-output function is a straight line with a close-to-unity slope (1.01-1.06). In other words, the BM response near the base increases proportionally with the input intensity. At the peak where $x = 5.7$ mm (the CP at the lowest input level in the simulation), the input-output function showed varying slopes at low, medium, and high sound levels, which are 0.62, 0.40, and 0.70, respectively. The BM response around the peak shows saturation at medium to high input levels, evidence of compressive growth. At a position that is a little apical to the CP where $x = 6.5$ mm, the BM velocity also shows saturation with a slope of 0.48 at high input levels.

For comparison, we also plotted the input-output function of the BM at the peak of chinchilla cochlea's responses (from [47]; Figure 3.18D). As can be seen, our model simulation is in good agreement with physiological data with the similar saturation profile. Therefore, the nonlinear cochlear model with saturation of OHC forces was shown to be capable of model the compressive growth in the biological cochlea.

3.3.2 Two-Tone Suppression

In a nonlinear cochlear model, frequency components of the input sound are expected to interact with one another. When two tones are presented to the cochlea, suppression is

observed, known as two-tone suppression. That is, the response to one tone is reduced in the presence of the other one. This phenomenon occurs at three levels: the BM vibration, the IHC membrane voltage, and the auditory nerve discharge (action potentials). The main features of mechanical two-tone suppression are at least qualitatively similar to that of two-tone rate suppression in the auditory nerve [48]. Therefore, we investigate this interference phenomena at the BM level in our cochlear model (i.e., with saturating ABC).

Our model showed two-tone suppression both when the suppressor frequency is higher (high-side) and lower (low-side) than the probe frequency. We used an 8 kHz probe tone, a 10 kHz high-side suppressor tone, and a 6.4 kHz low-side suppressor tone, of various intensities. The BM input-output curves (BM velocity versus input level) at the CP (Figure 3.19) show that for both the high-side (Figure 3.19A and Figure 3.19B) and low-side (Figure 3.19C and Figure 3.19D) cases, compression decreases with increasing intensity. Consequently, the saturating BM input-output curve obtained for the probe tone alone becomes almost linear when an intense suppressor tone is simultaneously present.

The mechanism underlying two-tone suppression has been ascribed to the saturating profile of the OHC input-output curve (i.e., the OHC receptor potential versus sound pressure) [18, 79]. In our model, the louder suppressor drives the OHC into saturation so that the probe response is reduced. For low-side suppression (Figure 3.19C& D), the probe tone response is directly suppressed by the suppressor tone. In contrast, for high-side suppression (Figure 3.19A & B), the suppressor response acts by suppressing the probe-tone response basal to the CP of the probe-tone response, where negative damping occurs for the probe tone.

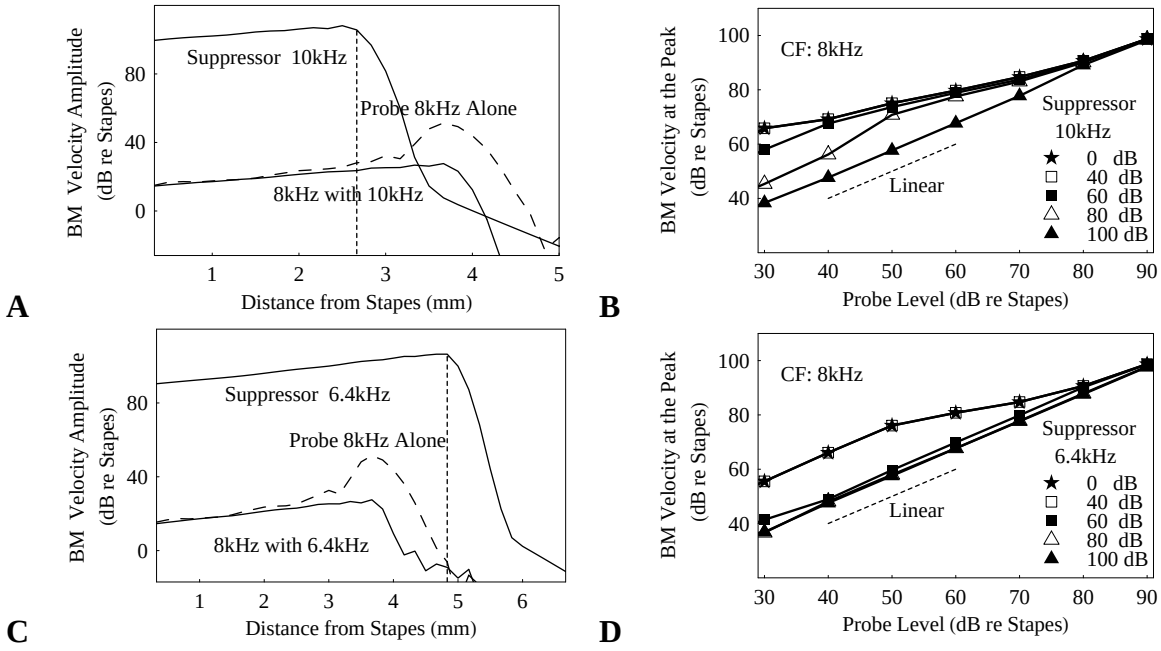

Figure 3.19: Nonlinearity: Two-Tone Suppression in the Model

A The basilar membrane (BM) velocities (in dB re Stapes) at the characteristic position at which the CF is near the probe tone frequency 8kHz versus the probe tone intensity. Increasing suppressor tone intensity(from zero to 100 dB) turns the curve from nonlinear to linear relation. **B** The BM velocity amplitude for the probe 8kHz alone, the suppressor 10kHz, and 8kHz with 10kHz. **C** The BM velocities at the characteristic position at which the CF is near the probe tone frequency versus the probe tone intensity. Increasing suppressor tone intensity(from zero to 100 dB) turns the curve from nonlinear to linear relation. **D** The BM velocity amplitude for the probe 8kHz alone, the suppressor 6.4kHz, and 8kHz with 6.4kHz.

3.4 Model Evaluation

We have presented our model simulation results and showed that the present active cochlear model—by incorporating the cochlear amplifier mechanism, ABC—is able to reproduce the characteristic cochlear responses. We shall now evalaute the model through discussing several issues that are related to the model's performances.

Given the fact that the cell diameters of OHCs and DCs are much larger than the BM transverse fiber width [18], we need to explore the effect of discretization on model simulation results. Discretizing the BM into larger number of segments does not affect the simulated BM responses as long as the tilt distance d is fixed. Without loss of generality, we always use an BM segment width that is an integer fraction of the tilt distance d. For example, we doubled the discretization step number, which decreases the BM segment length Δ to be 0.035mm, while we kept the tilt distance d to be the same as 0.071 mm. This resulted in the configuration that each BM segment sends and receives coupling to and from BM segments that are two-segment upstream (basalward) and downstream (apicalward) away from the segment in question, respectively, instead of to and from its immediate neighbors. Reaults of the simulation under such configuration showed that discretization does not affect model responses.

Previous models (e.g., [15]) included the OHC low-pass filtering in the cochlear amplifier. However, such concern has been largely cleared by newly accumulated evidence showing that the limiting frequency of the operating motor in the mammalian OHCs is up to 25 kHz [103]. Thus, OHC electromotility is fast enough, especially for human hearing. Theoretical analysis of OHC receptor potentials showed that the corner frequency of low-pass filtering could be extended into the audio range due to the membrane-voltage-dependent capacitance [104]. According to these findings, there is no need in our model to

include low-pass filtering effect in OHCs.

The focus of this model is to help explore a plausible way in which OHCs forces are delivered through the unique architecture of the OC. Our model seeks to capture the major anatomical features of the cochlear partition and to verify their role in reproducing realistic cochlear responses. We did not attempt to include all the possible roles that every contitutional component in the OC plays in the cochlear amplifier. For example, we did not include the tectorial membrane's inertial mass against which outer hair cells can exert forces [105]) nor its essential role in generating the shear force that deflects OHCs' stereocilia. However, the functional role of the tectorial membrane was implicitly included; it was just not modeled by mathematical variables.

There is room for the model to be extended to include more details in the Oc that have been brought to the attention of cochlear physiologists. For example, the organ of Corti shows morphological differences along the length of the cochlea—difference in OHCs' properties between the basal and apical regions are particularly relevant. First, despite fairly constant diameter, OHCs' length varies: relatively short near the base while relatively long in the apex [106]. Second, OHCs are oriented at varying angles along the radial direction near the base and apex: they are oriented almost in parallel to the modiolus near the base while their apical ends are more slanted toward the modiolus near the apex [107]. These differences would possibly result in differences in OHC forces. Therefore, it is reasonable to postulate that these differences in OHCs at different cochlear locations will contribute to the differences in BM's vibrations along the cochlea, such as magitude, tuning, and cut-off slope. The present model did not include these distinct aspects between the base and apex, which will be addressed in its improvement as the next step.

3.5 Summary

OHC motility was discovered more than two decades ago in the mammalian cochlea and has since been considered to be the basis of the cochlear amplifier. The exact manner in which OHC motility contribute to characteristic cochlear behavior, or the cochlear amplifier mechanism, however, remains a mystery. The principle idea of our proposed cochlear amplifier mechanism stems from the notion that the cochlear anatomy, especially the microanatomy of the cochlear partition, must somehow serve its functioning. Our observation of tilts of OHCs and phalangeal processes has suggested that this unique arrangement of sensory cells and supporting cells work in concert to transmit OHC motile forces onto the basilar membrane, thus enhancing its motion. This delivery of active forces from one cochlear position to another results in bidirectional coupling between basilar membrane fibers, and thus active bidirectional coupling.

Specifically, in the active bidirectional coupling mechanism, OHCs' motile forces are delivered, through the basal and apical tilt of the OHCs and PhPs, respectively, to up- and downstream BM fibers. ABC also includes the saturation of OHCs forces with BM displacement. Our 2D mathematical cochlear model produces large amplification, sharp tuning, high input-intensity compression near the characteristic place, and two-tone suppression, which are the characteristic cochlear responses, and compares favorably with physiological measurements. Our model analysis shows that ABC results in negative damping, which accumulates energy to produce a large and localized peak. By its dependence on the traveling wave's wavelength, we also demonstrate that the bidirectional tilts function as a spatial filter that selectively amplifies BM motion selectively—only when the wavelength is appropriate (i.e., comparable to tilt distance).

Our model was not built to describe the details of the cochlear micro-mechanics; it is

only inspired by them. Our model captures the major anatomical features of the cochlear partition needed to produce realistic cochlear responses. The model could be further extended to address other issues that have already been brought to attention of cochlear physiologists. For example, OHC's tilt distance is less than that of the PhP, which can be easily incorporated in the model. Further, OHC length increases from the base to the apex, which can be modeled by a varying OHC motility factor. Also, the saturation profile of OHC forces versus BM displacement is asymmetric, whereas the model uses a symmetric profile.

In summary, our mathematical cochlear model based on a novel cochlear amplifier mechanism, ABC, emulates active cochlear behavior. With ABC, the cochlea is able to realize nonlinear amplification by virtue of clever arrangement of its sensory and supporting cells, rather than a complex arrangement of multiple resonant systems. Indeed, our model provides a plausible physical basis, the microanatomy of the cochlear partition, for the hypothesized cochlear amplifier that has not been described in such detail until now.

Chapter 4

The Active Cochlea: Analog VLSI Implementation

In the previous chapter, we elaborated our efforts of exploring the cochlear amplifier mechanism through developing a mathematical cochlear model. We proposed a novel cochlear amplifier mechanism based on the cochlear microarchitecture, namely, active bidirectional coupling (ABC), to account for the active amplification in the cochlea. The resultant nonlinear active cochlear model yields characteristic responses comparable to physiological measurements. In this chapter, we will proceed to morph the cochlear microarchitecture as well as mechanics into a silicon very-large-scale-integration (VLSI) chip.

The chapter is organized as follows. First, we begin with discussing circuit design techniques, specifically continuous-time filter design, as background reference to our cochlear circuit. We shall also discuss the effect of transistor mismatch in analog CMOS (Complementary metal-oxide semiconductor) circuits. Second, we synthesize a second-order section that models the dynamics and properties of the basilar membrane (BM) in the cochlea

and the interactions between the BM and the cochlear fluids. Third, we show the log-domain (current mode) implementation of our Class AB design. In addition, we describe circuit design that emulates the cochlear fluid and circuitry that realizes the cochlear amplifier mechanism, ABC. Last, we present the architecture of our silicon cochlea.

4.1 Analog VLSI Approach

We employ analog VLSI circuit technique for developing microelectronic chips to mimic the nervous system's functions—these microchips are known as "neuromorphic systems". Toward the goal of modeling the brain functions, this approach offers several advantages over software simulation and/or digital hardware modeling. First of all, hardware implementation runs in real time while computer software simulation usually requires tremendous amount of computation time and large memory space.

Second, analog MOSFET (metal-oxide-semiconductor field-effect transistor) transistor-based circuits, rather than digital implementation, perform continuous-time computation in which continuously varying electrical signals, voltages and/or currents, represent analog properties of the biological system. This analog computation is especially suitable and beneficial for the task of modeling the sensory periphery of the nervous system because input to the sensory models is usually real-world analog signals—light or sound, for example—so that the need for analog-to-digital converters is eliminated.

Finally, operating transistors in subthreshold region leads to compact and low-power designs which are desirable in both engineering and clinical applications. Two major factors lead to the features of small size and low power consumptions. On one hand, simple exponential relationship between drain current and gate voltage of a MOS transistor work-

ing in weak inversion usually gives rise to simple designs, meaning smaller chip area. On the other hand, low current level results in lower power consumption than their digital counterparts. Specifically, we use current-mode low-pass filter (LPF) as the building block of the cochlear chip design.

In this section, we shall first discuss the log-domain filter design technique that we employed in our cochlear chip, then we will touch on an important issue that is closely associated with subthreshold analog circuit design—effect of noise and variation of parameters on circuit and system performance.

4.1.1 Filter Design Techniques

Electronic filters are circuits that perform signal processing for specific purposes. From the perspective of frequency-component processing of signals, there are five basic filter types:low-pass, high-pass, bandpass, all pass and notch filters. Based on the way signals are processed, filters fall into three different categories: Continuous-time filters process analog signals in real time, and fully-digital filters perform filtering operation on digital representation of samples of signals, often not in real time, while sampled data filters operate on samples themselves [108]. Digital filters can be reliable and insensitive to noise, but require analog-digital converter and digital-analog converter when dealing with analog signals or when interfacing with real world; they also consume high power due to fast switching. Switched capacitor filters and switched current filters are the two best known sampled data filters; they use switches (usually transistor switch) together with capacitors and active devices to provide filter functions [108]. Sampled-data filters need sampling and switching, which may have problems in signal settling, clock feedthrough, and charge injection [109]. In our circuit design, we used continuous-time filter design because it meets

the requirement for low power and moderate dynamic range [110]. In other words, it serves our goal to design a cochlear chip whose performance and efficiency are comparable to its biological counterpart.

Aside from passive continuous time filters (classic RLC filter as an example) which are still much in use but are unsuitable for implementation in the ubiquitous integrated circuit [108], active continuous time filters have been extensively explored, in which active-RC and active-C filter form major conventional continuous time filters. Opamp-RC is the major form of active-RC filters that use opamp as active elements. Operational transconductance amplifier-C (OTA-C, or gm-C) filters use only active element, OTA, and capacitors, making them suitable for integration [108]. Two most popular forms of active-C filters are MOS-C and OTA-C filters [109].

Most of the existing silicon cochlea employed gm-C filter design [6], [82], [111]. A gm-C filter is suited for high-speed application due to the fact that it is configured in open loop such that there is no stability constraint. Its major drawback is that with an OTA used in open loop, it has a very small input level range, about 60 mV, to keep it relatively linear [81].

Among all active filter design approaches are only a few of the circuit topologies well suited to VLSI implementations, one of which, the state-variable filter is the most general in form and most widely used in VLSI continuous-time filters [110]. The key advantage of state-variable filters is that they require only two basic building blocks: integrators and weighted summers [110]. By decoupling the poles of the system, a N-th order biquadratic (biquad) filter structure is generally realized as a cascade of second-order circuits, followed by a first-order circuit, if N is odd. The biquad approach is widely used for its simplicity, ease of design, and ease of debugging.

Log-domain Filters

As a novel form of current-mode active continuous-time filter, Log-domain filters have been recently proposed and developed and have demonstrated the potential to accomplish both high-frequency and low distortion levels [112]. A Log-domain filter directly utilizes the inherent exponential I-V relationship of a bipolar transistor or a MOSFET transistor operated in subthreshold. It realizes a linear filter from outside although the internal filtering done in Log-domain is nonlinear. Log-domain filters using MOS transistors has become increasingly attractive in current-mode design due to its zero gate-leakage current and low power consumption. As there is no need to include linearization in a Log-domain filter, unlike in a gm-C filter, the topology is usually quite simple, resulting in fast operation.

The Log-domain technique shares certain similarities with the classical translinear principle, and can be viewed as a dynamic extension to this principle [109]. Logarithmic compression in log-domain followed by exponential expansion is referred to as companding (compress-expand) technique. Log-domain filters achieve the advantageous potential of companding signal processing, which mainly includes larger dynamic range than that of a linear signal processing circuit. The compression raises weak signals further above the noise floor while shrinking strong ones away from the distortion-prone level; the expansion restores the signal's original dynamic range by attenuating the weak signals and amplifying the large signals [109].

Current versus Voltage Mode

Traditional voltage-mode circuits have faced difficulties in meeting high-speed, highly linear operation towards low-power and low-voltage designs [113]. Current-mode circuits excel in their high-speed response, generally low power supply requirements, and low sen-

sitivity to various parasitics. Design of current-mode filters requires current-mode building blocks, rather than voltage-mode ones. Recent advances in analog integrated circuits and signal processing have shown that the current-mode approach is superior to the voltage-mode in terms of its wide bandwidth, high speed, low voltage and power, large dynamic range, and simplicity in circuit structure [108]. Current-mode operation offers large dynamic range if the nonlinear device transconductance is compensated for in the filter design, such that the operation remains linear outside the small-signal region [1] [4].

Class AB versus A Operation

Classification principle in analog electronic amplifiers has also been introduced in classifying analog filter designs. Among Class A, B, AB and C, Class A and AB are the two mostly often encountered circumstances. In a Class A filter design, the input signal drives the output signal throughout the entire input wave cycle, while in a Class B design, only half cycle of the input drives the output. The "off" status of the device in Class B design yield high power efficiency; however, it suffers from a drawback that there is some distortion caused by switching between "on " and "off" status—called crossover distortion. Employment of a complementary pair or "push-pull" arrangement of Class B design, but with a slight "on" bias (a little above zero) for the device when it is not in use, results in Class AB design.

Compared to Class A operation, Class AB implementation offers the advantages of increased dynamic range, reduced effect of transistor mismatch, and lowered power consumption. This is mainly due to the fact that a Class AB design only maintains a relatively low baseline level (current/voltage), thus suppressing this major source of variation and additional power consumption.

[1] For small time-varying signals carried over a constant bias, a nonlinear device or system can be considered as linear as an approximation.

The Class AB design not only inherits the power efficiency of Class B design, but also gets rid of the crossover distortion problem by means of the non-zero baseline. In a Class AB design, there are two differential signal paths in which signals are always kept positive relative to the low baseline signal. The final full-wave output of a Class AB design can be obtained through combining the output signals in the two filtering paths. A common-mode constraint is required to determine the differential output signals together with the differential mode. This configuration eliminates the need for a large baseline (a DC current in current-mode design), thus also decreasing power consumption and moderating the effect of transistor mismatch introduced by matching of the baseline which is a requirement in a Class A design.

According to the noise behavior analysis for Log-domain filters in both class A and class AB operation, the dynamic range of class AB companding circuits can be substantially extended compared to that obtained with class A circuits without increasing the maximum signal-to-noise ratio and therefore without increasing the power consumption [114]. However, the requirement of an additional class AB conditioner for the input signal (e.g., on-off circuit [4] or a current splitter) might result in a higher noise floor, which, in turn, will somewhat reduce the extension of the dynamics range. Despite the drawback, Class AB design is favorably chosen in our cochlear chip design because it meets our goal of reduced variations between circuit components as well as the low power consumption.

4.1.2 Mismatch in CMOS Circuits

Device variations can be categorized into systematic and random [115]. Differential circuit topology and proper biasing techniques can make the integrated circuits performance largely insensitive to these systematic variations. Device to device variation is refereed

to as device mismatch, which is random. In subthreshold operation, variation in threshold voltage is the major source of channel current difference for a matched transistor pair. It has a normal distribution with zero mean and a variance dependent on the device area (channel width W times channel length L) [115]. This simply suggests that increasing transistor size will decrease the extent in threshold voltage matching, thus improving device matching and circuit performance.

Several approaches can be taken to reduce the effect of transistor mismatch. First, proper layout technique can be employed, such as symmetry and common centroid technique, to obtain better matching between transistors that are supposed to match. Second, transistor size can be increased such that area variation becomes smaller. However, this size increase is always related to increase in parasitic capacitances, and the extent of area increase is also limited by the fabrication cost. When taking the approach of increasing transistor size in our design, we first investigated though SPICE (simulation program with integrated circuit emphasis) [2] simulation of transistor-level circuits to find the transistors whose size change leads to most significant change in output signals, and then we only increase the size of transistors that fall into this category, rather than using large-area transistors everywhere blindly, in order to achieve cost-effective design.

Imperfection in circuit performance can also be caused by the Early effect [3] of MOS transistors. This occurs mostly with current mirrors, the most frequently used circuit primitive. In order to achieve better matching between the original current and the copied one in a current mirror, an implementation improvement can be made by connecting one transistor

[2] SPICE is a general purpose analog circuit simulator. It is a powerful program that is used in integrated circuit and board level design to check the integrity of circuit designs and to predict circuit behavior.

[3] Early effect, also the channel length modulation effect, describes the phenomenon that the drain current increases slightly with drain voltage for a saturated MOSFET. Early voltage is defined to be the drain-to-source voltage (negative) at which the drain current is zero. In an ideal MOSFET, the Early voltage would be infinite.

in series on both sides of the mirror and using diode connection on the source-current side. This results in a “complex current mirror”. The insertion of these two additional transistors brings the source-to-drain voltage closer between both sides, thus reducing the effect of Early voltage. Our SPICE simulations show that if a complex mirror accompanied by increasing the channel area of the transistors that are connected to power supply rails would make the gain of the mirror closer to 1 while decreasing the standard deviation of the gain distribution to a large extent.

Class AB design could suffer from mismatch between the differential paths introduced by device mismatch. An ideal differential-mode circuit does not respond to common-mode signal (i.e., a signal that is present on both paths) and only responds to differential signals. That is, an ideal Class AB design has zero common-mode gain and large differential-mode gain. The ratio between the differential-mode signal gain and the common-mode gain, called common-mode rejection ratio (CMRR), should be equal to infinity in the ideal case. However, existence of device mismatch will cause the CMRR to decrease as it increases the common-mode gain. To address this problem, proper and careful layout technique should be employed to reduce the effect of mismatch between the two differential paths to make the CMRR as large as possible.

4.2 Cochlear Circuit Synthesis

We shall synthesize the cochlear circuit in this section which will be the circuit analog of our mathematical cochlear model, thereby the biological cochlea. We synthesize a circuit model of a 2D active cochlea, which comprises the cochlear fluid design, the basilar membrane (BM) design, and implementation of our hypothesized cochlear amplifier

mechanism—active bidirectional coupling (ABC). We first start by synthesizing a passive cochlea, which mainly includes the design of the BM boundary condition. The synthesis result was a second-order section that is formed by two first-order LPFs, and the interaction between the input and output signals of the BM. We then synthesize the BM boundary condition in the active case by adding ABC, achieving an active cochlear circuit model.

4.2.1 Cochlear Fluid Design

VLSI implementation of a passive cochlear model consists of two circuit elements: the cochlear fluid and the BM. In this section, we present the design of a cochlear fluid element; connecting a number of such elements will form the fluid network that emulates the cochlear fluid body. In other words, we will implement a discrete fluid network, at a large scale (i.e., small discretization step), as the approximate analogy of the continuous cochlear fluid.

Modeling the two dimensions of the cochlear fluid chamber offers advantages over a one-dimensional model in which the height of the fluid chamber is not considered. A 2D fluid model allows for fluid motion in the vertical direction, and is thus capable of capturing more biologically compatible responses. Our mathematical modeling investigation on the choice of a 1D or 2D model also revealed that a 2D model generates more realistic cochlear behavior than a 1D model, in terms of the amplitude and the phase of the BM vibration. Therefore, we implemented a 2D cochlea model in analog VLSI, also taking advantage of the 2D planar nature of a silicon die.

The first silicon cochlea to implement a 2D cochlear fluid was constructed by Watts [6]. Following Watts's approach, we treat the cochlear fluid as a resistive sheet [6]. Our

implementation is different from his though as we employ current-mode design, rather than voltage mode.

In current mode, we achieve a simpler implementation of the fluid element, described as follows. In discrete form, the fluids can be viewed as a grid of elements with certain resistance that corresponds to the fluid density or mass. As we know from Chapter 3, the fluid velocity potential, ϕ, satisfies the Laplace's equation assuming the incompressibility of the inviscid fluids. Since electrical charge is conserved for a small resistance sheet while flux is conserved for a small fluid volume, current variables shall be used to represent the velocity of the fluid, and also of the BM.

Following the approach in [116], we implement the cochlear fluid network using a diffusor network formed by a 2D grid of nMOS transistors. A MOS transistor in subthreshold ohmic region acts as a diffusive element as the source-to-drain current flowing through the channel is caused by the diffusion of charge carriers. Thus, such a MOS transistor is called a diffusor and a network formed by diffusors is called a diffusive network.

We now show in detail the operation of a diffusor. We rewrite the drain current, $I_{\rm ds}$, of a nMOS transistor as follows (voltages are in the unit of $\mathrm{u_T} = kT/q$, where k is the Boltzmann constant, T is the absolute temperature (in Kelvins), and q the magnitude of the electrical charge (in coulombs) on the electron. At room temperature ($T = 300$K), the value of $\mathrm{u_T}$ is approximately 26 mV):

$$\begin{aligned} I_{\rm ds} &= I_0 e^{\kappa V_{\rm g}} (e^{-V_{\rm s}} - e^{-V_{\rm d}}) \\ &= D(Q_{\rm s} - Q_{\rm d}), \end{aligned} \tag{4.1}$$

where $V_{\rm g}$, $V_{\rm s}$, and $V_{\rm d}$ are the gate, source, and drain voltages, respectively, and I_0 is the

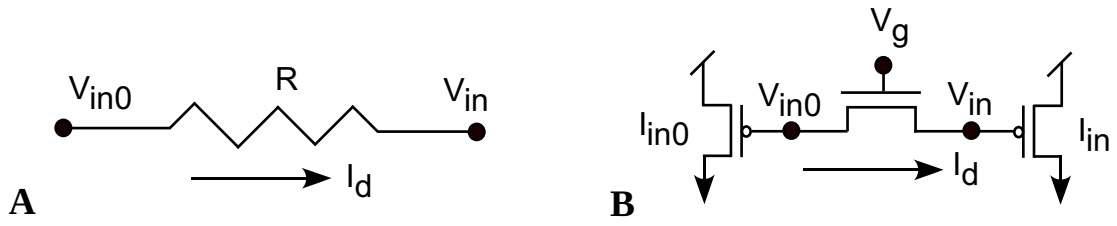

Figure 4.1: Fluid Diffusive Element Design

Analogy between resistive element and its nMOS implementation. **A** A resistor with its two terminal voltages denoted by $V_{\rm in0}$ and $V_{\rm in}$. **B** An nMOS transistor acts as a diffusor with its gate voltage denoted by $V_{\rm g}$. The drain and source voltage of the nMOS is also $V_{\rm in0}$ and $V_{\rm in}$, respectively, and the reciprocals of their exponentials are lineally related to the currents $I_{\rm in0}$ and $I_{\rm in}$, respectively. An analogy can be drew between the resistance of a resistor and the gate voltage of a MOS transistor. In other words, the resistance can be simulated by the diffusive coefficient of a MOS transistor working in subthreshold ohmic regime.

leakage current at zero gate voltage. $D = e^{\kappa V_{\rm g}}$ denotes diffusion strength of charge carriers (electrons in the case of nMOS transistors) while $Q_{\rm s} = I_0 e^{-V_{\rm s}}$ and $Q_{\rm d} = I_0 e^{-V_{\rm d}}$ represent their concentrations at the source and the drain, respectively.

We derived the relation between the resistance of a resistor and the diffusive coefficient of a MOS transistor by drawing an analogy between a resistor and a nMOS transistor in subthreshold ohmic regime (Figure 4.1). For the resistor R (in Figure 4.1A), the current $I_{\rm d}$ was calculated as

$$I_{\rm d} = \frac{V_{\rm in0} - V_{\rm in}}{R}. \tag{4.2}$$

For the pMOS transistor that is gated by $V_{\rm in0}$ (in Figure 4.1B) with assumed small drain voltage ($4{\rm u_T}$ smaller than $V_{\rm dd}$), its drain current $I_{\rm in0}$ can be described as $I_0 e^{-\kappa V_{\rm in0}} e^{V_{\rm dd}}$; similarly, $I_{\rm in}$ is equal to $I_0 e^{-\kappa V_{\rm in}} e^{V_{\rm dd}}$. By assuming $\kappa \approx 1$, we obtain the following as an

approximation:

$$\begin{aligned} I_{\text{in0}} &= I_0 e^{-V_{\text{in0}}} e^{V_{\text{dd}}}, \\ I_{\text{in}} &= I_0 e^{-V_{\text{in}}} e^{V_{\text{dd}}}. \end{aligned} \tag{4.3}$$

And for the nMOS transistor in Figure 4.1B, according to Equation 4.1, the channel current I_{d} can be represented by $D(Q_{\text{in}} - Q_{\text{in0}})$ where $Q_{\text{in}} = I_0 e^{-V_{\text{in}}}$ and $Q_{\text{in0}} = I_0 e^{-V_{\text{in0}}}$. Thus, Equation 4.3 becomes

$$\begin{aligned} I_{\text{in0}} &= Q_{\text{in0}}\, e^{V_{\text{dd}}}, \\ I_{\text{in}} &= Q_{\text{in}}\, e^{V_{\text{dd}}}. \end{aligned} \tag{4.4}$$

Therefore, for the diffusive element in Figure 4.1B, we have

$$\begin{aligned} I_{\text{d}} &= D(Q_{\text{in}} - Q_{\text{in0}}) \\ &= D e^{-V_{\text{dd}}}(I_{\text{in}} - I_{\text{in0}}) \\ &= \frac{I_{\text{in}} - I_{\text{in0}}}{e^{V_{\text{dd}}}/D} \end{aligned} \tag{4.5}$$

By comparing Equation 4.5 with Equation 4.2, we obtained the expression as follows that describes the relation between the magitude of the fluid-element resistance and the circuit variables:

$$R \equiv e^{V_{\text{dd}}}/D \tag{4.6}$$

$$= e^{V_{\text{dd}}} e^{-\kappa V_{\text{g}}} \tag{4.7}$$

Therefore, the resistance due to the fluid density was implemented by controlling the gate

voltage $V_{\rm g}$ of an nMOS transistor thus its difference from the power supply $V_{\rm dd}$. Increasing $V_{\rm g}$ thus decreasing the difference results in larger channel current, thus corresponding to smaller resistance, and vice versa.

4.2.2 Synthesis and Analysis of a Single BM Stage

We shall now synthesize the circuit design for realizing the BM boundary condition in the log domain (current mode). This BM circuit will interact with the diffusor fluid network that we have discussed in the previous section.

For reference, we repeated the boundary condition of the BM in the passive case as

$$2\rho\dot{\phi} = S(x)\delta(x) + \beta(x)\dot{\delta}(x) + M(x)\ddot{\delta}(x), \quad \text{at } y = h, \tag{4.8}$$

where $M(x)$ is the mass, $S(x)$ is the stiffness, and $\beta(x) = \zeta\sqrt{S(x)M(x)}$ is the damping per unit area of the BM, and ζ is the damping ratio; δ is the downward displacement of the BM while the first time-derivative of δ is its velocity and the second is its acceleration. $\phi(x)$ is the velocity potential at the BM boundary where $y = 0$, ρ is the fluid density, and the factor of 2 accounts for fluid mass in both top and bottom cochlear ducts. For this second-order system, the input is the fluid velocity potential, ϕ, which is the driving force, and the output is the BM velocity, $\dot{\delta}$.

The design goal for the passive case is to determine a relation between the input and the output in terms of circuit variables (electrical signals: current in our current-mode design) that implements the BM boundary condition as shown in Equation 4.8. Once we obtain the BM circuit design equation, we shall employ a number of BM circuits to model a number of BM transverse fibers, and make the BM circuits interact with the fluid diffusive network,

mimicking the biological cochlea.

We employed current to model the velocity as in our fluid element design. We used the current flowing through the BM impedance, I_{mem}, to represent the BM velocity $\dot{\delta}$ in the vertical direction. Thus, the BM displacement δ is represented by the integral of the current I_{mem} while the BM acceleration $\ddot{\delta}$ is represented by the first time-derivative of I_{mem}. We also use the quantity I_{in} to represent the velocity potential $\rho\phi$.

Substituting I_{mem} and I_{in} in Equation 4.8 yields

$$\dot{I_{\mathrm{in}}} = S(x) \int I_{\mathrm{mem}} + \beta(x) I_{\mathrm{mem}} + M(x) \dot{I_{\mathrm{mem}}}. \tag{4.9}$$

Taking the time derivative of Equation 4.9 in order to remove the integration operation, we obtain

$$\ddot{I_{\mathrm{in}}} = S(x) I_{\mathrm{mem}} + \beta(x) \dot{I_{\mathrm{mem}}} + M(x) \ddot{I}_{\mathrm{mem}}. \tag{4.10}$$

This equation thus becomes the target of our circuit synthesis. Synthesis of the above equation means decomposing the second-order section into two first-order sections and possible another equation that describes the relation between the input, the output, and intermediate variables.

We tackled the synthesis task for the passive case starting with rewriting the design target equation. Since the passive model is a linear system, we transformed the design equations in the time domain to the frequency domain to get rid of time-derivative expressions. Using $s = j\omega$, Equation 4.10 becomes

$$I_{\mathrm{in}} s^2 = S(x) I_{\mathrm{mem}} + \beta(x) I_{\mathrm{mem}} s + M(x) I_{\mathrm{mem}} s^2, \tag{4.11}$$

which is a new version of our target design equation.

Our synthesis process was a variation of the state-space synthesis approach proposed by Frey [112]. The general procedures of the approach are firstly to determine a state-space representation of the system, secondly to explore the equilibrium condition and obtain a transformation that yields appropriate operating condition, and finally to derive a set of nodal equations for capacitors, which suggests an interconnection of transistors, thus the transistor-level implementation of the design.

We developed a Mathematic code to facilitate the synthesis process, which mainly involves determining the coefficients of the state variables, input, and output current signals. The choice of coefficients is based on whether the chosen set of coefficients could lead to realization of the target design equation and which realization is the most economical solution, meaning the simplest implementation and smallest chip area among other possible options.

We found that a few solutions to the synthesis equations were possible. For example, the two first-order sections could be chosen to be both integrators, both LPFs, or one integrator and one LPF. Adding gain factors for the state variables as well as input (I_{in}) and the output (I_{mem}) introduces additional flexibility. We need to determine what choice yields the best functionality, flexibility, and implementation cost.

We shall describe both the synthesis result involving two integrators and the result with two LPFs. Through analyzing both cases, we shall explain why we reached our decision, based on considerations of DC operating point and stability.

Implementing the second-order system of the BM requires two state-space variables, which were represented by currents I_{s} and I_{o}. Synthesis result of a second-order system

that consists of two integrators is described as follows, with $s = j\omega$.

$$\begin{aligned} \tau_1 I_{\rm s} s &= I_{\rm mem} \\ \tau_2 I_{\rm o} s &= I_{\rm mem} + I_{\rm s} \\ I_{\rm mem} &= I_{\rm in} - I_{\rm o} \end{aligned} \tag{4.12}$$

Gain factors can be easily added to the results above thus adding more flexibility to the design. We shall describe two of the possible variations as follows. We added gain factors a and b at different positions, which result in

$$\begin{aligned} \tau_1 I_{\rm s} s &= I_{\rm mem} \\ \tau_2 I_{\rm o} s &= I_{\rm mem} + bI_{\rm s} \\ I_{\rm mem} &= a(I_{\rm in} - I_{\rm o}) \end{aligned} \tag{4.13}$$

and

$$\begin{aligned} \tau_1 I_{\rm s} s &= I_{\rm mem} \\ \tau_2 I_{\rm o} s &= I_{\rm mem} + bI_{\rm s} \\ I_{\rm mem} &= I_{\rm in} - aI_{\rm o}, \end{aligned} \tag{4.14}$$

For the design described in Equation 4.12, Equation 4.13, and Equation 4.14, their DC operating point were found as follows.

$$I_{\rm mem} = 0, \quad I_{\rm s} = 0, \ \text{and} \ I_{\rm o} = I_{\rm in}. \tag{4.15}$$

We also synthesized this second-order system using two interacting LPFs, and the design equations are described as:

$$\begin{aligned} \tau_1 I_{\mathrm{s}} s + I_{\mathrm{s}} &= -I_{\mathrm{in}} + I_{\mathrm{o}}, \\ \tau_2 I_{\mathrm{o}} s + I_{\mathrm{o}} &= I_{\mathrm{in}} - b I_{\mathrm{s}}, \\ I_{\mathrm{mem}} &= I_{\mathrm{in}} + I_{\mathrm{s}} - I_{\mathrm{o}}, \end{aligned} \tag{4.16}$$

The two first-order systems are both LPFs, with time constants τ_1 and τ_2, respectively; b in the second LPF is a gain factor, which is necessary for realizing reasonable BM stiffness given practical choice of τ_1, τ_2 and capacitance (capacitor size is limited by silicon area).

This design realizes the passive cochlea model, as was described by Equation 4.11. This design uses a loop of two LPFs connected with negative feedback to realize the poles. The zeros of the second-order system are achieved by creating an output signal, I_{mem}, that is the weighted summation of the two LPFs' outputs, I_{s}, and I_{o}, as well as the input signal, I_{in}. The design's DC operating point, shown below, was somewhat different from that of the integrator-based design we just described above.

$$I_{\mathrm{mem}} = I_{\mathrm{s}}, \quad I_{\mathrm{s}} = \frac{1}{b} I_{\mathrm{in}}, \ \text{and} \ I_{\mathrm{o}} = I_{\mathrm{in}}. \tag{4.17}$$

4.2.3 Analysis of the Design

We performed some analysis on both the integrator-based design and the LPF-based design that we presented in the previous section. This analysis associates the circuit variables and their expressions with physiological parameters in the biological cochlea. We also obtained the transfer functions of a single BM section, when stages are combined to form a

1D network (single cochlear stage with loading), and when stages are combined and ABC is included. Analysis and result comparison revealed that the output of a combined BM-fluid network cannot be simply derived from single-stage responses due to the effect of network loading. We will also present the effect of ABC on the transfer functions.

Circuit Parameters vs. Physical Properties

Given Equation 4.16 in the LPF-based design, $I_{\rm in}$, $I_{\rm s}$, and $I_{\rm o}$ can be expressed in terms of the output current $I_{\rm mem}$ as follows.

$$\begin{aligned} I_{\rm in} &= \frac{(b+1)+(\tau_1+\tau_2)s+(\tau_1\tau_2)s^2}{\tau_1\tau_2 s^2} I_{\rm mem}, \\ I_{\rm s} &= -\frac{1}{\tau_1 s} I_{\rm mem}, \\ I_{\rm o} &= \frac{(b+1)+\tau_1 s}{\tau_1\tau_2 s^2} I_{\rm mem}. \end{aligned} \tag{4.18}$$

By comparing the expression of $I_{\rm in}$ with the design target Equation 4.8, we obtain the circuit counterparts of the BM 's stiffness $S(x)$, damping $\beta(x)$, and mass $M(x)$:

$$S(x) = \frac{b+1}{\tau_1\tau_2}, \qquad \beta(x) = \frac{\tau_1+\tau_2}{\tau_1\tau_2}, \qquad M(x) = 1. \tag{4.19}$$

As we can see, three circuit parameters, b, τ_1, and τ_2, were used to model the BM's physical properties. This configuration was the same as in the mathematical model simulation, in which the BM mass was a constant. Based on these relations, it is required that τ_1 and τ_2 increase exponentially from the stapes along the cochlea in order to simulate the exponentially decreasing BM stiffness and damping.

Furthermore, we can derive the quality factor of the second order section based on the

above relationships.

$$\begin{aligned} Q &= \frac{\sqrt{S(x)M(x)}}{\beta(x)} \\ &= \sqrt{\frac{b+1}{\tau_1\tau_2}}\frac{\tau_1\tau_2}{\tau_1+\tau_2} \\ &= \frac{\sqrt{b+1}}{\sqrt{\tau_1/\tau_2}+\sqrt{\tau_2/\tau_1}}. \end{aligned} \tag{4.20}$$

Therefore, Q was electrically tunable and it varied from stage to stage as τ_1 and τ_2 varied exponentially along the cochlear position. If $\tau_1 = \tau_2$, Equation 4.21 reduced to:

$$Q = \frac{\sqrt{b+1}}{2}, \tag{4.21}$$

which implements a constant-Q along the cochlea if the gain factor b is implemented as a constant.

Similarly, the integrator-based design (Equation 4.12) yields the relationship between I_{in} and I_{mem} as follows.

$$I_{\text{in}} = \frac{1+\tau_1 s+\tau_1\tau_2 s^2}{\tau_1\tau_2 s^2} I_{\text{mem}}, \tag{4.22}$$

based on which, we obtain the circuit analogs as follows,

$$S = \frac{1}{\tau_1\tau_2}, \quad \beta = \frac{1}{\tau_2}, \text{ and } M = 1 \tag{4.23}$$

and the quality factor as follows,

$$Q = \sqrt{\frac{\tau_2}{\tau_1}}. \tag{4.24}$$

Its two variations have the following circuit analogs, respectively:

$$S = \frac{ab}{\tau_1\tau_2}, \quad \beta = \frac{a}{\tau_2}, \text{ and } M = 1 \tag{4.25}$$

and

$$S = \frac{b}{\tau_1 \tau_2}, \quad \beta = \frac{1}{\tau_2}, \text{ and } M = \frac{1}{a} \tag{4.26}$$

And the quality factors are the same,

$$Q = \sqrt{\frac{b\tau_2}{a\tau_1}}. \tag{4.27}$$

For the BM design, we chose the design with two low-pass filters (LPFs), rather than two integrators or one LPF and one integrator (synthesis results not shown). The main reason was that through circuit simulations, we found that the response stability of a second-order system with internal interaction between its two first-order systems was less sensitive to parameters (e.g., time constants, input amplitude, etc.) when the two comprising first-order systems were both LPFs instead of integrators. In addition, in terms of realizing a relatively large quality factor, an LPF-based design does not require the two time constants, τ_1 and τ_2, to have a large ratio to achieve certain large quality factor, as required in the integrator-based design.

Transfer Functions

Investigating the characteristics of a single BM stage, especially when it is embedded in the network that a cochlear circuit requires, was instructive for understanding the response of the whole 2D cochlea. We calculated the transfer function of a BM-fluid stage, in an isolated condition and in the context of a network (with interaction between previous and following BM sections and fluid diffusive elements), and compared them in order to develop insight into the effect of network loading on a BM section.

In a single BM-fluid stage, the BM was viewed as a finite impedance, z_{m}, to the driving

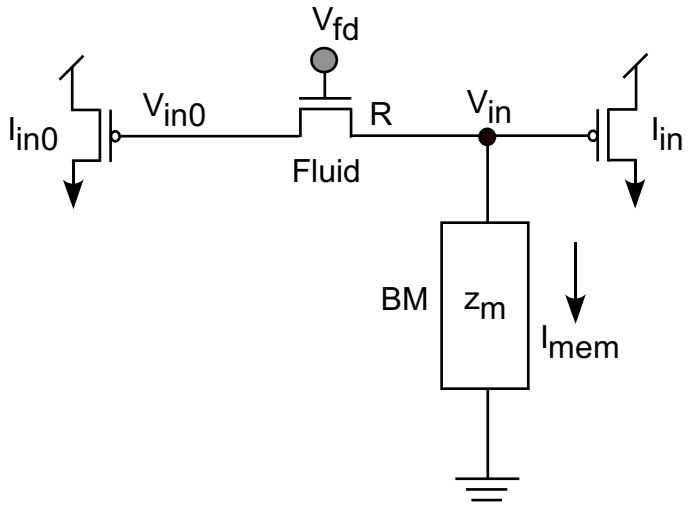

Figure 4.2: Conceptual Electrical Model of a Single Basilar Membrane-Fluid Stage

A single basilar membrane (BM)-fluid stage includes a fluid diffusive element realized by an nMOS transistor, and an impedance z_{m}, representing the BM circuit. I_{in0} and I_{in} represent the velocity potential at the two terminals of the fluid element while the corresponding voltages, V_{in0} and V_{in}, represent the logarithm of the velocity potentials, respectively. The fluid diffusive element, an nMOS transistor, is gated by the voltage V_{fd}, which determines the resistance given a supply voltage. The current flowing through the BM impedance is denoted by I_{mem}, emulating the BM's velocity in the vertical direction.

force of the fluid (Figure 4.2). $I_{\rm in0}$ and $I_{\rm in}$ represent the velocity potential of the two fluid terminals. The impedance $z_{\rm m}$ can be calculated as follows, based on the BM design we have described in the previous section.

$$\begin{aligned} z_{\rm m} &= \frac{I_{\rm in}}{I_{\rm mem}} \\ &= \frac{(b+1)+(\tau_1+\tau_2)s+(\tau_1\tau_2)s^2}{\tau_1\tau_2 s^2}. \end{aligned} \tag{4.28}$$

In order to gain understanding about the behavior of a single BM subcircuit, we explored two transfer functions, the same approach as in [6] except that we used currents as variables rather than voltages. In addition, the present BM design was different from that work.

One transfer function, $G_{\rm sgl}$ (the subscript "sgl" represents the single isolated stage case), defined as the relation between the resultant current through the BM impedance, $I_{\rm mem}$, and the driving force on the fluid diffusive element, $I_{\rm in0}$, can be expressed as:

$$\begin{aligned} G_{\rm sgl}(s) &= \frac{I_{\rm mem}}{I_{\rm in0}} \\ &= \frac{1}{R+z_{\rm m}} \\ &= \frac{\tau_1\tau_2 s^2}{(b+1)+(\tau_1+\tau_2)s+(R+1)(\tau_1\tau_2)s^2}, \end{aligned} \tag{4.29}$$

where R represented the fluid mass as we discussed in the previous section. The transfer function $G_{\rm sgl}(s)$ had a complex-zero-pair and a complex-pole-pair with the pole-pair corresponding to a peak at certain frequency. At even higher frequencies, $G_{\rm sgl}(s)$ becomes a constant.

Another transfer function $H_{\rm sgl}(s)$, defined as the relation between the currents at the

two terminals of a single fluid diffusive element, $I_{\rm in}$ and $I_{\rm in0}$, is described as:

$$\begin{aligned} H_{\rm sgl}(s) &= \frac{I_{\rm in}}{I_{\rm in0}} \\ &= \frac{z_{\rm m}}{R + z_{\rm m}} \\ &= \frac{(b+1) + (\tau_1 + \tau_2)s + (\tau_1\tau_2)s^2}{(b+1) + (\tau_1 + \tau_2)s + (R+1)(\tau_1\tau_2)s^2} \\ &= \frac{1 + \frac{\tau_1 + \tau_2}{b+1}s + \frac{\tau_1\tau_2}{b+1}s^2}{1 + \frac{\tau_1 + \tau_2}{b+1}s + (1+R)\frac{\tau_1\tau_2}{b+1}s^2} \end{aligned} \tag{4.30}$$

Representing $H_{\rm sgl}(s)$ in terms of functional parameters, τ (time constant), Q (quality factor, a measure of sharpness of frequency responses), and η, yields:

$$H_{\rm sgl}(s) = \frac{1 + \frac{\tau}{Q}s + \tau^2 s^2}{1 + \frac{\tau}{Q}s + (1+\eta)\tau^2 s^2}, \tag{4.31}$$

where $\tau = \sqrt{\tau_1\tau_2/(b+1)}$, $Q = \sqrt{(b+1)\tau_1\tau_2/(\tau_1+\tau_2)}$, and $\eta = R$. Using the same relationships, we rewrote the transfer function $G_{\rm sgl}(s)$ as:

$$G_{\rm sgl}(s) = \frac{\eta\tau^2 s^2}{R(1 + \frac{\tau s}{Qs + \tau^2 s^2(1+\eta)})}. \tag{4.32}$$

The roots of the denominator of $H_{\rm sgl}(s)$ determined its complex-pole pair:

$$s_{p\pm} = \frac{1}{2\tau Q(1+\eta)}[-1 \pm \sqrt{1 - 4Q^2(1+\eta)}]. \tag{4.33}$$

while the roots of the numerator set its complex-zero pair:

$$s_{z\pm} = \frac{1}{2\tau Q}[-1 \pm \sqrt{1 - 4Q^2}]. \tag{4.34}$$

As plotted in [6], the poles and zeros were close to the imaginary axis, which suggested a pronounced peak and a pronounced valley in the magnitude of the transfer function $H_{\mathrm{sgl}}(s)$. Since η is determined by the resistance R, which realization was described in Equation 4.7, we expected that $\eta > 1$. As pointed out in [6], due to the positive value of η, the poles were always closer to the real axis in the complex plane than were the zeros, so the peak in the magnitude of the transfer function always occured at a lower frequency than did the valley.

As we can see from Equation 4.32, for the second-order BM circuit, its amplitude (or gain) and phase responses was determined by the quality factor Q, when η was a constant throughout the cochlea, and τ was chosen for a certain cochlear position. Increasing Q will result in increased response gain.

Single-Stage Transfer Functions in a Loaded Network

Transfer functions of an isolated single BM-fluid section cannot represent its property when it was loaded by a number of other sections in a network [6, 117]. Therefore, it was beneficial to obtain the transfer functions when embedded in the network of BM sections and fluid elements. Toward this end, the straightforward approach was to obtain an closed-form expression of the transfer functions. It is, however, extremely difficult to achieve that goal due to the fact that in a BM-fluid network, BM sections have exponentially increasing time constants along the cochlear position, resulting in a non-uniform network. Therefore, we combined semi-analytical solution and numerical simulation to obtain the frequency response of the two transfer functions, and we checked the effect of loading on the single BM-section function by comparing the transfer functions in the two cases.

We derived the semi-analytical solution to compare a single stage transfer function and the combined-network stage transfer function, based on the single-stage shown in Fig-

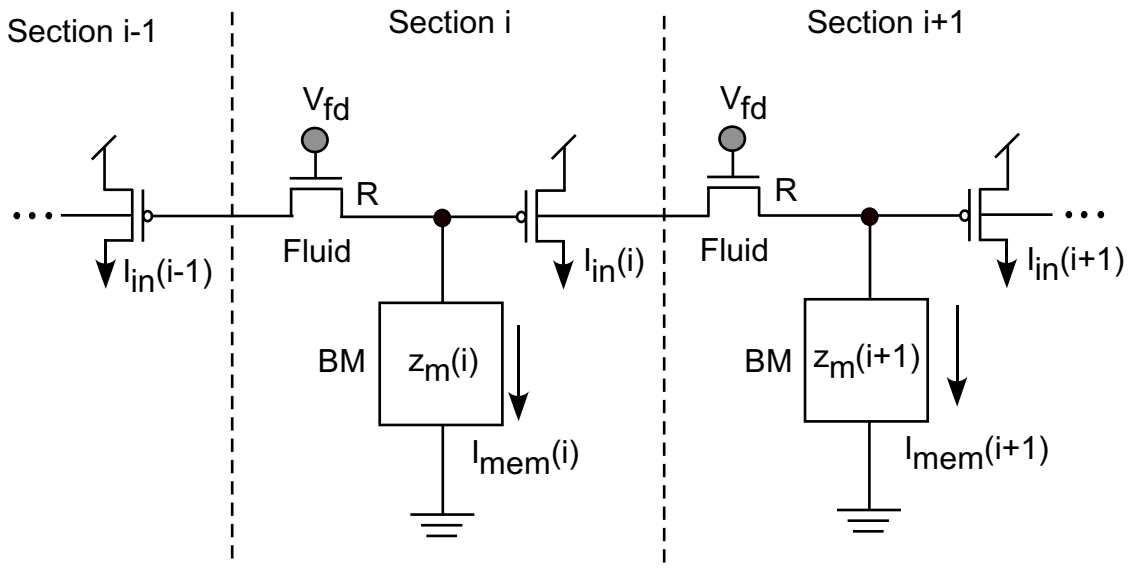

Figure 4.3: Basilar Membrane-Fluid Interaction With Loading

A array of single basilar membrane (BM)-fluid forms a network. Transfer functions are altered by the network loading.

ure 4.2 and the network setup shown in Figure 4.3.

According to the Kirchhoff's Current Law (KCL), we have

$$\begin{aligned} \frac{I_{\rm in}(i-1)-I_{\rm in}(i)}{R} &= I_{\rm mem}(i)+\frac{I_{\rm in}(i)-I_{\rm in}(i+1)}{R} \\ \Longrightarrow \frac{I_{\rm in}(i-1)-I_{\rm in}(i)}{R} &= \frac{I_{\rm in}(i)}{z_{\rm m}(i)}+\frac{I_{\rm in}(i)-I_{\rm in}(i+1)}{R}. \end{aligned} \tag{4.35}$$

This leads to

$$\begin{aligned} H_{\rm load}(i) &= \frac{I_{\rm in}(i)}{I_{\rm in}(i-1)} \\ &= \frac{z_{\rm m}(i)}{R+\left(2-H_{\rm load}(i+1)\right)z_{\rm m}(i)}. \end{aligned} \tag{4.36}$$

where the subscript "load" denotes the loaded case. From Equation 4.36, we see further

that it is difficult to obtain a closed-form solution for the two transfer function because z_{m} (Equation 4.28) changes with cochlear position and it has a complex form. Therefore, Equation 4.36 was solved numerically to obtain solution to $H_{\mathrm{load}}(i)$.

In seeking solutions for transfer functions at each cochlear position, we represented z_{m} and R in terms of biophysical parameters. The BM impedance z_{m} was represented as:

$$z_{\mathrm{m}} = \frac{I_{\mathrm{in}}}{I_{\mathrm{mem}}} = \frac{S(x) + i\omega\beta(x) + (i\omega)^2 m(x)}{(i\omega)^2}, \tag{4.37}$$

where ω is the input signal's angular frequency, and x is the distance from the stapes in the cochlear model. As we can see, aside of its dependence on input frequency, z_{m} varied along the cochlear location x with varying stiffness $S(x)$, damping $\beta(x)$ and mass $m(x)$. In our case, the mass was constant across the cochlea. Also, the resistance of a small amount of fluid was represented as

$$R = 2\rho(\Delta x)^2/H, \tag{4.38}$$

where ρ is the fluid density, H is the cochlear duct height, and Δx is the discretization size along the longitudinal axis. Using Equation 4.37 and Equation 4.38, the transfer functions $H_{\mathrm{sgl}}(s)$ and $G_{\mathrm{sgl}}(s)$ were obtained easily in an isolated case based on the expressions in Equation 4.31 and Equation 4.32.

Finding the transfer functions in the loaded network case was more complex. First it was necessary to solve for the transfer functions at the last position (at the apex) of the discretized cochlea, and then use the solution to solve for the transfer function at the previous section, based on the relation described in Equation 4.36. Repeating the procedure yielded the transfer functions at all cochlear positions. The parameter values used were the same as those listed in Chapter 3.

Comparing the numerical simulation results in the loaded network with the isolated condition revealed the effect of loading to the transfer functions of BM-fluid section. In contrast to the responses of a single BM-fluid stage, the peak was reduced when stages were combined (Figure 4.5A). Furthermore, the amplitude of $H_{\mathrm{load}}(i)$'s frequency response did not exhibit a pronounced peak before the valley in the loaded network (Figure 4.4A). The result indicated that interactions between BM stages through the diffusive elements had a destructive impact on the gain of BM responses. This destructive interference was very likely due to the large phase difference between BM sections, with close-to-π phase difference causing cancelation of response amplitude. This destructive-interference phenomena was evident with responses described in [7].

Adding ABC in the Loaded Network

It was instructive to take the loaded-network simulation further by adding the cochlear amplifier mechanism into the system, and then investigating the effect of the active bidirectional coupling. Meanwhile, this task was formidable if the circuit model in Figure 4.3 was used because the realization of ABC requires using the comprising lower-level variables of the BM circuit to represent the BM impedance z_{m}. Therefore, it was quite difficult to formulate the transfer function as described in Equation 4.36. An equivalent approach we took was to simulate our 1D mathematical model and obtain the value of transfer functions defined by their definition.

When ABC was included in the simulation, the amplitude response of $H_{\mathrm{load}}(s)$ regained a pronounced peak and a relatively large quality factor (Figure 4.6A and Figure 4.7A). This suggested an important notion that the bidirectional coupling between BM sections due to ABC counteracts the destructive interference among BM sections due to their coupling through fluid. Therefore, ABC played a critical role in achieving desirable gain and quality

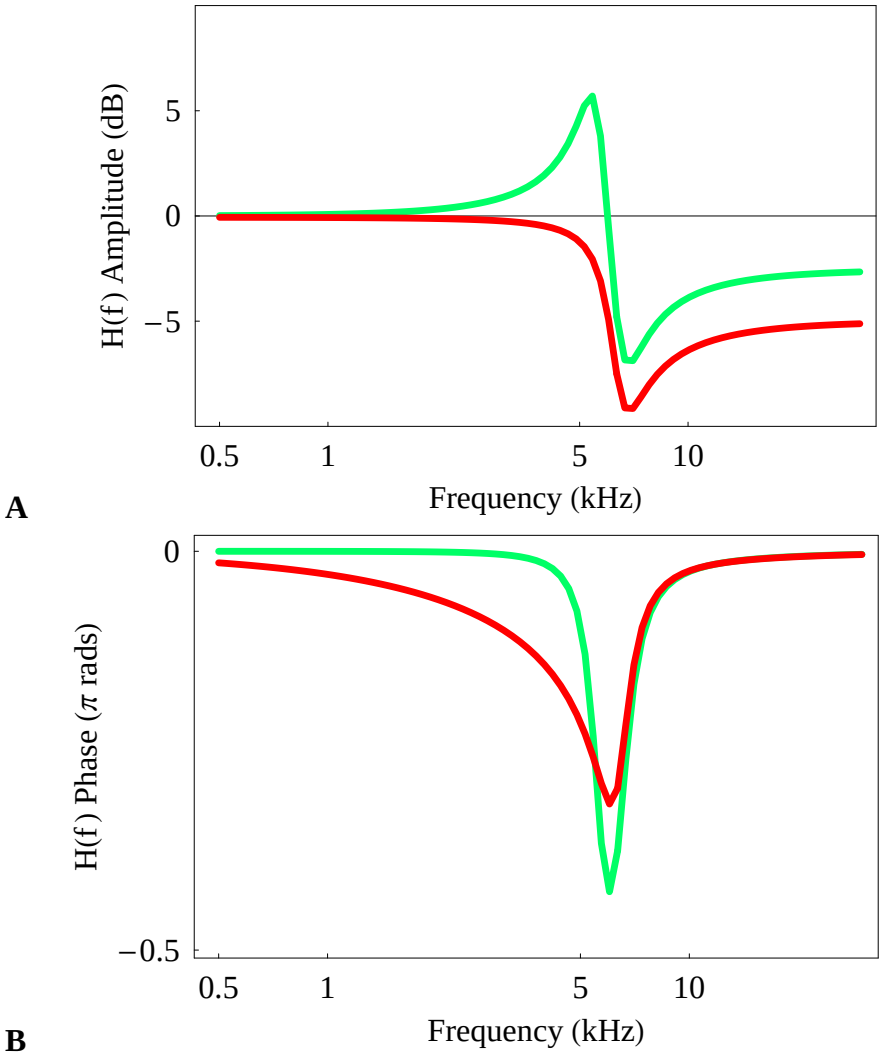

Figure 4.4: Transfer Function $H(f)$ of a Single Basilar Membrane-Fluid Stage and in a Loaded Network

Frequency responses of transfer function $H(f)$ of a single basilar membrane (BM)-fluid stage ($H_{\mathrm{sgl}}(f)$) and in a loaded network ($H_{\mathrm{load}}(f)$). **Top** Amplitude; **Bottom** Phase; **Green** Single BM-fluid stage; **Red** Loaded network.

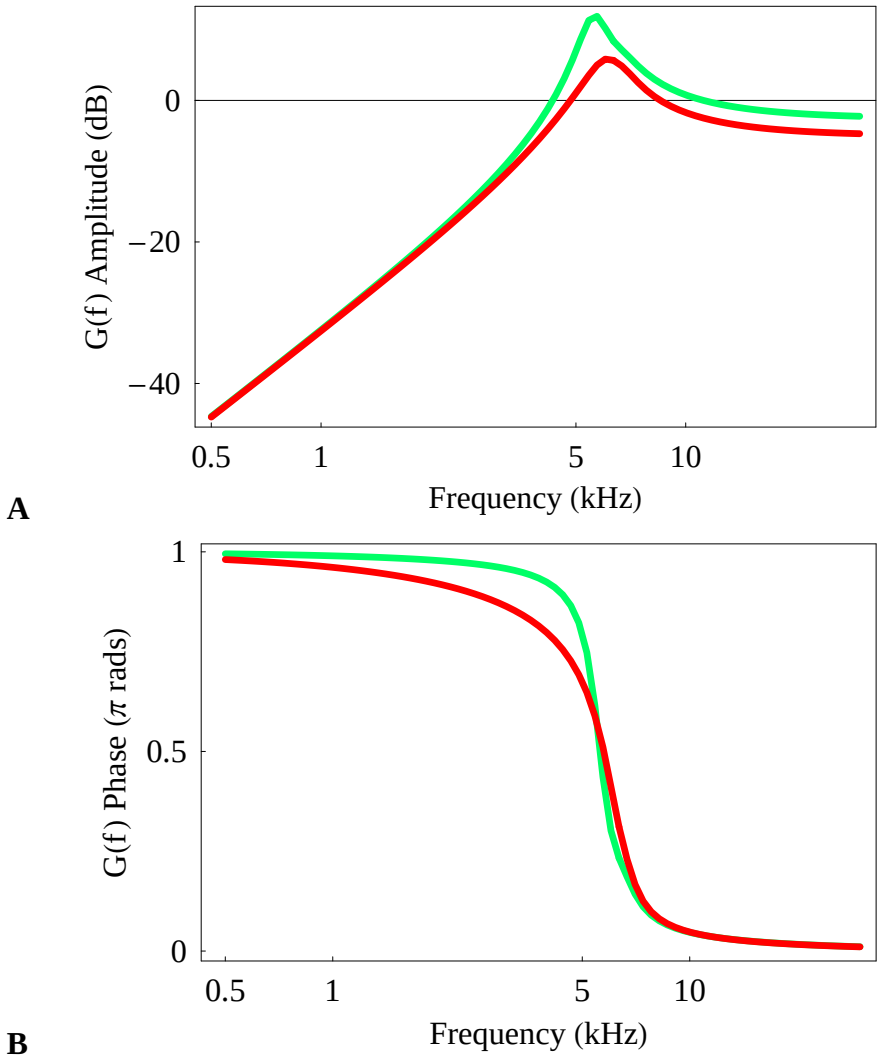

Figure 4.5: Transfer Function $G(f)$ of a Single Basilar Membrane-Fluid Stage and in a Loaded Network

Frequency responses of transfer function $G(f)$ of a single basilar membrane (BM)-fluid stage ($G_{\mathrm{sgl}}(f)$) and in a loaded network ($G_{\mathrm{load}}(f)$). **Top** Amplitude; **Bottom** Phase; **Green** Single BM-fluid stage; **Red** Loaded network.

factor along the cochlea.

4.2.4 Adding Active Bidirectional Coupling

We have described our circuit design for the BM and fluid circuits and we have also investigated the characteristics of a single BM in isolated and loaded conditions. We were also able to compute the transfer functions of the BM-fluid network with added cochlear amplifier mechanism ABC through solving the mathematical circuit equivalent We shall now present the circuit design when including the active bidirectional coupling OHC forces in the cochlea design (i.e., to include the F_{OHC} term).

For reference, we rewrote the BM boundary condition with ABC as follows.

$$\begin{aligned} 2\rho\dot{\phi} &= S(x)\delta(x) + \beta(x)\dot{\delta}(x) + M(x)\ddot{\delta}(x) - F_{\mathrm{OHC}}, \\ F_{\mathrm{OHC}} &= \alpha\gamma S(x)\mathcal{T}\big(\delta(x-d)\big) - \alpha S(x)\mathcal{T}\big(\delta(x+d)\big), \end{aligned} \tag{4.39}$$

where $\mathcal{T}$ denotes saturation, and $\delta(x-d)$ and $\delta(x+d)$ represented the displacement of adjacent upstream and downstream BM segments, respectively. Note that we took the terms $r_{\mathrm{fb}}S(x)$ and $r_{\mathrm{ff}}S(x)$ outside of the saturation operation $\mathcal{T}$ as an approximation and for simplicity.

Let the gain factor $r_{\mathrm{ff}} = \alpha\gamma$ denote the feedforward OHC motility factor and the gain factor $r_{\mathrm{fb}} = \alpha$ denote the feedbackward OHC motility factor. Combining the two equations

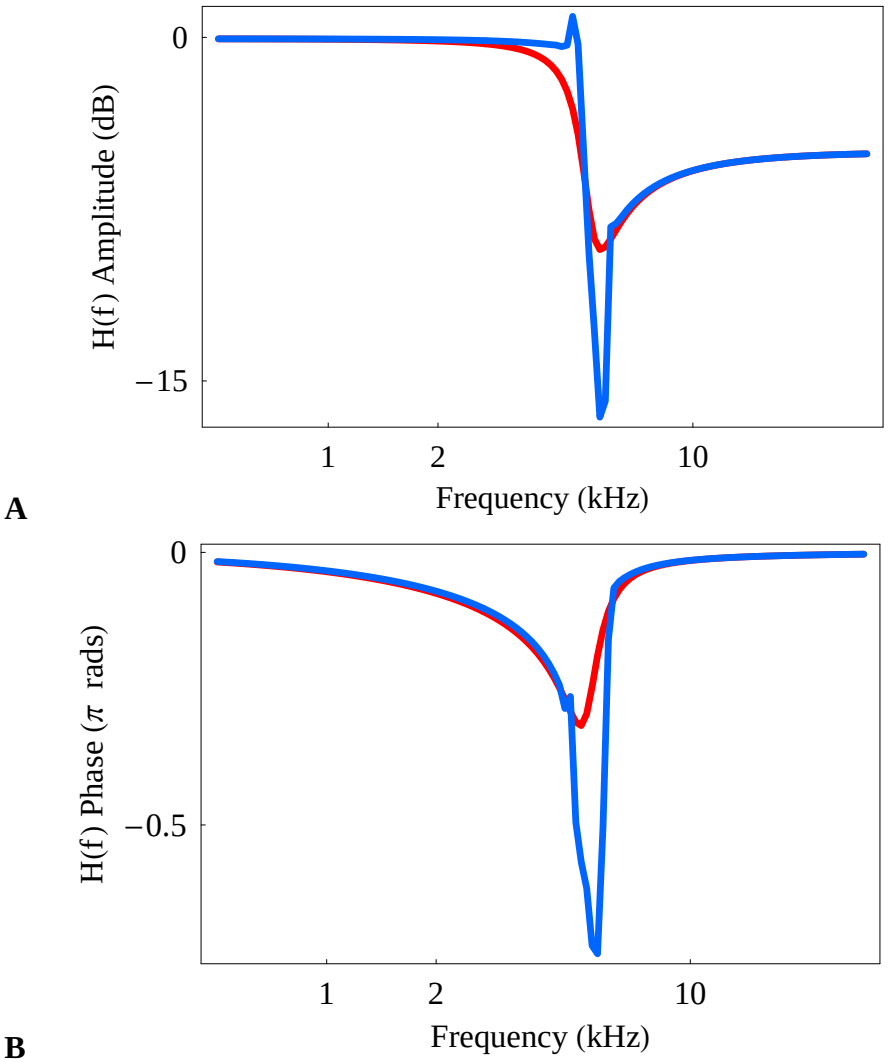

Figure 4.6: Transfer Function $H(f)$ with Loading in the Passive and an Active Case

Frequency responses of transfer function $H_{\text{load}}(f)$. **Top** Amplitude; **Bottom** Phase; **Red** Passive case; **Blue** Active case. The OHC motility factor used is 0.16 while the forward-to-backward ratio is 0.3 for the simulation.

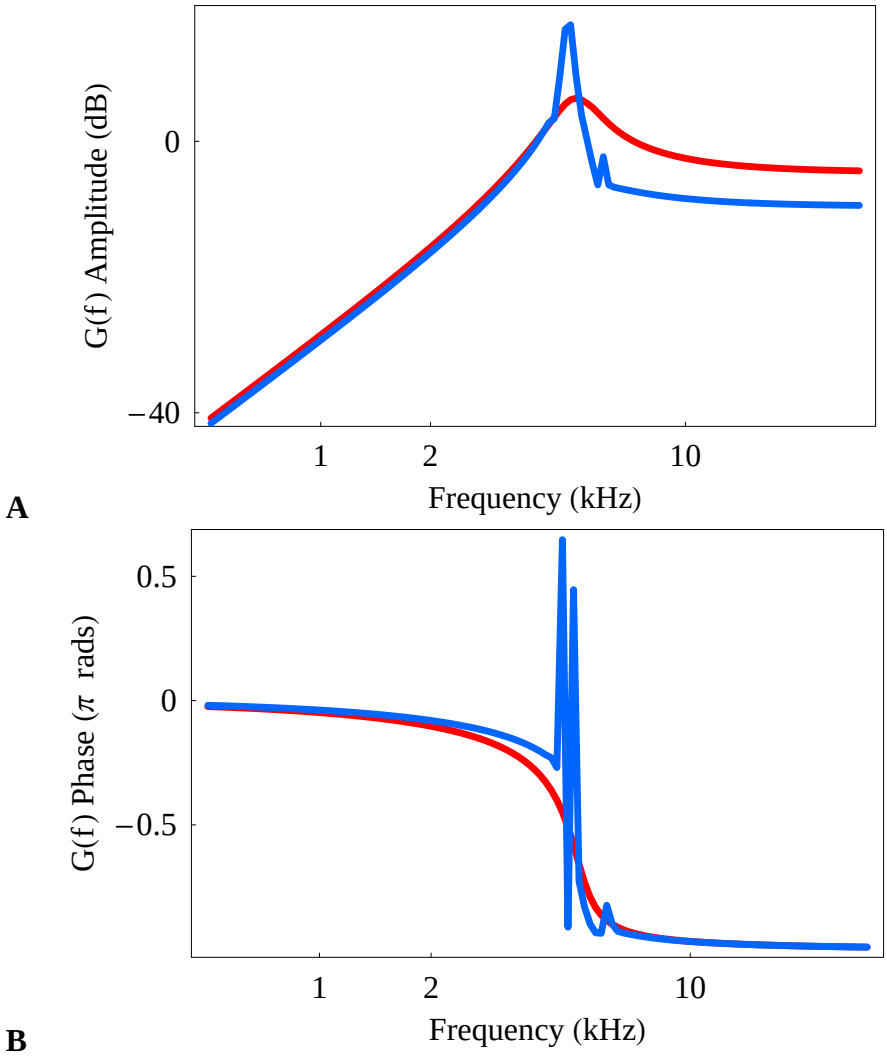

Figure 4.7: Transfer Function $G(f)$ with Loading in the Passive and an Active Case.

Frequency responses of transfer function $G_{\mathrm{load}}(f)$. **Top** Amplitude; **Bottom** Phase; **Red** Passive case; **Blue** Active case. The OHC motility factor used is 0.16 while the forward-to-backward ratio is 0.3 for the simulation.

above and taking the first time-derivative yields:

$$2\rho\ddot{\phi} = S(x)\dot{\delta}(x) + \beta(x)\ddot{\delta}(x) + M(x)\dddot{\delta}(x)$$
$$+r_{\mathrm{fb}}S(x)\dot{\mathcal{T}}\big(\delta(x+d)\big) - r_{\mathrm{ff}}S(x)\dot{\mathcal{T}}\big(\delta(x-d)\big). \tag{4.40}$$

As in the passive design, we used I_{in} to model the quantity $2\rho\phi$ and I_{mem} to represent the BM velocity $\dot{\delta}$. Also, working in the frequency domain (Laplace domain) with $s = j\omega$ gave us:

$$I_{\mathrm{in}}s^2 = S(x)I_{\mathrm{mem}} + \beta(x)I_{\mathrm{mem}}s + M(x)I_{\mathrm{mem}}s^2$$
$$+r_{\mathrm{fb}}S(x)\mathcal{T}\big(\frac{I_{\mathrm{mem}}(x+d)}{s}\big)s - r_{\mathrm{ff}}S(x)\mathcal{T}\big(\frac{I_{\mathrm{mem}}(x-d)}{s}\big)s, \tag{4.41}$$

We based the synthesis of the active model, implementation of F_{OHC}, on the outcome of the passive design. By observing that in the passive design Equation 4.18, the state variable I_{s} was expressed in terms of I_{mem} as

$$I_{\mathrm{s}} = -\frac{I_{\mathrm{mem}}}{s\,\tau_1}. \tag{4.42}$$

We then obtained expressions for $I_{\mathrm{mem}}(x-d)$, received from the upstream BM segment, and for $I_{\mathrm{mem}}(x+d)$, received from the downstream BM segment, as follows.

$$\frac{I_{\mathrm{mem}}(x-d)}{s} = -\tau_{1\mathrm{f}}I_{\mathrm{sf}}, \quad \text{and} \quad \frac{I_{\mathrm{mem}}(x+d)}{s} = -\tau_{1\mathrm{b}}I_{\mathrm{sb}}, \tag{4.43}$$

where $\tau_{1\mathrm{f}}$ and $\tau_{1\mathrm{b}}$ represent the time constant, I_{sf} and I_{sb} the output currents, of the first LPF at the upstream and downstream BM segment, respectively.

To reduce complexity in implementation, we used τ_1 to approximate both $\tau_{1\mathrm{f}}$ and $\tau_{1\mathrm{b}}$ as they have similar values due to the small longitudinal span between neighboring sections. Recall that in the passive system, the BM stiffness $S(x)$ is represented by τ_1, τ_2 and the gain b, $S(x) = (b+1)/(\tau_1\tau_2)$. Thus, the F_{OHC} term in Equation 4.41 was transformed to the following:

$$\begin{aligned} F_{\mathrm{OHC}} &= r_{\mathrm{fb}} S(x)\mathcal{T}(-\tau_1 I_{\mathrm{sb}})s - r_{\mathrm{ff}} S(x)\mathcal{T}(-\tau_1 I_{\mathrm{sf}})s \\ &= r_{\mathrm{fb}} S_0(x)\mathcal{T}(-I_{\mathrm{sb}})s - r_{\mathrm{ff}} S_0(x)\mathcal{T}(-I_{\mathrm{sf}})s, \end{aligned} \tag{4.44}$$

where $S_0(x) = S(x)\tau_1 = (b+1)/\tau_2$. Note that τ_1 was taken out of $\mathcal{T}$ in order to simplify the implementation.

Therefore, we have obtained the target equation for the active system synthesis:

$$\begin{aligned} I_{\mathrm{in}}s^2 = \quad & S(x)I_{\mathrm{mem}} + \beta(x)I_{\mathrm{mem}}s + M(x)I_{\mathrm{mem}}s^2 \\ & + r_{\mathrm{fb}} S_0(x)\mathcal{T}(-I_{\mathrm{sb}})s - r_{\mathrm{ff}} S_0(x)\mathcal{T}(-I_{\mathrm{sf}})s. \end{aligned} \tag{4.45}$$

Following similar synthesis procedures to that used in the passive design, we obtained the synthesis result for an active design, which implemented the BM boundary condition with active coupling, as follows.

$$\begin{aligned} \tau_1 I_{\mathrm{s}} s &= -I_{\mathrm{in}} + I_{\mathrm{o}} - I_{\mathrm{s}}, \\ \tau_2 I_{\mathrm{o}} s &= I_{\mathrm{in}} - bI_{\mathrm{s}} - I_{\mathrm{o}} + r_{\mathrm{fb}}(b+1)\mathcal{T}(-I_{\mathrm{sb}}) - r_{\mathrm{ff}}(b+1)\mathcal{T}(-I_{\mathrm{sf}}), \\ I_{\mathrm{mem}} &= I_{\mathrm{in}} + I_{\mathrm{s}} - I_{\mathrm{o}}. \end{aligned} \tag{4.46}$$

Note that to include implementation of the cochlear amplifier mechanism ABC, we only

needed to add two current quantities into the input of the second LPF in each BM circuit design. The two current signals were taken from the two adjacent neighbors of each BM circuit, respectively. Specifically, I_{sf} and I_{sb} denoted the output current signals of the first LPF, I_{s}, in a BM circuit, fed forward and backward from its upstream (basalward) and downstream (apicalward) BM circuits.

4.3 A Log-Domain Class AB Low-Pass Filter

4.3.1 Nodal Equations

We have synthesized the design for the cochlear fluid and the second-order BM section. We used a single nMOS transistor as a physical model of a small amount of cochlear fluid. Next we shall discuss the implementation of the BM design. We chose to realize the BM circuit differentially. This results in Class AB operation which increases dynamic range, reduces the effect of transistor mismatch, and lowers power consumption. Differential operation also agreed with the way the biological cochlea operates—the vibration of BM is driven by the pressure difference across it.

In a differential design, each signal was represented by the difference between its positive component and negative component. In addition to the constraint applied to differential signals, the operation of a Class AB design also required additional common-mode constraint. Differential- and common-mode conditions combined together and determined the two components of the output signal.

Following a bottom-up strategy, we will present the design of a differential LPF in detail

as a building block based on which we will develop the BM circuit. A current-mode LPF can be described in the frequency domain as:

$$\tau I_{\text{out}} s + I_{\text{out}} = I_{\text{in}} \tag{4.47}$$

where $s = j\omega$ and τ is the time constant. I_{in} and I_{out} are the input and output current, respectively. We wrote the differential-mode equation of the LPF as follows by representing each signal using the difference between its two components (i.e., positive and negative).

$$\tau(I_{\text{out}}^{+} - I_{\text{out}}^{-})s + (I_{\text{out}}^{+} - I_{\text{out}}^{-}) = I_{\text{in}}^{+} - I_{\text{in}}^{-}. \tag{4.48}$$

Using the approach described in [4], we then enforced a common-mode constraint to additionally govern the two components of the output signal. This constraint is chosen as follows:

$$\tau I_{\text{out}}^{+} I_{\text{out}}^{-} s + I_{\text{out}}^{+} I_{\text{out}}^{-} = I_{\text{q}}^{2}, \tag{4.49}$$

where I_{q} set the geometric mean of the positive and negative currents. This equation realized a dynamic common-mode constraint that had the same time constant as the differential mode. At constant input ($s = j\omega = 0$), the following relation holds:

$$I_{\text{out}}^{+} I_{\text{out}}^{-} = I_{\text{q}}^{2} \tag{4.50}$$

Combining the common-mode constraint with the differential design equation, we de-

rived the nodal equations for the positive and negative paths.

$$\begin{aligned} C\frac{dV^{+}_{\rm out}}{dt} &= \frac{I_\tau}{I^{+}_{\rm out}+I^{-}_{\rm out}}\left((I^{+}_{\rm in}-I^{-}_{\rm in})+(\frac{I^{2}_{\rm q}}{I^{+}_{\rm out}}-I^{+}_{\rm out})\right), \\ C\frac{dV^{-}_{\rm out}}{dt} &= \frac{I_\tau}{I^{+}_{\rm out}+I^{-}_{\rm out}}\left((I^{-}_{\rm in}-I^{+}_{\rm in})+(\frac{I^{2}_{\rm q}}{I^{-}_{\rm out}}-I^{-}_{\rm out})\right). \end{aligned} \tag{4.51}$$

Here, C was the capacitance of the capacitors in each paths of the differential-mode LPF. Voltages $V^{+}_{\rm out}$ and $V^{-}_{\rm out}$ were the node voltages of the capacitors; and the current flowing through a MOS transistor gated by $V^{+}_{\rm out}$ was the current signal $I^{+}_{\rm out}$, and same relation applies to $V^{-}_{\rm out}$ and $I^{-}_{\rm out}$.

4.3.2 Circuit Building Block

The nodal equations of the LPF (Equation 4.51) that were derived in the previous section showed that the primitive computations required are multiplication and division. For that implementation, we employed the log-antilog multiplier (Figure 4.8) as the building block of the differential-mode LPF circuit and thereby the BM circuit.

The relation between the input current, $I_{\rm a}$, and the output current, $I_{\rm r}$, in the building block (Figure 4.8) can be described as:

$$I_{\rm r} = \frac{I_{\rm a}I_{\rm b}}{I_{\rm c}} \tag{4.52}$$

where $I_{\rm a}$ was the current flowing through the pMOS gated by $V_{\rm a}$ (and sourced by the power supply rail$V_{\rm dd}$), $I_{\rm b}$ by $V_{\rm b}$, and $I_{\rm c}$ by $V_{\rm c}$. We tied the well (substrate) of the two pMOS transistors gated by $V_{\rm m}$ to their sources, respectively, to eliminate the body effect [4].

[4]Effect on the threshold of a MOSFET when the source to substrate voltage increases. Increase in $V_{\rm sb}$ ($V_{\rm source}-V_{\rm substrate}$) results in increase in threshold voltage and decrease in channel current

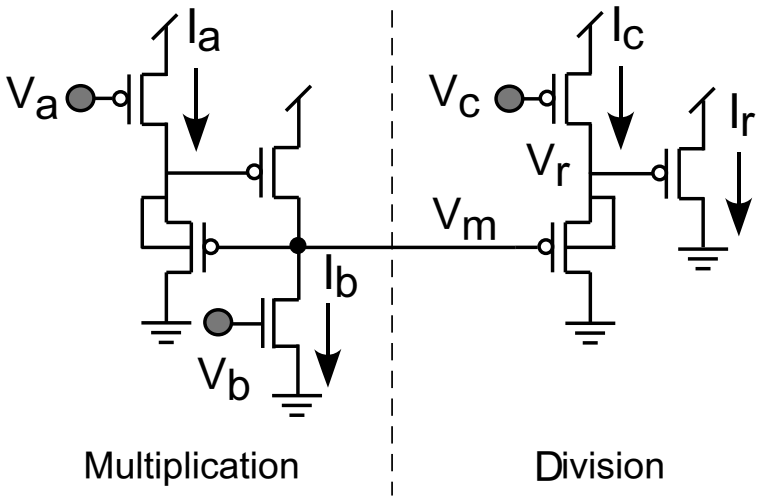

Figure 4.8: Log-Antilog Multiplier

This circuit is the building block of a low-pass filter in the present design. Comprised of only seven transistors, the circuit realizes multiplication and division of currents.

4.4 Log-Domain Class AB Circuit Implementation of the Cochlea

In this section, we will present the transistor-level cochlear circuits, then the cochlear chip architecture. We will first show the Log-domain Class AB circuit of a low-pass filter, two of which will form the BM circuit. With additional circuit for realizing the cochlear amplifier mechanism ABC, we shall present the schematic for the BM circuit in the active case. Last, we will show the architecture of the entire cochlear chip which includes fluid diffusive network, the BM circuit, and the coupling circuit for ABC.

4.4.1 BM Circuit

Using the building block (Figure 4.8), we obtained the circuit of the positive path of a Class AB LPF (Figure 4.9A). The nodal equation set in Equation 4.51 suggests the transistor-level LPF circuit, in which $V_{\rm out}^{+}$ and $V_{\rm out}^{-}$ denoted the voltage on plus- and minus- capacitor nodes, respectively, and each of them gated a pMOS transistor to produce the corresponding current signals, $I_{\rm out}^{+}$ and $I_{\rm out}^{-}$. $V_{\rm in}^{+}$ and $I_{\rm in}^{+}$, $V_{\rm in}^{-}$ and $I_{\rm in}^{-}$, were related in the similar way. The bias $V_{\rm q}$ set the quiescent current $I_{\rm q}$, which was usually close to zero, while V_{τ} determined the current I_{τ}, which was related to the time constant by $\tau = C{\rm u_T}/\kappa I_{\tau}$ ($\rm u_T$ is the thermal voltage, and κ is the subthreshold slope coefficient). Two of these subcircuits, connected to push/pull with each other, formed a complete differential log-domain LPF.

The nodal equations for the two LPFs in the BM design (Equation 4.16) were derived using the same approach as that for obtaining Equation 4.51. Based on the BM design described in Equation 4.46, we put together the BM circuit using two Class AB LPFs and

circuitry that realized their interactions (Figure 4.9). The differential input signals $I_{\rm in}^{+}$ and $I_{\rm out}^{-}$ represented the difference of velocity potentials across the BM, and the differential output signals $I_{\rm mem}^{+}$ and $I_{\rm mem}^{-}$ represented the BM velocity in the upward and downward directions, respectively. As can be seen, the final output $I_{\rm mem}^{+}$-$I_{\rm mem}^{-}$ representing the BM velocity, or $I_{\rm mem}$, was computed as the linear summation of three current signals, $I_{\rm in}$, $I_{\rm s}$, and $I_{\rm o}$.

For realizing the ABC, each BM circuit sent out currents $I_{\rm s}^{+}$ to its two immediate neighbors; each BM circuit also received $I_{\rm T}^{+}$ and $I_{\rm T}^{-}$ from its neighbors, which were saturated version of its neighbor's $I_{\rm s}^{+}$ and $I_{\rm s}^{-}$, respectively. The bidirectional coupling currents, $I_{\rm s}^{+}$ and $I_{\rm s}^{-}$, were saturated simply by passing through a current-limiting transistor which was inserted in series in each of the coupling current pathway (Figure 4.10).

The saturation of the input current through M1 was realized by connecting a current limiting transistor M2 (Figure 4.10). When the input current, $I_{\rm in}$, set by $V_{\rm in}$, exceeded the current level that $V_{\rm sat}$ sets, $V_{\rm x}$ increases which in turn reduced the current through M1. The saturation current, denoted by $I_{\rm rsat}$, was described as

$$I_{\rm rsat} = \mathcal{T}(I_{\rm in}) = \frac{I_{\rm s} I_{\rm sat}}{I_{\rm s} + I_{\rm sat}} \tag{4.53}$$

where $I_{\rm sat}$ was set by the bias voltage, $V_{\rm sat}$.

4.4.2 Spiral Ganglion Cell Circuit

In the cochlea, the mechanical vibration is eventually translated into neural activities; inner hair cells (IHCs) and spiral ganglion cells are the agents for the translation. The output of the biological cochlea is neurotransmitter release at the base of IHC, and ultimately

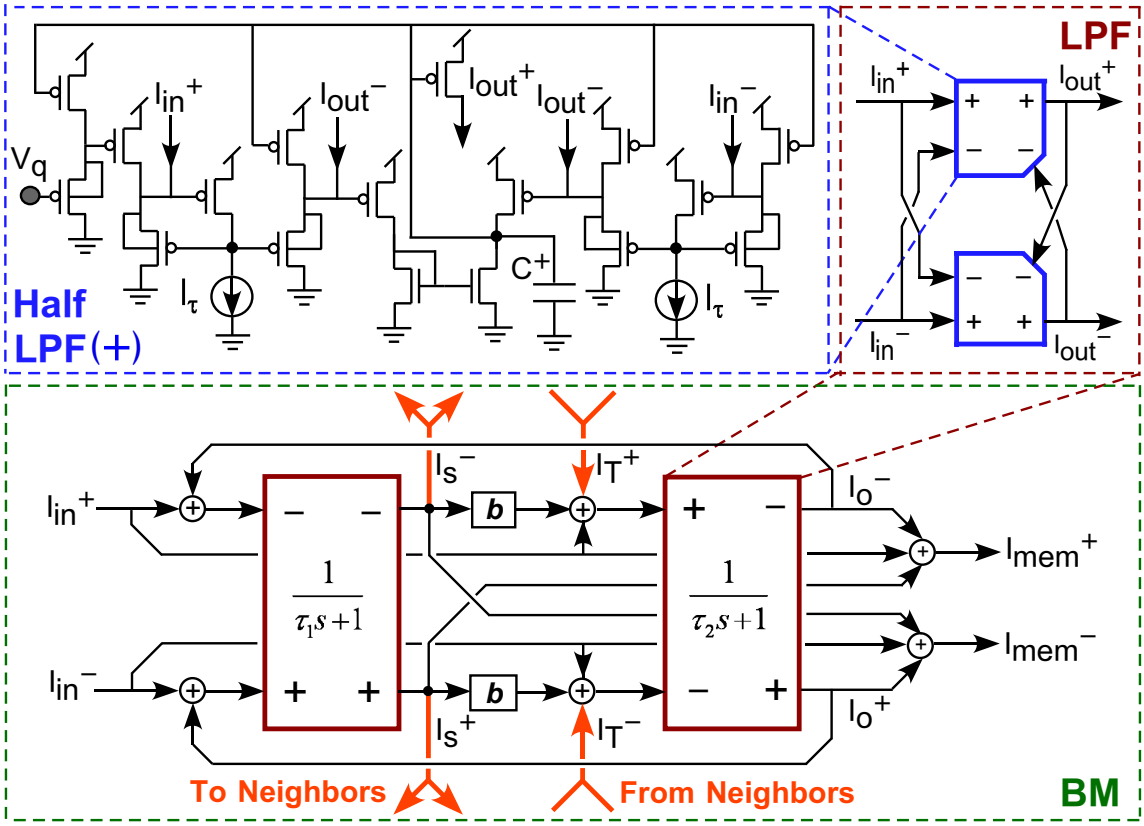

Figure 4.9: Class AB Low-Pass Filter and Basilar Membrane Circuit Design

A Low-pass filter (LPF) subcircuit. **B** LPF circuit formed by two LPF subcircuits. **C** Basilar membrane (BM) circuit. It consists of two LPFs and connects to its neighbors through I_{s} and I_{T}.

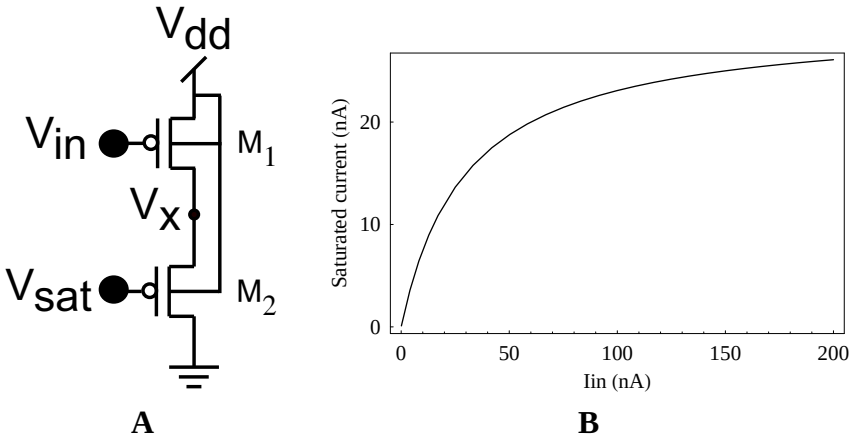

Figure 4.10: Circuit Implementation of Saturation

A Circuit. **B** Mathematical simulation result showing saturation profile of the current that flows through the pMOS transistor with its gate as V_{in}.

neurons' electrical discharges, or spiral ganglion cell's (SGC) spikes.

Several transduction processes occur from the BM's motion to the spikes of the SGCs [18]. The BM's up and down motion causes the cochlear fluid in the sub-tectorial space to move, causing viscous drag which deflects the cilia of inner hair cells (IHC). If the ciliary deflection is in the radially outward direction (i.e., away from the modiolus), IHCs are excited which means that the transduction channels on the hairs open, allowing K^{+} to flow into the IHCs, which in turn depolarizes the IHCs. Depolarization of IHCs causes voltage-gated Ca^{2+} channels to open, and the resultant influx of Ca^{2+} causes neurotransmitter vesicle exocytosis. The neurotransmitter binds with glutamate receptors on the post-synaptic membrane of spiral ganglion cells. The receptor potentials serve as generator potentials that initiate a cascade of events that eventually produce action potentials at the SGCs.

SGCs in the cochlea fall into three categories based on their spontaneous firing rate; there are high-, medium-, and low-spontaneous rate SGCs. In addition to spontaneous rate, they also have different firing-rate profile with sound intensity (rate-intensity or RI) functions [118].

To convert the analog current that represents the BM's motion into digital pulses , or spikes of SGCs, we built a circuit model to emulate the functions of SGCs. First, we modeled the conversion between the BM's velocity to the post-synaptic input current to the SGCS. We used a current-splitter [114] to obtain a half-wave rectified current signal, which represented the depolarizing K^{+} influx. Constrained by chip die size, we did not explicitly model the IHC-SGC synapses in detail; instead, we used a low-pass filter to model the IHC cell membrane's filtering effect.

The circuit has three functional components: circuit to obtain full-wave BM velocity,

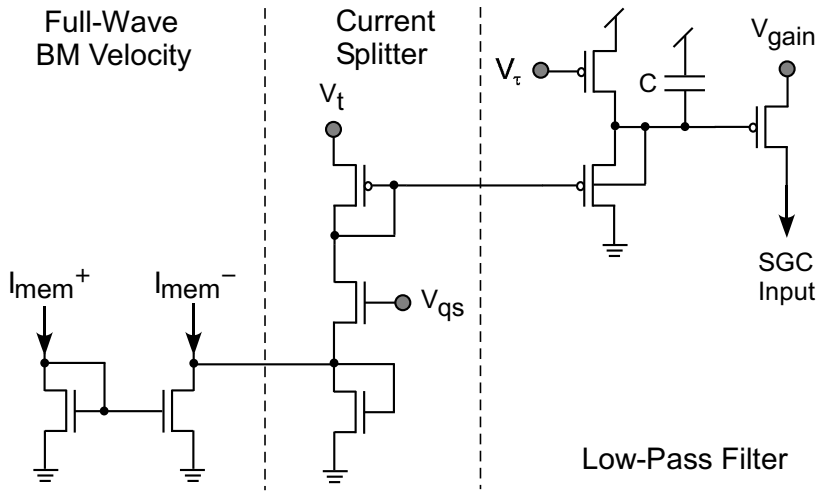

Figure 4.11: Input to Spiral Ganglion Cells

Circuit that models the processes converting BM velocity into the driving current of spiral ganglion cells. The outcome is a half-wave rectified current.

current splitter for generating half-wave currents, and a LPF. The circuit of full-wave BM velocity was formed by taking the difference between the positive and negative components of the BM velocity, ${I_{\rm mem}}^+$ and ${I_{\rm mem}}^-$, which were half-wave rectified, and 180 degree out of phase. Then this sinusoidal signal was split into a positive and a negative current, from which we only used one of them (i.e., a half-wave current with near-zero baseline) as the input for driving SGCs. Last, a LPF filters out the high-frequency component in the half-wave rectified input, emulating the effect of the membrane capacitance of IHCs.

In order to model the difference in their spontaneous rates, our silicon SGC modeled have different gain of the input current (i.e., different bias $V_{\rm gain}$), and modeled the different saturation levels by using different $V_{\rm sat}$ biases. What was in common among the high-, medium-, and low-spontaneous rate SGC circuits are the types of ion channels and their dynamics. Similar to the biology, our silicon SGC model consisted of a depolarizing fast $\rm Na^+$ ion channel, a hyperpolarizing membrane-voltage-dependent $\rm K^+$ channel, a hyperpolarizing $\rm Ca^{2+}$-concentration-dependent $\rm K^+$ channel, and a fast hyperpolarizing $\rm K^+$ channel

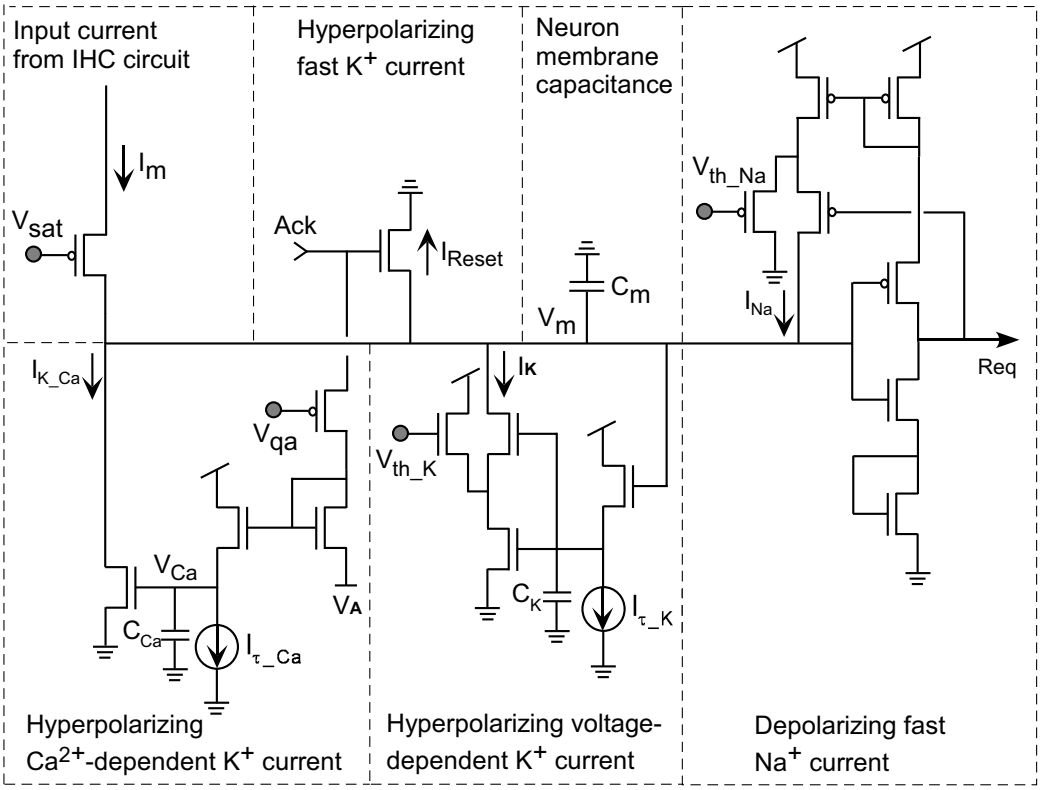

Figure 4.12: Silicon Spiral Ganglion Cells

Transistor-level circuit model of spiral ganglion cells. It consists of Na^{+}, K^{+}, and Ca^{2+} ion channels whose dynamics together shape that of the spiral ganglion cell.

Figure 4.12 (Figure 4.12).

The neurons' spikes were sent off chip through an asynchronous digital communication protocol, address event representation (AER) [119, 120]. AER is an interface designed for transmitting and receiving neuronal spike information between silicon neurons. Instead of communicating using actual spikes of a neuron, each spike is represented by the neuron's unique address (i.e., coordinates) in a 2D array and the address is the token for communication. The form of digital pulses offers the advantage of robustness and high efficiency, compared to an analog code.

Once a neuron's membrane voltage V_{m} (Figure 4.12) reached its threshold, the neuron generated an action potential, or a spike, which then sent a request (Req) to the AER transmitter circuitry. Upon the request was serviced, an acknowledgment (Ack) was received from the receiver (the receiver configured and mounted on the chip test PCB) and the neuron were reset.

4.5 Chip Architecture

We fabricated a version of our design with 360 BM circuits and two 4680-element fluid grids (360$\times$13), with its architecture shown in Figure 4.13 and the chip die shown in Figure 4.14. This chip occupied 10.9 mm^2 of silicon area in 0.25 μm CMOS technology. Differential input signals were applied at the base while the two fluid grids were connected at the apex through a fluid element, which represented the helicotrema. As we can see in the close-up view (at the bottom of Figure 4.13)), BM circuits exchanged their currents realizing ABC, and the level of currents were controlled by a bias V_{sat} realizing the saturation of ABC.

4.6 Summary

In this chapter, we described the process of the cochlear circuit design based on our mathematical cochlear model, including design synthesis and transistor-level implementation. This silicon cochlea comprised the BM and the fluid circuits. The BM design was implemented by two interacting LPFs and the coupling to the cochlear fluid circuit, similar to the biological cochlea in which the BM is driven by the pressure in the cochlear fluids, and the BM's motion in turn affects the motion of the fluid nearby. In order to achieving simpler implementation, larger dynamic range, and low power consumption, we chosen to implement the cochlear circuits in current mode with class AB operation. We synthesized the passive and the active cochlea and implemented the design using current-mode circuit building blocks. Inclusion of our proposed cochlear amplifier mechanism ABC yielded a novel architecture of silicon cochlea design.

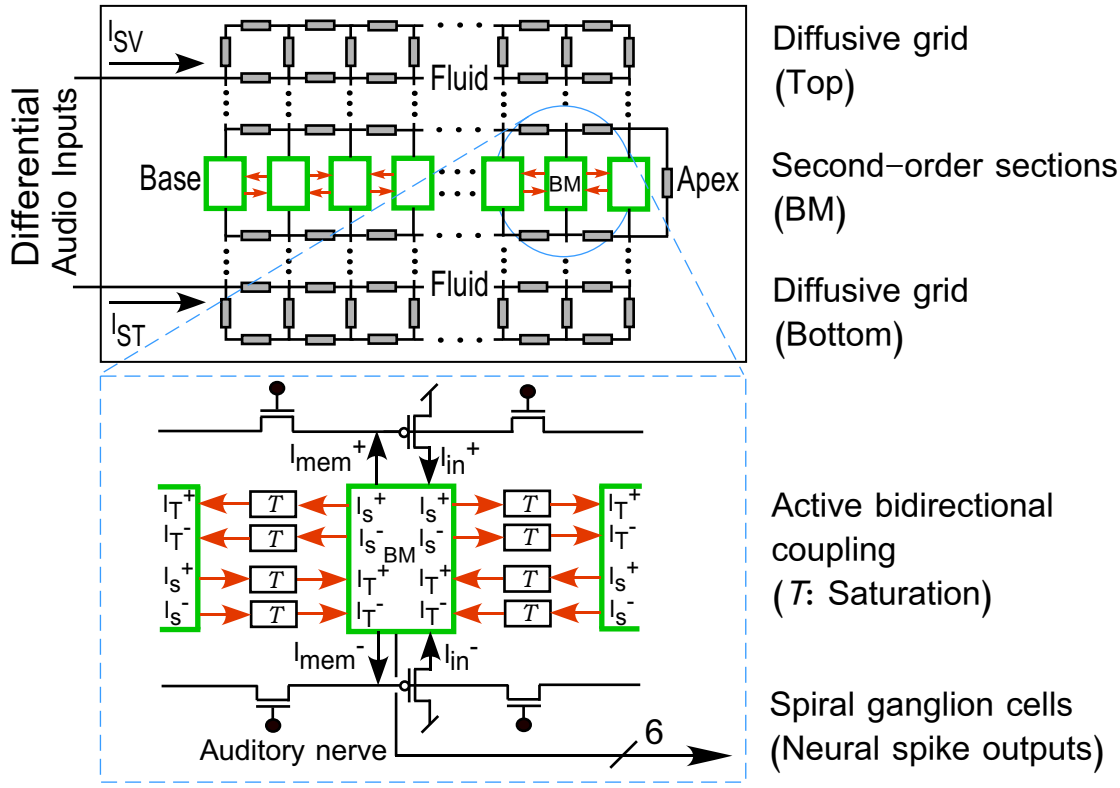

Figure 4.13: Cochlear Chip Architecture

The cochlear chip comprises two diffusive-element grids that model the two cochlear fluid chambers, and 360 basilar membrane (BM) circuits that are embedded in between the two diffusive grids. Each BM segment sends and receives currents from its two immediate neighbors. The current output of each section, representing BM's velocity, drives six spiral ganglion cells that have three different spontaneous firing rates with the ratio of 3:2:1.

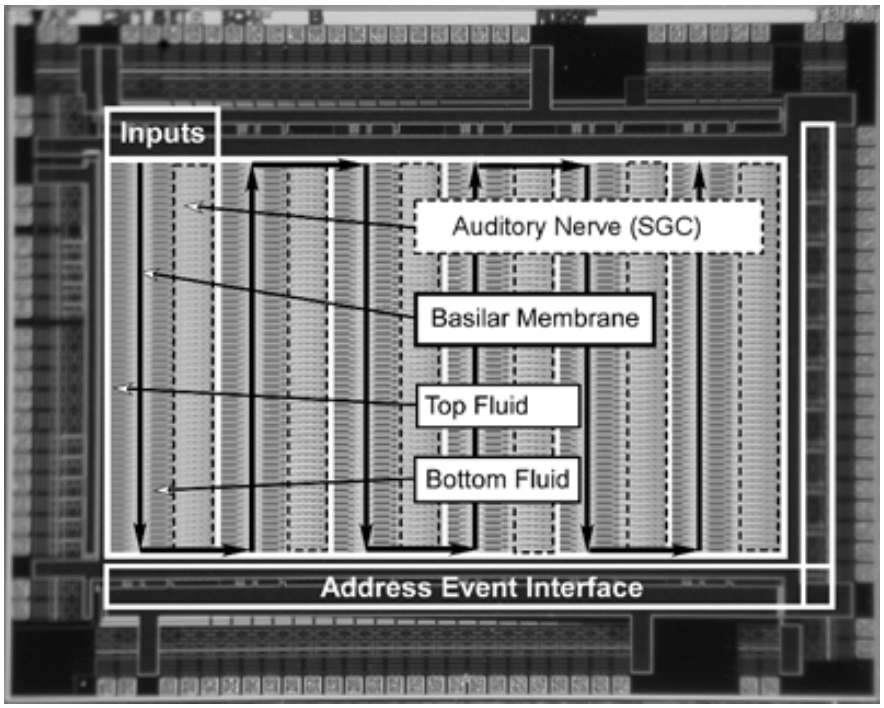

Figure 4.14: Micrograph of Cochlear Chip Die

Different comprising elements of the cochlear chip die are labeled in the micrograph, including the input, the basilar membrane, top/bottom fluid, and the auditory nerve (SGC: Spiral ganglion cell).

Chapter 5

Cochlear Chip Responses to Sound

In previous two chapters, we have elaborated our hypothesis about the cochlear amplifier mechanism, active bidirectional coupling (ABC), in which we proposed that outer hair cell (OHC) motile forces are delivered onto the basilar membrane through the tilted structure within the organ of Corti, thereby giving rise to frequency-selective amplification and nonlinear cochlear responses. In this chapter, we present responses to sound stimuli in our silicon cochlea that was described in detail in Chapter 4.

We first examined the effect of ABC on the basilar membrane's (BM) motion in response to sound stimuli, thereby providing further verification of our hypothesis. We then explored both the frequency responses and longitudinal responses of the silicon cochlea. To demonstrate nonlinearity of the silicon cochlea, we performed experiments that involved measuring BM's responses with varying input intensities. Finally, we obtained spiking activities on the auditory nerve model, which represented the final output stage of the silicon cochlea.

5.1 Chip Test Setup

Input signals of differential nature were required for our Class AB silicon cochlea. To stimulate the chip, we drove the top and bottom diffusive network simultaneously by applying two complementary voltage signals at the beginning of the silicon cochlea, corresponding to the base of the biological cochlea. A voltage signal of a node of the diffusive network represented the logarithm of fluid velocity potential. Therefore, the current flowing through a pMOS transistor that was gated by the node voltage emulates the fluid velocity potential. By the same token, the currents flowing in and out of the two diffusive networks model the complementary inward and outward motion (velocities) of the oval window and the round window of the silicon cochlea.

In order to generate sinusoidal current input for the BM subcircuits, the voltage signals applied were set to be the logarithmic of a half-wave rectified sinusoidal signal with certain offset (i.e., DC level), based on the exponential I-V relationship of transistors operating in subthreshold region. To this end, We obtained the value of κ through transistor characterization from the chip being tested and used this κ value in generating input voltage signals. Further, in order to obtain a set of input current signals with log-linear increase in their amplitude, a linear increase in the amplitude of the input voltage resulted in an exponential increase in input current for the BM subcircuit, through which we obtained a linear increase of current on a logarithmic scale.

Mimicking its biological counterpart, the chip's outputs have two forms. One is the current output at each BM subcircuit representing the BM velocity, can be measured through the voltage across a resistor through which the output current passes. The output current goes through a current sense-amplifier in the output pad before it flows through the resistor. Given the class AB operation of the present design, we measured both current outputs

from the positive and negative paths and then took the difference between the two as the complete output signal. The operation of taking the difference of two output signals is conveniently performed off chip (i.e., through separate circuitry on the test printed circuit board).

We included a serial-analog-multiplexer, or scanner, in the periphery of the chip to facilitate visualizing and measuring analog output signals at any desired chip position. The scanner design we used in our cochlear chip was adapted from [121]. Considering the actual layout of the present silicon cochlea (i.e., columns of cochlear segments alternated in downward and upward directions physically, forming a consecutive cochlea electrically), we used two arrays of shift-registers—in downward and upward directions—connected such that they formed a chain that enabled scanning the entire silicon cochlea sequentially from the beginning of the silicon cochlea (corresponding to the base) to its end (corresponding to the apex). As the adjacent two columns of BM stages in the cochlear chip were arranged in opposite directions, the shift registers in the two columns were arranged in the similar manner to accommodate selection of BM stages in the chip core. By controlling the clock input of the shift registers, we were able to measure output signals of any BM stage (i.e., subcircuit) in the silicon cochlea.

We directed digital-pulse outputs of the cochlear chip—the neuronal spikes on the silicon auditory nerve—to a PC for real-time visualization (including debugging). Through the word-serial address-event representation (AER) interface [120], the spikes were represented in terms of their x and y addresses in the 2D array; then an on-board CPLD (complex programmable logic device) and a USB (universal serial bus) controller were employed for transmitting spike events together with time stamps to a PC program that we developed for displaying the results.

5.2 BM Frequency Responses: Linear Domain

Although measurements of the human cochlea are unavailable, data of other mammalian cochleas are abundant with which we can compare the chip measurements, at least qualitatively. In physiological measurements, pure tones were most often used for obtaining the cochlea's responses. The use of pure-tone stimuli provided a simple and straightforward probe for the cochlea's functions—including spectral analysis and active amplification. To obtain frequency responses, we swept the frequencies of input signals and measured the current outputs (from both positive and negative paths) of the BM subcircuit at certain cochlear location that are selected by the scanner.

5.2.1 Effect of Active Bidirectional Coupling

We investigated the frequency responses for the passive and active cases by varying the saturation level of outer hair cell (OHC) forces, and thus the extent of ABC between BM stages. To that end, we varied the voltage bias V_{sat} that controlled the coupling current level between BM stages.

Increasing V_{sat} decreased the coupling between neighboring BM stages, and vice versa, as V_{sat} gated pMOS transistors. Specifically, the cochlear amplifier (i.e., ABC) was completely shut off by setting V_{sat} equal to or higher than the source of the saturation transistors; that reduced the system to a passive cochlea with only electrical embodiments of the fluid hydrodynamics, BM's physical properties, and interaction between the fluid and the BM. Decreasing V_{sat} increased coupling current level, introducing ABC into the system, thereby giving rise to active cochlear responses.

At each saturation level, the input frequency was swept from 100 Hz to 30 kHz in 45 logarithmically spaced frequencies. At the BM Stage 100, we obtained a series of frequency response curves (Figure 5.1), each of which had a peak—the corresponding frequency at which the stage vibrates maximally, known as the characteristic frequency (CF).

Increasing ABC changed the BM velocity amplitude responses but hardly affected the phase response (accumulation or lag in the traveling wave). As can be seen, with decreasing V_{sat}, the CF at which the peak occurs remains more or less the same (around 4 kHz).

The peak amplitude increased monotonically as a result of increasing strength of ABC (through lowering the bias V_{sat}). Plotted on an arbitrary dB scale (Figure 5.1), the peak height values with increasing ABC level were listed as follows: 18.2, 18.5, 24.1, 26.2, 28.1, 31.6, 33.4, 34.1, and 34.3 dB. Note that the amplitude of the BM velocity were amplified only over a restricted frequency region so that the responses became more sharply tuned. In terms of the frequency tuning, the calculated Q_{10} values increased monotonically in general from 0.45 to 1.14 with increasing ABC levels.

BM velocity phase responses relative to that of the input signal keep almost the same: flat near the base and abrupt accumulation near the CF (Figure 5.1B). This result indicated that a traveling wave was formed along the BM in the silicon cochlea.

5.2.2 Active Cochlear Frequency Responses

Under an active cochlea setting (with maximal saturation current level), we measured frequency responses of six linearly spaced BM stages (Figure 5.2). The six cochlear locations were from Stage 30 to 230, spaced 40 segments apart. The CF that maximally excited the first measured position (i.e., Stage 30) was 12.1 kHz. The remaining five CFs, from early to

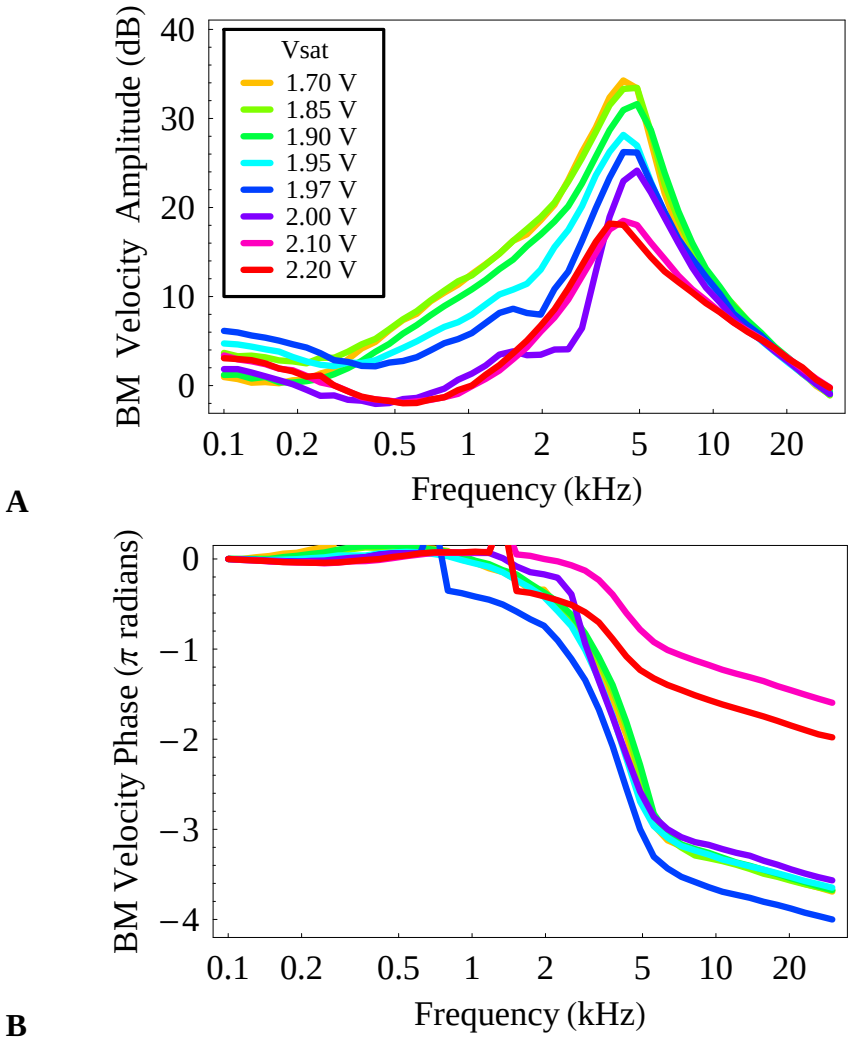

Figure 5.1: Frequency Responses in the Cochlear Chip with Varying Outer Hair Cell Forces

Measured frequency response of the basilar membrane velocity with increasing strength of outer hair cell forces, thus varying ABC. **A** Amplitude. **B** Phase. Decreasing V_{sat} leads to increase in the saturation level, which increases the strength of ABC. The amplitude of the BM velocity increases over a certain frequency range and thus the tuning becomes sharper. The phase responses remains almost the same.

later stages, were 8.2 k, 1.7 k, 905, 366, and 218 Hz, respectively. Their tip-to-tail ratio values (amplitude difference between the response peak to the lowest response value) are 27, 18, 27, 17, 22, 26 dB, respectively. Q_{10}s were also calculated as 1.4, 2.7, 2.2, 1.3, 1.4, 2.2, respectively. The cutoff slopes were -21, -38, -54, -20, -20, -46 dB/Octave, respectively.

Measurements from the chinchilla cochlea were also plotted in Figure 5.2 for comparison (dashed lines). Q_{10} of the chinchilla cochlea was 2.55 at mid-sound intensity (computed from [47]) and the cutoff slope was about -85 dB/octave (computed from [47]). In the chip, the phase accumulation at the CFs ranged from 0.56 to 2.67π radians, comparable to 1.67π radians in the mammalian cochlea ([47]). Despite some irregularities with the response shape (which were related to Q_{10} and cutoff slope) and peak height, the chip responses were comparable to the biological data qualitatively.

We performed frequency-response measurements with the chip at several more cochlear positions, from Stage 10 to 230, which were spaced by 20 stages, thereby we obtained the frequency-position map in the chip. The frequency-position map depicted the tonotopic (spatial) mapping of the spectral analysis that the cochlea performs. To obtain such a map, we plotted the characteristic frequency for each BM stage we measured against its cochlear position (Figure 5.3). The expression in Figure 5.3 is the regressed relationship between the CF and cochlear position. It was evident that despite some deviation due to transistor mismatch, the CFs decreased linearly on a logarithmic scale with the increasing cochlear positions, thus distance from the beginning of the silicon cochlea.

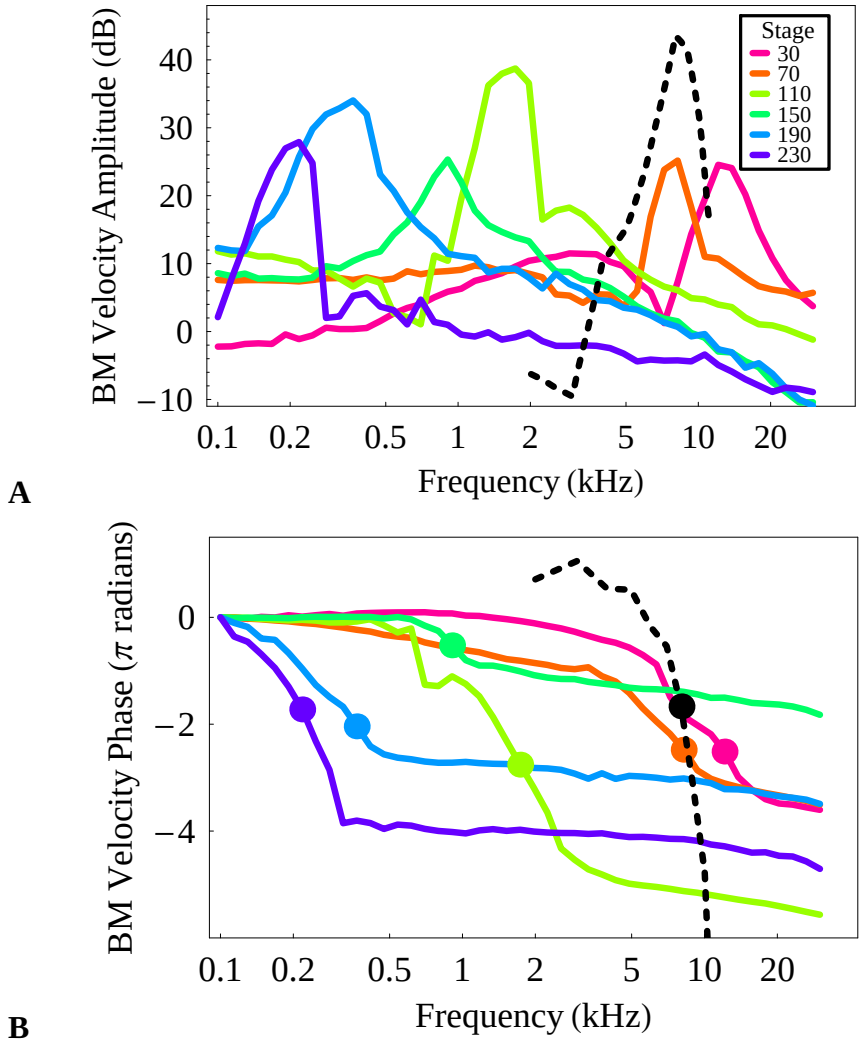

Figure 5.2: Frequency Responses in the Cochlear Chip Compared to Biology

Frequency responses of the basilar membrane (BM) velocity at different cochlear positions are obtained and compared with physiological data measured in chinchilla cochlea [47]. **A** Amplitude. **B** Phase. These linearly spaced BM stages, ranging from the beginning to the end of the silicon cochlea, have characteristic frequencies that shift from high to low. In addition, the responses are comparable to biological measurement in terms of shape, peak amplitude, and the phase accumulation.

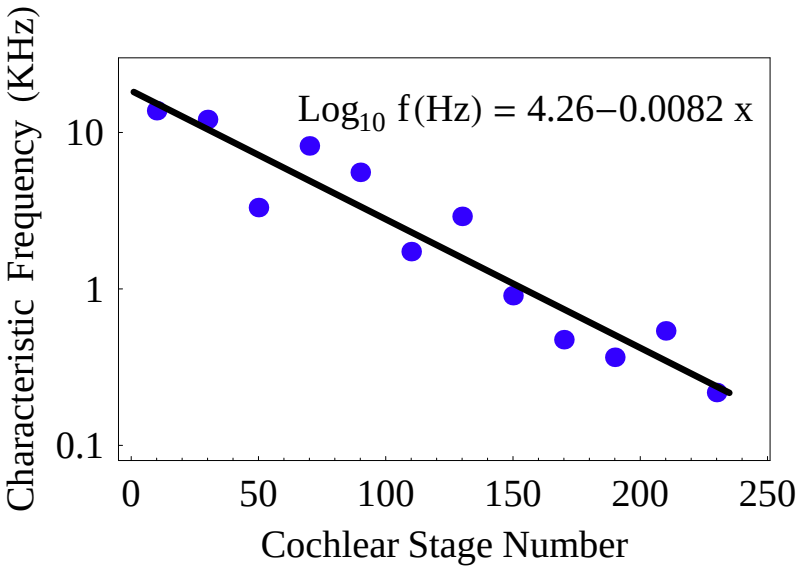

Figure 5.3: Measured Frequency-Position Map in the Cochlear Chip

The expression in the figure describes the regressed function, indicating a linear relationship between the characteristic frequency, f, and the cochlear position, x (x is in the unit of stage number).

5.3 Nonlinear Frequency Responses

We investigated the nonlinearity of the cochlear responses due to saturation of ABC. In an active-cochlea parameter setting (high saturation level of ABC), we varied the input current level and obtained the BM velocity frequency responses at the Stage 100 (Figure 5.4). We increased the input voltage level linearly such that the corresponding current into the BM increase exponentially; the input level (in dB) was then calculated based on the input voltage and measured value of κ from the chip being tested. The dynamic range of input current was limited on the high side by the threshold of transistors, and on the low side by the noise floor of the output current.

BM Stage 100 responds to increasing input intensity distinctively at different frequencies. As expected in the log-scale plot, we observed the linearly increasing BM responses in the lowest frequency region. In contrast, the BM responses around the CF did not increase linearly with the input level as the near-CF region was where ABC took effect. Thus, saturation of OHC forces caused the compression, or compressive growth, with the increasing input levels locally around the CF region. Figure 5.4B shows the phase responses of the BM velocity, relative to that of the input signal.

The peak amplitude increases monotonically in a compressive way, which is evident when we plot the peak amplitude against the input intensity (Figure 5.5). As can be seen, the amplitude at the CF (peak) increase more linearly when input intensity is low while it grows compressively when the input level is high, resulting in 24 dB compression between the input and the output. In Figure 5.4, at lower frequencies, the output increases more linearly than at the peak. The CFs at increasing input intensities hardly change while in the biological cochlea the peak shifted a little basalward (to lower-frequency side) [32].

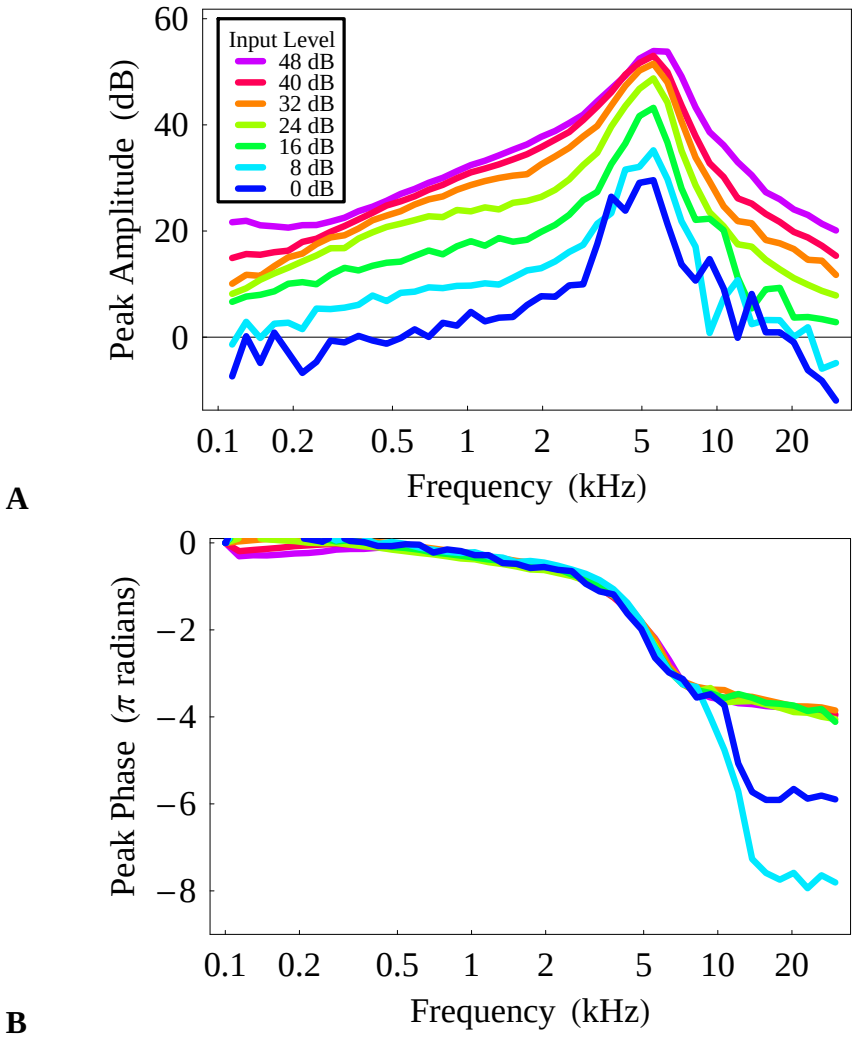

Figure 5.4: Nonlinear Compression in the Cochlear Chip

Chip data of BM velocity frequency responses at different input levels. **A** Amplitude. **B** Phase. The input levels (dB) were listed in the figure legend: they were 8 dB spaced, ranging from 0 to 48 dB.

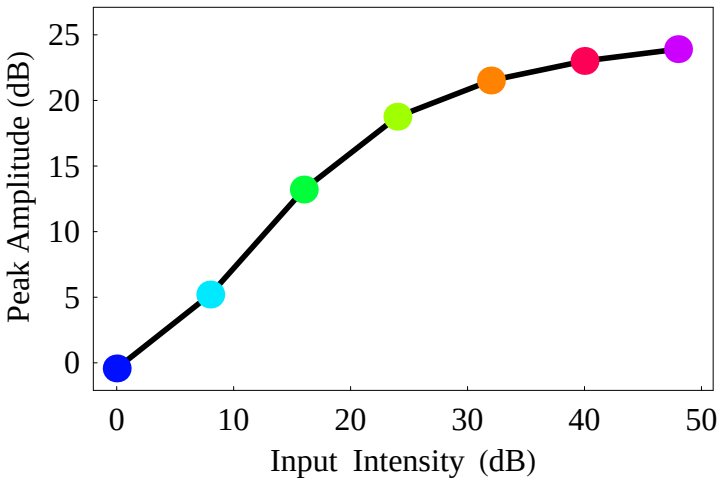

Figure 5.5: Saturating Input-Output Function in the Cochlear Chip

The basilar membrane velocity at the characteristic frequency (i.e., peak amplitude) saturated with the input intensity.

The tuning of the responses became broader with increasing input level; Q_{10}s were 1.8, 1.6, 2.2, 1.6, 1.4, 1.4, and 1.1, respectively (monotonically except for the 16 dB input, due to some artifacts at lower input levels whose responses were noisier); the cutoff slopes were -44, -29, -35, -24, -19, -16, and -13 dB/Octave, respectively; again, they became shallower monotonically except for the response at 16 dB input. The phase plots at different input level overlapped with one another, nearly independent of the input intensity. The larger phase plateau at the lower input levels (0 and 8 dB) were due to the noisy responses at the cutoff; as a result, the plateau occurred at -6π and -8π for the two lower input levels, respectively, just one or two more cycles than that of other phase response curves.

5.4 Longitudinal Patterns

Longitudinal responses of the cochlea are the spatial patterns of BM vibrations in response to input sound. We measured the longitudinal responses of BM velocity in the cochlear chip by applying sinusoidal current input (input voltages were logarithm of sinusoidal signals). At 500 Hz pure tone input, we measured the BM responses at every single stage and then we obtained the smoothed response by taking a moving average over 10 stages (Figure 5.6).

We measured the silicon cochlea's responses at 2 kHz input in the passive and active case (Figure 5.7). In the active case, where the largest possible coupling gain between BM stages was set, the cochlea showed larger response peak (about 14.6 dB) than that in the passive case where there was no coupling made possible. In addition, the cutoff slope was much steeper in the active case than in the passive case.

Stimulating the chip using three additional input frequencies independently—500 Hz, 1, 2, and 4 kHz—we obtained the BM velocity longitudinal responses (Figure 5.8). 4 kHz input elicited a BM response peak at Stage 85 (defined as the characteristic place, or CP) while 500 Hz sound traveled all the way to Stage 178 and peaked there. In addition, the CPs for 1k and 2kHz were Stage 166 and 139, respectively. The tip-to-tail ratios of the responses from 500 Hz to 4 kHz were 13, 14, 32, and 12 dB, respectively. Q_{10}s were 1.1, 0.9, 1.2, and 0.9, respectively. The cutoff slopes were -70, -16, -27, and -21 dB/Octave, respectively.

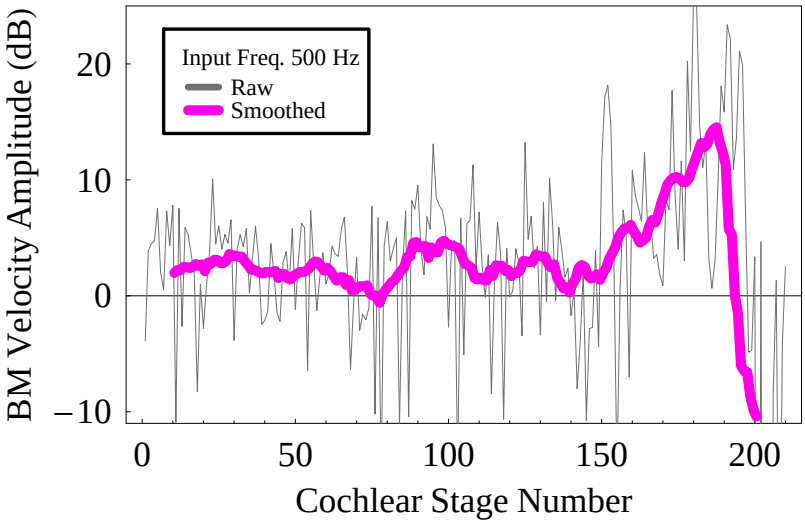

Figure 5.6: Longitudinal Responses in the Cochlear Chip (I)

Measured BM longitudinal responses at 500 Hz input frequency. Gray: Raw data. Magenta: Smoothed data (10-stage moving average).

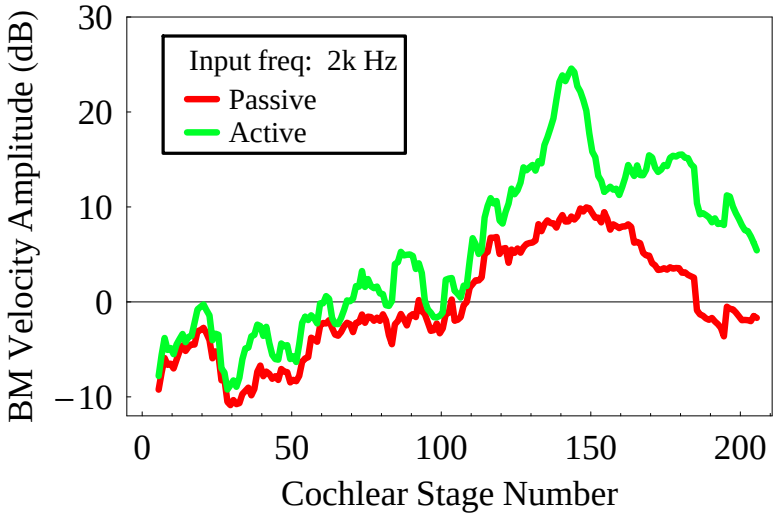

Figure 5.7: Longitudinal Responses in the Cochlear Chip (II)

Measured BM longitudinal responses at 2 kHz input frequency in the passive case and in an active case. Curves are smoothed data (10-stage moving average).

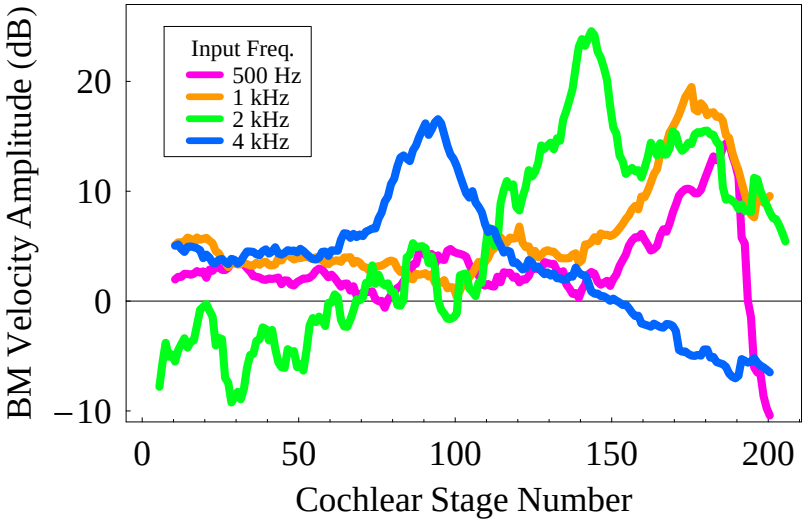

Figure 5.8: Longitudinal Responses in the Cochlear Chip (III)

Input frequency varies from 500 Hz to 4 kHz, resulting in response peaks at different cochlear positions (10-stage moving average).

5.5 Silicon Auditory Nerve's Spike Activities

The silicon auditory nerve in our cochlear chip converted the BM's mechanical motion into electrical discharge patterns, or spikes that encoded a sound wave's frequency, intensity and temporal information. The sound signal's frequency was represented by neuronal spikes at certain cochlear positions, or frequency channels; the temporal structure of sound signals were replicated in terms of the temporal responses of the frequency channels. Sound intensity was coded by the firing rate of the spiral ganglion cells, whose axons formed the auditory nerve.

Cochleargram

We measured real-time auditory nerve responses to a complex sound stimulus. The complex sound comprised a chirp followed by a click. We constructed the chirp by sweeping frequency linearly on a logarithmic scale from 16 kHz to 200 Hz for 1.5 seconds. The click contained 50 frequency components on a logarithmically linear scale. The spectrum of the constructed sound signal was plotted in Figure 5.9.

We presented this complex sound to the silicon cochlea and obtained the spike responses on the silicon auditory nerve. There were two ways for generating the differential input signals: one is to download signal data points into two function generators and to use their output signals (out-of-phase half-wave rectified sinusoidal) as the input of the chip, the other is to play the sound signals in a PC and use the sound card output to drive the chip. We then obtained a cochleagram from the chip response (Figure 5.10), in which the silicon cochlea responded to frequencies from high to low at cochlear positions from the beginning (the base) to the end (the apex), and all of the frequency channels in the input frequency range were activated by the click sound.

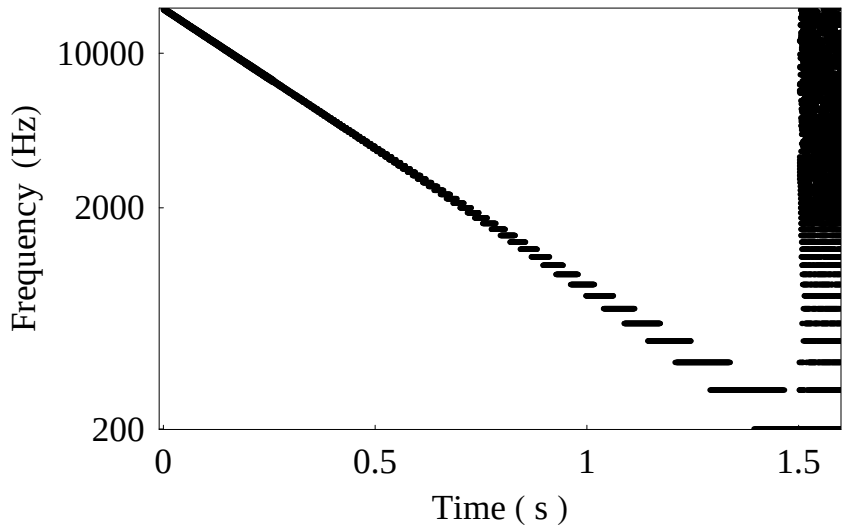

Figure 5.9: Spectrum of A Complex Sound

In the spectrotemporal pattern of a complex sound stimulus (Frequency vs. time plot), the first component was a 1.5-second chirp, with frequency sweeping from 16 kHz to 200 Hz logarithmically to match the log-frequency position map of the cochlea. Each of the all 50 frequency components lasted for the same number of periods thus for a frequency-dependent duration. The second part of the complex sound was a click-like sound for 0.1 second, which comprised all of the 50 frequencies.

In this cochleagram, we plotted the spike outputs of all the three types of spiral ganglion cells (SGC) for cochlear channels ranging from 1 to 240, which amounted to spike activities of 1440 (i.e., $240x6$) frequency channels. The channel activities from Stage 240 to 360 (near the end of the silicon cochlea) were omitted in the cochleagram because the responses outputs were not satisfactory under the bias setting used.

We could now appreciate one of the advantages of building analog VLSI model of the cochlea, from the perspective of complex-sound processing. This mixed-mode silicon cochlea responded to sound, simple or complex, in real time; in contrast, responses to the complex sound discussed above would take thousand times more time to obtain in software simulation running on a PC. The real-time characteristic is desirable in engineering applications such as sound/speech preprocessing in automatic speech recognition systems.

Rate-Intensity Function

Firing rate varying with input intensity is one of the coding approaches that the biological auditory nerve employs for representing intensity. We measured the average firing rate at the characteristic place in the cochlea for a given sinusoidal input, and we obtained the firing rates with increasing input intensity, a relation called the rate-intensity (RI) function.

We observed different RI functions for different SGC types, namely high-, medium, and low-spontaneous rate (HSR/MSR/LSR) SGC (Figure 5.11). The input to the SGC cells is a low-pass filtered version of a half-wave rectified signal that represents the upward velocity of the BM.

In the chip, there were two major differences in the parameter setting among the three types of SGCs. On one hand, HSR SGCs were assigned a higher gain bias voltage than the MSR and LSR SGCs so that $V_{\mathrm{gainH}} > V_{\mathrm{gainM}} > V_{\mathrm{gainL}}$. Under this setting, HSR SGCs

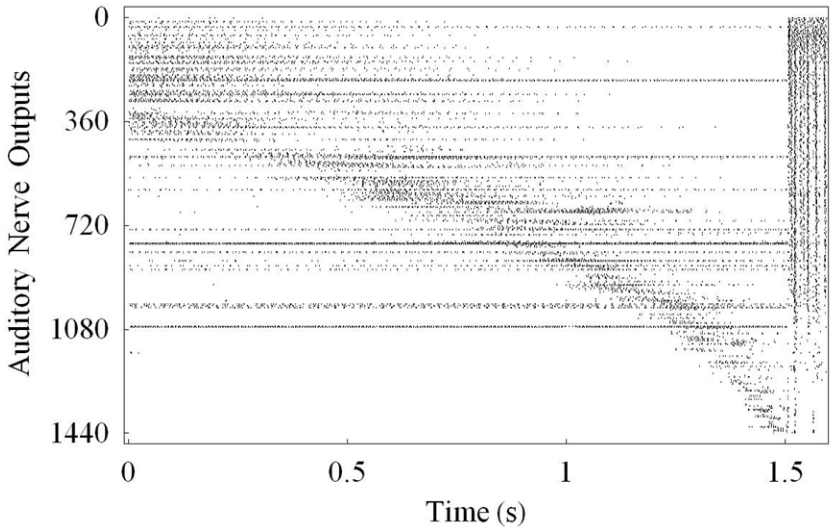

Figure 5.10: Measured Cochleagram from the Cochlear Chip

The spectrotemporal structure of the sound stimulus is described in Figure 5.9. In response to the chirp, the neuronal spiking activities shifted from high-frequency channel (i.e., near the beginning) to low-frequency channels (i.e., near the end). In response to the click, almost all of the channels shown in the plot generated spikes simultaneously.

obtained larger input current than MSR and LSR SGCs while MSR SGCs were stimulated more than the LSR SGCs. By setting the neuron's firing threshold at an appropriate level, the three types of SGCs exhibited different firing rate, which can be interpreted as different spontaneous rates. On the other hand, the saturation levels of the depolarizing input current were set differently; the gate voltage of the pMOS transistor for the HSR was set to be higher than the other two types of SGCs so that starting from certain input current level the firing rate of the HSR SGCs saturated while the MSR and LSR SGCs did not show such saturation profile.

Four different RI types have been reported in the chick cochlea nerve ([118]), while only three RI function profiles have been found in the guinea pig [122]. In our chip, we only modeled the major three types of RI functions for simplifying the design—saturating for HSR SGCs, sloping-up for MSR SGCs, and straight for LSR SGCs.

Comparing the RI function we obtained from the silicon cochlea with the physiological data ([118, 122]), we found that our chip showed similar RI functions as that in the biological cochlea. As seen in Figure 5.11, HSR SGCs generated spikes even at the lowest input intensities, while MSR and LSR neurons kept silent until the input intensity increased to a certain level; LSR SGCs had an even higher threshold than the MSR SGCs. With the input level increasing, the HSR SGCs' firing rate saturated while the firing rate of LSR SGCs continued to increase.

5.6 Nonideality in Chip Responses

We have shown in the previous sections that our silicon cochlea's responses demonstrate the characteristic features observed in the biological cochlea. Meanwhile, we also observed

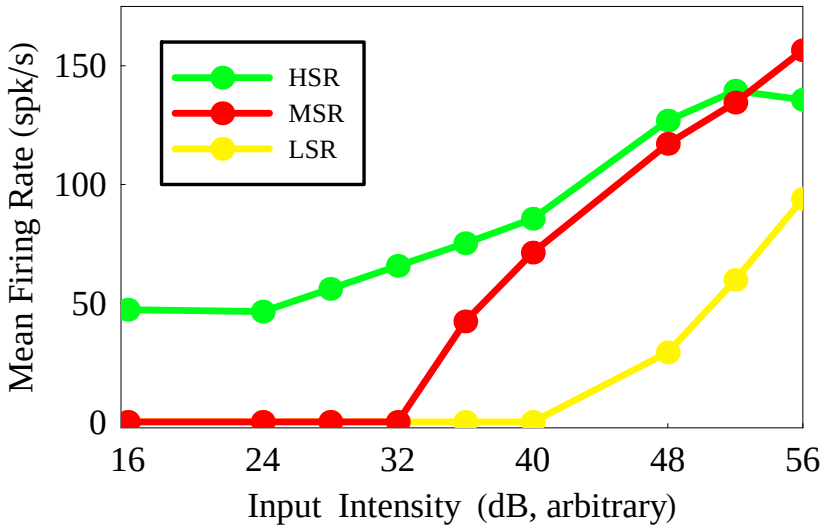

Figure 5.11: Rate-Intensity (RI) Functions Measured From the Cochlear Chip

The average firing rates of the silicon auditory nerve vary with the input intensity. The spike raw data of silicon spiral ganglion cells (SGCs) were collected at Stage 110 for an 4 kHz pure tone input and the firing rates were calculated. Different parameter settings (voltages) were used for generating distinct RI functions for high-, medium-, and low-spontaneous rate (HSR/MSR/LSR) SGCs.

that the chip responses were different across the chip (e.g., in shape or amplitude), and/or deviated somewhat from physiological measurements. This variation in responses can be largely attributed to the variation in parameter setting (voltages) in the chip.

We shall explore the possible cause of the variation of chip parameters, thus suggesting possible ways of reducing the nonideality with chip responses. We first describe the circuit parameters that model the physical properties of the cochlea and discuss what an optimal setting is. We then investigated the effect of transistor mismatch on chip responses due to variations in the chip parameters.

Parameter Settings in the Cochlea Chip

We shall find out what the optimal bias voltage settings should be for achieving desired responses that are quantitatively comparable with the physiological measurements or the mathematical model responses. It is not reasonable to pursue precise matching thereby exactly the same responses across the chip because that is not the case even in the biological cochlea. It is also not practical to find a set of parameters to make chip responses the same as the mathematical model responses because the hardware and the software modeling work in different modeling paradigm—software simulation is performed under an ideal condition without ant variations, while a VLSI system is unavoidably subject to nonideality in the physical medium that are introduced by the fabrication process. However, it is instructive to scrutinize the effect of parameter settings and their variations because the resultant knowledge will help the physical model yield more realistic responses.

We repeated the circuit analogs of the stiffness S, damping β, and mass M of the BM,

as follows.

$$\begin{aligned} S &= \frac{b+1}{\tau_1\tau_2}, \\ \beta &= \frac{1}{\tau_1}+\frac{1}{\tau_2}, \\ M &= 1. \end{aligned} \tag{5.1}$$

Form the above expressions, we calculated the damping ratio as:

$$\begin{aligned} \xi &= \frac{\beta}{\sqrt{SM}} \\ &= \frac{\tau_1+\tau_2}{\sqrt{(b+1)\tau_1\tau_2}} \end{aligned} \tag{5.2}$$

The damping ratio value we chose in our mathematical simulation was 0.2, resulting in a quality factor of 5 for this second-order system. In order to realize this damping ratio in the chip by equalizing Equation 5.6 with 0.2 and solving the equation, the relationship between the time constants τ_1 and τ_2, and the gain factor b was calculated as:

$$\tau_1 = (0.02b - 0.98 + 0.02\sqrt{(b+1)(b-99)})\tau_2, \tag{5.3}$$

or

$$\tau_1 = (0.02b - 0.98 - 0.02\sqrt{(b+1)(b-99)})\tau_2. \tag{5.4}$$

The relations above suggest that to obtain real-value time-constant solutions, the gain factor b should be set to be equal to or greater than 99. In our circuit design, b is calculated as:

$$b = e^{V_b - V_{dd}} \tag{5.5}$$

where voltages were in the unit of $\mathrm{u_T}$, the thermal voltage at room temperature. To this end, the bias voltage V_b needs to be set somewhat higher than $\mathrm{V_{dd}}$. Let us look at an example of the setting to get a flavor of the relation between τ_1 and τ_2, in which we made $b = 100$ meaning that V_b was about 0.12 V higher than V_dd. Then we obtained:

$$\tau_1 = 0.819\tau_2, \qquad \text{or} \qquad \tau_1 = 1.221\tau_2 \tag{5.6}$$

In other words, only when this relation was satisfied across the chip (along the silicon cochlea) can the desired damping ratio be realized. The larger b, the larger ratio between τ_1 and τ_2.

Note that τ_1 and τ_2 should increase exponentially along the cochlear position in the chip. Also, a time constant τ is related to the time-constant current, namely I_τ as follows.

$$\tau = \frac{C\mathrm{u_T}}{\kappa I_\tau}. \tag{5.7}$$

We had two electrical variables for controlling the time constants, the capacitor C and the current I_τ. In practice, it is convenient to have C fixed (corresponding to constant area for capacitance in chip layout) and to decrease I_τ along the silicon cochlea. For each BM stage, each of the two time-constant bias voltages was tied to a node on a polysilicon wire. These nodes across the chip were linearly spaced, which in turn results in exponentially spaced time-constant currents due to the exponential I-V (current-voltage) relation in transistors' subthreshold-regime operation. A polysilicon wire with certain voltage potential difference at its two ends were known as a tilt poly line.

With regard to keeping the ratio between τ_1 and τ_2, we need to maintain the ratio at the starting and ending terminals of the tilt poly lines. Assuming that the time constant ratio is

r, we have the relations as:

$$\begin{aligned} \tau_1(x) &= r\tau_2(x), \\ \Longrightarrow I_{\tau 1} &= \frac{1}{r} I_{\tau 2}, \\ \Longrightarrow V_{\tau 2} - V_{\tau 1} &= \frac{\mathrm{u_T}}{\kappa} \log(r). \end{aligned} \tag{5.8}$$

where we can see from that the two voltage tilt lines needed to have the same space constant.

From Equation 5.6 only, the values of r was determined by b and $V_{\tau 1}$ can be set either larger or smaller than $V_{\tau 2}$. In oder to help determine which τ of the second-order section should be set higher, we needed to consider what setting will give rise to optimal responses.

Recall that the quality factor Q of the BM second-order section can be computed as

$$\begin{aligned} Q &= \frac{\sqrt{SM}}{\beta} \\ &= \frac{\sqrt{b+1}}{\sqrt{\tau_1/\tau_2} + \sqrt{\tau_2/\tau_1}} \end{aligned} \tag{5.9}$$

Note that this Q was not directly indicative of the value of Q_{10} in the cochlear chip responses because the tuning, or frequency selectivity, of the cochlea is the outcome of a collective network behavior that comprised the loading effects among a number of second-order sections. From Equation 5.6, we can see that when $\tau_1 \gg \tau_2$:

$$Q = \sqrt{(b+1)\frac{\tau_2}{\tau_1}} \tag{5.10}$$

or when $\tau_2 \gg \tau_1$:

$$Q = \sqrt{(b+1)\frac{\tau_1}{\tau_2}} \tag{5.11}$$

The highest Q can be obtained when $\tau_1 = \tau_2$, which is $\sqrt{b+1}/2$. Therefore, a larger value

of b will result in a higher Q.

However, another issue should also be considered—the parameter setting should be optimal so that the chip's responses become enhanced to the relatively large extent when the active mechanism, ABC, is activated. As a reference, we repeated the second LPF that includes the ABC design below.

$$\tau_2 I_{\mathrm{o}} s = I_{\mathrm{in}} - bI_{\mathrm{s}} - I_{\mathrm{o}} - r_{\mathrm{fb}}(b+1)\mathcal{T}(I_{\mathrm{sb}}) + r_{\mathrm{ff}}(b+1)\mathcal{T}(I_{\mathrm{sf}}). \tag{5.12}$$

As we know from the derivation above, the gain factor b has to be equal to or greater than 99, which adds at least two orders of magnitude gain for the current I_{s} on the right side of Equation 5.6. For that purpose, together with the subthreshold-regime current level in mind, we want to have a relatively small value of I_{s} relative to other current quantities, I_{o} for example. Therefore, we chose the latter case in Equation 5.6 for setting τ_1 and τ_2 such that the effect of the last two terms, which implemented ABC, become relatively larger once included. Of course, the effect of ABC can be additionally augmented by raising the gain factors r_{fb} and r_{ff} in Equation 5.6.

Variations in Parameters due to Transistor Mismatch

Device mismatch in integrated circuits refers to the variations in transistor's properties and characteristics. It is essentially caused by random difference in dopant density in the transistor channels. In practice, two identically designed transistors are never exactly identical. Much research has characterized and modeled the device mismatch [115] and has shown that the variation in the threshold voltages is one of the dominant sources underlying the drain-source current and gate-source voltage mismatch [115]. The threshold mismatch, ΔV_{T}, is due to the fluctuation in dopant density across the chip. These fluctuations exhibit

a Gaussian (or normal) distribution with a standard deviation, $\sigma(\Delta V_{\mathrm{T}})$; it can be modeled as:

$$\sigma(\Delta V_{\mathrm{T}}) = \frac{A_{V_{\mathrm{T}}}}{\sqrt{WL}} \tag{5.13}$$

where $A_{V_{\mathrm{T}}}$ is a proportionality constant that is technology-dependent, W is the channel width and L is the channel length [115,123]. As can be seen from Equation 5.13, increasing the channel area (either W or L or both) obviously decreases the standard deviation of the variation in threshold voltage, but it is only employed to a very limited extent due to the high cost in terms of chip die area. Due to this design tradeoff, transistor mismatch inevitably contributes to variations in model parameters. Specifically, in our cochlear chip, the variations in parameters τ_1, τ_2, and b would result in variations in the implemented stiffness S, damping β, and mass M.

In order to investigate the effect of parameter variations on the BM response, we simulated our mathematical model with additionally added log-normal distributed variations to the model parameters (i.e., the BM's stiffness and damping). Circuit analogs of these parameters are scaled current variables (according to Equation 5.1 and the relationship between time constants and current variables described in Equation 5.7). Therefore, these parameters with variances are lognormally distributed, to a first-order approximation, because their logarithms (i.e., voltage) are normally distributed.

According to [123], $A_{V_{\mathrm{T}}}$ in 0.25 μm technology is about 6 mV, which give the value of $\sigma(\Delta V_{\mathrm{T}})$ to be around 1.4% (based on Equation 5.13) for a 10 by 10 λ nMOS transistor (mostly common in our chip) with its threshold voltage around 0.36 V. Therefore, in our simulation under nonideal condition, we applied the standard deviation σ ranging from 0% (zero variation) to 2% to the logarithmic of mean parameter values, which has normal distribution.

We found that model responses deviated from the ideal result, exhibiting smaller peak amplitude and less sharp tuning and getting noisier with increasing σ (Figure 5.12). This simulation provided just one example of the effect of parameter variations on model responses, thus we can gain understanding on the causes of the nonideal chip responses. Multiple simulation can be performed further to obtain the distribution of some characteristics of the BM displacement response (e.g., peak amplitude, Q_{10}, cutoff slope, etc.).

The effect of variation can be somewhat compensated by increasing the OHC motility factor α in model simulations (Figure 5.13). This simulation example showed that increasing the OHC motility factor α raises the response peak but causes the cutoff slope (slope of the response curve after the characteristic place) to become shallower than that when there is no variation. In practice, we increase the source bias V_{ff} and V_{fb} in the chip to increase the OHC motility factor. The extent of this raise is limited as instability would occur if the coupling among BM stages were too large. The non-steep cut-off slope was also observed in our chip's BM velocity responses (Figure 5.2) as a result of increasing OHC motility factor.

In the biological cochlea, variations also exist with the physical properties of its comprising components. They do not, However, seem to deteriorate the cochlear behavior to a severe extent. In other words, the biological cochlea tackles the variation problem somehow, likely through averaging responses locally as inner hair cells sense the nearby-fluid's velocity, which is a collective outcome of neighboring BM fibers' motion. This suggests a possible solution in the silicon cochlea design—to average BM responses locally and use the smoothed BM responses as input signals to inner hair cell and the spiral ganglion cells.

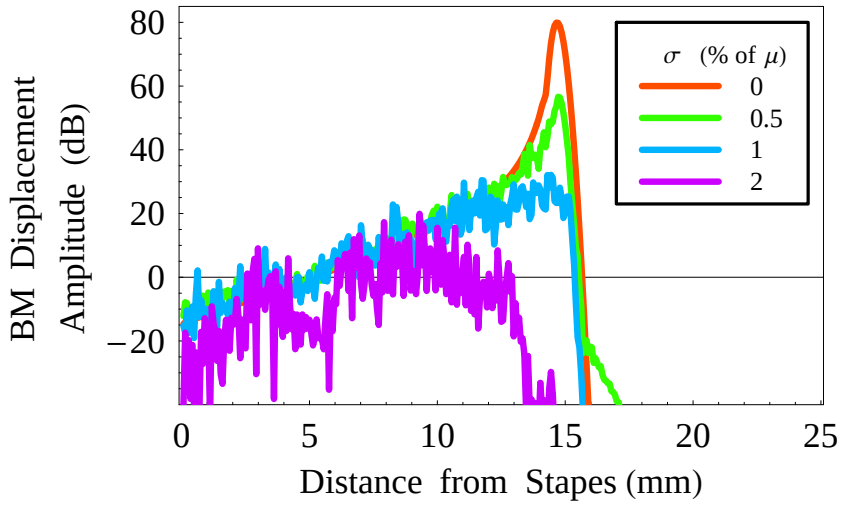

Figure 5.12: Effect of Log-Normal Variations in Parameters on Model Responses

Basilar membrane (BM) displacement responses at 2 kHz pure tone input are obtained with Log-Normal distributed variation added to original model parameters of fluid density ρ, BM stiffness S, damping β. Mass M was kept without variation to match the circuit implementation scheme (constant mass). The values of standard deviation σ used are 0% (original case), 0.5%, 1%, and 2% of mean (log) values. With increasing variation, the BM displacement peak becomes reduced and the tuning becomes broader.

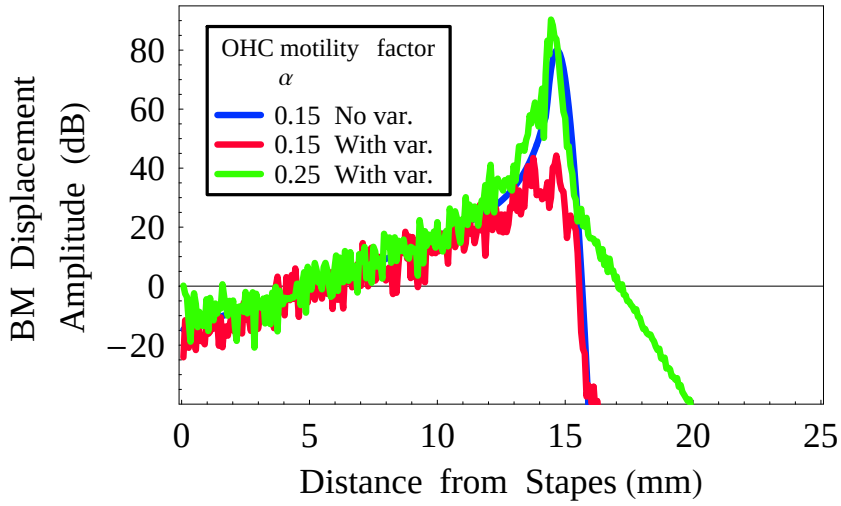

Figure 5.13: Effect of Log-Normal Variations and OHC Motility on Model Responses

Effect of Log-Normal variations on model responses can be remedied to a certain extent through increasing the OHC motility factor α. The responses shown are examples with the standard deviation of the normal-distributed variation was set to be a relatively high value, 1% of the mean (log). When the OHC motility factor α is increased from 0.15 to 0.25, basilar membrane displacement peak is raised but the cutoff slope apical to the peak becomes shallower compared to the model response without variation.

5.7 Summary

Measured chip responses have demonstrated that inclusion of the OHC motility, simply through the coupling between BM neighboring sections, enhances the basilar membrane responses' amplitude response and frequency selectivity, turning a passive cochlear model into an active one. This active model produces cochlear responses that are qualitatively comparable to physiological data. The cochlear chip consumed 52 mW power when ABC was activated and the silicon auditory nerve's spiking activities were being generated. The overall performance of the present silicon cochlea is generally superior to existing designs, in terms of response amplitude, sharpness of tuning and working frequency range.

Compared to the biological cochlea or the present mathematical cochlear model, the silicon cochlea does not exhibit quantitatively comparable responses—its response peak amplitude was smaller even when ABC was included, although its phase responses are realistic. The BM response curves also existed irregular shapes across the chip. These undesirable features of chip responses are mainly caused by transistor mismatch, which gives rise to parameter variations. Since the cochlear model took on a physical form, silicon medium, to mimic the biological cochlea, it is subject to both advantages and constraints that are imposed by the medium, the similar way as the biological cochlea has evolved. The design, thereby performance, of a physical model relies on our understanding of the biological system; meanwhile, the final yield for functionality is also dependent on hardware design techniques and implementation approaches. Therefore, performance optimization is the next step in improving the silicon cochlea through reducing the negative effect of device mismatch. This highlights an important issue for neuromorphic system design that are compact, operates in subthreshold, and consumes low power—in addition to mimicking the organization and function, neuromorphic systems should also learn from the nature's

approaches for overcoming the physical constraints and combating the effect of variations.

What have we gained from building the silicon cochlea? Despite its less realistic responses compared to software simulation, a hardware cochlear model is superior to a mathematical model on several aspects. First, it runs in real time with electronically tunable model parameters. This is especially attractive when processing complex sound such as natural sound and speech, which usually require a great amount of computation resource if simulated on a computer. Second, the low-power feature and compact design of analog VLSI cochlear models promise a variety of applications. For example, it could work as the acoustic front end of automatic speech recognition system on a mobile phone or a personal digital assistant. It can also be tranformed into a fully-implantable cochlear implant if a microphone can be embedded on the chip. Above all, through building the silicon cochlea, we learned what it takes to build a system that emulates a biological system and what the constraints are.

Chapter 6

Conclusions

The human cochlea transduces sound waves into the basilar membrane (BM) vibrations and auditory nerve electrical discharge patterns. The cochlea decomposes complex sound into its spectral components, representing them as vibrations at different locations along the BM. This creates a tonotopic map of frequency along the cochlear partition. When performing the spectral analysis, the cochlea achieves exquisite sensitivity and remarkable frequency selectivity due to nonlinear active amplification of cochlear mechanics.

Although the outer hair cell (OHC) electromotility has been widely thought to amplify the traveling wave [18], the exact manner in which OHCs enhance cochlear function remains unclear. In other words, understanding of how the cochlear amplifier (CA) gives rise to the BM's exquisite frequency sensitivity and selectivity is still lacking. Cochlear modeling has been extensively employed to help deepen our understanding about how the cochlea works. Cochlear models were based upon what has been known but also make predictions on what still remains unknown and suggest further physiological experiments.

6.1 Summary of Present Work

The present effort was dedicated to explore a plausible CA mechanism that is possibly based on the cochlear microanatomy. We hypothesized a CA mechanism in which OHC motile forces actively couple the otherwise weakly coupled BMs transverse fibers, through the tilts of Deiters cells and of their phalangeal processes (PhPs), as observed anatomically. We implemented this cochlear amplifier mechanism, named active bidirectional coupling (ABC), in both a mathematical model and an analog VLSI microchip to reproduce nonlinear active cochlear behavior.

The ABC mechanism captured structural features of the cochlear microanatomy and thereby provided biologically plausible explanations to the outstanding question of how the cochlear amplifier is realized. In the organ of Corti, the OHCs are tilted toward the base of the cochlea while the phalangeal processes (PhPs) are tilted toward the apex. It is assumed in our model that this tilted structural organization very likely provides an efficient means to transmit OHC motile forces onto the BM. Due to the tilted structure, OHC forces are delivered in both forward and backward longitudinal directions, enhancing the cochlea's sensitivity and tuning. In addition, it is widely accepted that the saturating nature of OHC forces imparts to the cochlea nonlinearity, which is also incorporated in the ABC mechanism.

We formulated a two-dimensional nonlinear active model based on ABC. The numerical simulation results showed that activation of ABC boosted frequency-selective amplification, sharpened tuning, as well as increased sensitivity. Additional simulation demonstrated that the tilted structure was of primary importance in the cochlear amplifier because including OHC motility without taking into account the tilts of OHC and PhP was not as effective as ABC in terms of producing active amplification. Furthermore, including satu-

ration of OHC forces, as observed physiologically, produces compressive growth near the characteristic place (CP) at high sound levels. And when two tones are present, the louder one suppresses the other to a larger extent at higher suppressor intensity.

Analysis of the model revealed that the introduced OHC forces through the tilted structure leads to negative damping right before the peak over a restricted region in the cochlea. Further analysis showed that the tilts work as an array of spatial filters, only amplifying the traveling wave in the vicinity of the response peak where the shortening wavelength becomes comparable to the OHC (and PhP) tilt distance.

Our cochlea model may be tested by measuring the wavelength of the traveling wave in live (active) and dead (passive) cochleas. In the long-wave region, the model predicts a 9% longer wavelength in the active case. In the short-wave region, the model predicts a 81% shorter wavelength in the active case. Furthermore, the traveling wave peak amplitude was displaced 3.2 mm apically in the active case; negative damping should occur between these two peak locations.

Embodying a nonlinear active cochlear model in analog VLSI realizes cochlear processing in real time with low power consumption. We implement ABC in a silicon cochlea, resulting in a novel design architecture that addressed the problems of existing designs. Our cochlear chip comprises circuits that model the cochlear fluid, the BM, and the bidirectional delivered OHC forces. The measured chip responses demonstrate that when ABC was activated, larger amplification and sharper tuning is achieved. Through limited currents that represent ABC, the chip responses show nonlinear saturation at high sound levels. In addition, our chip also included silicon spiral ganglion cells, whose digital-pulse encoded output emulates the spike patterns of auditory nerve.

The present cochlear modeling efforts and results have a great deal of implications in the study of cochlear mechanics, clinical experiments, and sound-related engineering problems. Our mathematical and VLSI cochlear models will function as computational tools in scientific exploration of the auditory system. With its basis in cochlear microanatomy, the ABC-based cochlear model has clinical significance in understanding OHC-related hearing loss as well as in improving speech-preprocessing for cochlea implants. In addition, the cochlear model, especially the silicon cochlea, provides a basis for building silicon audition that involves emulating the human auditory system. Last, the new architecture of the silicon cochlea gives insight into the design of cochlea-like sound-processing microchips.

6.2 Future Work

The human auditory system has been recognized as the most efficient and noise-robust speech recognition system [124]. Human is capable of perceiving and recognizing sound/speech signals in rather noisy or reverberant environment with very low error rate while the state-of-the-art automatic speech recognition (ASR) system fails to perform well even with the most advanced computation resource. Therefore, building models that morph the superior capability of the auditory system in processing sound and speech, referred to as neuromorphic audition, would provide insightful hints or even solutions to the engineering problem of building ASR as well as shed light on understanding of auditory processing mechanisms.

Building cochlear models, in mathematics and VLSI, are a starting point of building neuromorphic auditory systems. The present silicon cochlea, inspired by the cochlear amplifier mechanism, can generate neuronal spikes that encode the input sound; its output is ready to drive systems that model higher auditory processing centers to perform more

auditory tasks such as pitch perception and sound localization. Therefore, in addition to improving the present cochlear model, future work along the track would include exploring practical applications using the silicon cochlea and developing neuromorphic auditory models.

On the model improvement side, the present cochlear model can incorporate more anatomical details of the cochlea, for example, the difference between the base and the apex, in order to generate more realistic cochlear behavior. More simulation of cochlear nonlinearity, such as distortion product otoacoustic emission, could further verify the notion that cochlear function is closely association with its structure and anatomy. Reducing effect of transistor mismatch in the silicon cochlea would result in more physiologically comparable behavior.

On the application side, an automatic speech recognition system could potentially benefit from the cochlea-like sound processing of the present silicon cochlea: it runs in real time and it's responses exhibit nonlinearity. Development of neuromorphic VLSI chips that emulate further auditory processing will allow more complicated tasks because each processing center in the auditory hierarchy seems to extract different features (e.g., frequency, timing, and location) of incoming sound. Building such models would be extremely challenging because it requires not only sufficient understanding of the auditory system, which is still rather limited although our knowledge about its working is experiencing extension through both experimental and theoretical approaches, but also advanced circuit and system design techniques. Nevertheless, it is no doubt a rewarding task because once the real-time low-power neuromorphic auditory system is built, it can be used to test our hypothesis of the auditory mechanisms; it can be applied to preprocess sound and speech in attempt to improve the performance of current ASRs, especially in acoustically-cluttered environment; Also, with appropriate silicon-neural interfaces, it can potentially substitute current

auditory prosthetic devices due to its advantages of low power consumption, compact size, and real-time biomorphic signal processing.

Appendix A

List of Abbreviations

1D	One-dimensional
2D	Two-dimensional
2TS	Two-tone suppression
ABC	Active bidirectional coupling
AER	Address event representation
ASR	Automatic speech recognition
BM	Basilar membrane
CA	Cochlear amplifier
CF	Characteristic frequency
CMOS	Complementary metal-oxide semiconductor
CMRR	common-mode rejection ratio
CP	Characteristic place
dB	Decibel
DC ($Re\ biology$)	Deiters' cell
DC ($Re\ engineering$)	Direct current

FD	Finite-difference
HSR	High spontaneous rate
IHC	Inner hair cell
IP	Inner pillar
IPC	Inner pillar cell
LG	Liouville-Green
LPF	Low-pass filter
LSR	Low spontaneous rate
MSR	Medium spontaneous rate
MOSFET	Metal-oxide-semiconductor field-effect transistor
OC	Organ of Corti
OHC	Outer hair cell
OP	Outer pillar
OPC	Outer pillar cell
PhP	Phalangeal process
RI	Rate-intensity
RL	Reticular laminar
SA	Semi-analytical
SAS	Semi-analytical solution
SGC	Spiral ganglion cell
SPICE	Simulation program with integrated circuit emphasis
VLSI	Very large scale integration
WKB	Wentzel-Kramers-Brillouin
WKBJ	Wentzel-Kramers-Brillouin-Jeffereys

Bibliography

[1] C. A. Mead and M. A. Mahowald. A silicon model of early visual processing. *Journal of Neural Networks*, 1(1):91–97, 1988.

[2] K. A. Boahen. A retinomorphic vision system. *IEEE Micro*, 16(5):30–39, 1996.

[3] K. A. Boahen. The retinomorphic approach: Pixel-parallel adaptive amplification, filtering, and quantization. *Analog Integrated Circuits and Signal Processing*, 13(1-2):53–68, 1997.

[4] K. Zaghloul and K. A. Boahen. An on-off log domain circuit that recreates adaptive filtering in the retina. *IEEE Transactions on Circuits and Systems I: Regular Papers*, 52(1):99–107, 2005.

[5] R. F. Lyon and C. A. Mead. An analog electronic cochlea. *IEEE Transactions on Acoustics, Speech, and Signal Processing*, 27(5):292–295, 1988.

[6] L. Watts. *Cochlear Mechanics: Analysis and Analog VLSI*. Ph. D. thesis, California Institute of Technology, Pasadena, California, 1993.

[7] E. Fragniére. A 100-channel analog CMOS auditory filter bank for speech recognition. In *IEEE International Solid-State Circuits Conference Digest of Technical Papers*, pages 140–141, 2005.

[8] P. Merolla and K. A. Boahen. A recurrent model of orientation maps with simple and complex cells. In S. Thrun and L. Saul, editors, *Advances in Neural Information Processing Systems*, volume 16, pages 995–1002. MIT Press, Cambridge, Massachusetts, 2004.

[9] T. Y. W. Choi, P. A. Merolla, J. V. Arthur, K. A. Boahen, and B. E. Shi. Neuromorphic implementation of orientation hypercolumns. *IEEE Transactions on Circuits and Systems I: Regular Papers*, 52(6):1049–1060, 2005.

[10] B. Taba and K. A. Boahen. Topographic map formation by silicon growth cones. In S. Becker, S. Thrun, and K. Obermayer, editors, *Advances in Neural Information Processing Systems*, volume 14, pages 1139–1146. MIT Press, 2002.

[11] J. V. Arthur and K. A. Boahen. Recurrently connected silicon neurons with active dendrites for one-shot learning. In *Proceedings of IEEE International Joint Conference on Neural Networks*, volume 3, pages 1699–1704, 2004.

[12] J. V. Arthur and K. A. Boahen. Learning in silicon: Timing is everything. In B. Sholkopf and Y. Weiss, editors, *Advances in Neural Information Processing Systems*, volume 17. MIT Press, Cambridge, Massachusetts, 2006.

[13] W. E. Brownell. Observation on a motile response in isolated hair cells. In W. R. Webster and L. M. Aiken, editors, *Mechanism of Hearing*, pages 5–10. Monash University Press, Melbourne, Australia, 1983.

[14] W. E. Brownell, C. R. Bader, D. Bertrand, and Y. De Ribaupierre. Evoked mechanical responses of isolated cochlear outer hair cells. *Science*, 227:194–196, 1985.

[15] C. D. Geisler and C. Sang. A cochlear model using feed-forward outer-hair-cell forces. *Hearing Research*, 86:132–146, 1995.

[16] T. Fukazawa. How can the cochlea amplifier be realized by the outer hair cells which have nothing to push against? *Hearing Research*, 172(1):53–61, 2002.

[17] K. Lim and C. R. Steele. A three-dimensional nonlinear active cochlear model analyzed by the WKB-numeric method. *Hearing Research*, 170:190–205, 2002.

[18] C. D. Geisler. *From Sound to Synapse: Physiology of the Mammalian Ear*. Oxford University Press, New York, 1998.

[19] J. L. Flanagan. *Speech Analysis Synthesis and Perception.* Springer-Verlag, New York, 2nd edition, 1972.

[20] P. Dallos. Overview: Cochlear neurobiology. In P. Dallos, A. N. Popper, and R. R. Fay, editors, *The Cochlea*, Springer Handbook of Auditory Research. Springer-Verlag, New York, 1996.

[21] L. L. Beranek. *Acoustics.* McGraw-Hill, New York, 1954.

[22] M. A. Ruggero, N. C. Rich, L. Robles, and B. G. Shivapuja. Middle-ear response in the chinchilla and its relationship to mechanics at the base of the cochlea. *Journal of the Acoustical Society of America*, 87(1612-1629), 1990.

[23] M. C. Killion and P. Dallos. Impedance matching by the combined effects of the outer and middle ear. *Journal of the Acoustical Society of America*, 66:599–602, 1979.

[24] D. W. Fawcett. *A Textbook of Histology*. Chapman & Hall, New York, 12th edition, 1994.

[25] C. Angelbor and H. Engstrom. Supporting elements in organ of Corti I: Fibrillar structures in supporting cells of organ of Corti of mammals. *Acta Otolaryngologica*, pages 49–60, 1972.

[26] N. B. Slepecky. Structure of the mammalian cochlea. In P. Dallos, A. N. Popper, and R. R. Fay, editors, *The Cochlea*, Springer Handbook of Auditory Research. Springer-Verlag, New York, 1996.

[27] W. S. Rhode. Observations of the vibration of the basilar membrane in squirrel monkeys using the Mössbauer technique. *Journal of the Acoustical Society of America*, 49:1218–1231, 1971.

[28] C. R. Steele. Behavior of basilar-membrane with pure-tone excitation. *Journal of the Acoustical Society of America*, 55(1):148–162, 1974.

[29] M. Ulfendahl, S. M. Khanna, A. Fridberger, A. Flock, B. Flock, and W. Jger. Mechanical response characteristics of the hearing organ in the low-frequency regions of the cochlea. *Journal of Neurophysiology*, 76(6):3850–3862, 1996.

[30] K. E. Nilsen and J. Russell. The spatial and temporal representation of a tone on the Guinea pig basilar membrane. *Proceedings of National Academic Society*, 97(22):11751–11758, 2000.

[31] G. von Békésy. *Experiments in Hearing.* McGraw-Hill, New York, 1960.

[32] L. Robles and M. A. Ruggero. Mechanics of the mammalian cochlea. *Physiological Reviews*, 81(3):1305–1352, 2001.

[33] B. M. Johnstone, R. Patuzzi, and G. K. Yates. Basilar-membrane measurements and the traveling wave. *Hearing Research*, 22(1-3):147–153, 1986.

[34] K. Yamaguchi and H. Ohmori. Voltage-gated and chemically gated ionic channels in the cultured cochlear ganglion neurone of the chick. *Journal of Physiology*, 420:185–206, 1990.

[35] C. J. Kros. Physiology of mammalian cochlear hair cells. In P. Dallos, A. N. Popper, and R. R. Fay, editors, *The Cochlea*, Springer Handbook of Auditory Research. Springer-Verlag, New York, 1996.

[36] P. Dallos. The active cochlea. *Journal of Neuroscience*, 12:4575–4585, 1992.

[37] W. E. Brownell, C. R. Bader, D. Bertrand, and Y. Deribaupierre. Evoked mechanical responses of isolated cochlear outer hair cells. *Science*, 227(4683):194–196, 1985.

[38] P. Dallos, D. Z. He, B. N. Evans, and B. Clark. Dynamic characteristics of outer hair cell motility. In H. Duifhuis, J. W. Horst, P. van Dijk, and S. M. van Netten, editors, *Biophysics of Hair Cell Sensory Systems*, pages 167–174. World Scientific, Singapore, 1993.

[39] J. F. Ashmore. A fast motile response in Guinea-pig outer hair cells—the cellular basis of the cochlear amplifier. *Journal of Physiology (London)*, 388:323–347, 1987.

[40] D. C. Mountain and A. E. Hubbard. Rapid force production in the cochlea. *Hearing Research*, 42(2-3):195–202, 1989.

[41] A. E. Hubbard and D. C. Mountain. Hair cell forward and reverse transduction—differential suppression and enhancement. *Hearing Research*, 43(2-3):269–272, 1990.

[42] I. J. Russell and P. M. Sellick. Low-frequency characteristics of intracellularly recorded receptor potentials in Guinea-pig cochlear hair cells. *Journal of Physiology (London)*, 338:179–206, 1983.

[43] P. Dallos and M. A. Cheatham. Nonlinearities in cochlear receptor potentials and their origins. *Journal of the Acoustical Society of America*, 86(5):1790–1796, 1989.

[44] I. J. Russell, A. R. Cody, and G. P. Richardson. The responses of inner and outer hair cells in the basal turn of the Guinea-pig cochlea and in the mouse cochlea grown in vitro. *Hearing Research,* 22:199–216, 1986.

[45] J. Santos-Sacchi. On the frequency limit and phase of outer hair cell motility: Effects of the membrane filter. *Journal of Neuroscience,* 12:1906–1916, 1992.

[46] N. P. Cooper and W. S. Rhode. Mechanical responses to two-tone distortion products in the apical and basal turns of the mammalian cochlea. *Journal of Neurophysiology,* 78:261–270, 1997.

[47] M. A. Ruggero, N. C. Rich, S. S. Narayan, and L. Robles. Basilar membrane responses to tones at the base of the chinchilla cochlea. *Journal of the Acoustical Society of America,* 101(4):2151–2163, 1997.

[48] M. A. Ruggero, L. Robles, and N. C. Rich. Two-tone suppression in the basilar membrane of the cochlea: Mechanical basis of the auditory-nerve rate suppression. *Journal of Neurophysiology,* 68(4):1087–1099, 1992.

[49] A. L. Nuttal and D. F. Dolan. Two-tone suppression of inner hair cell and basilar membrane responses in the Guinea pig. *Journal of the Acoustical Society of America,* 93:393–400, 1993.

[50] S. T. Neely. Mathematical modeling of cochlear mechanics. *Journal of the Acoustical Society of America,* 78(1):345–352, 1985.

[51] S. T. Neely and D. O. Kim. An active cochlear model showing sharp tuning and high sensitivity. *Hearing Research,* 9(2):123–130, 1983.

[52] S. T. Neely and D. O. Kim. A model for active elements in cochlear biomechanics. *Journal of the Acoustical Society of America,* 79(5):1472–1480, 1986.

[53] R. S. Chadwick. What should be the goals of cochlear modeling? *Journal of the Acoustical Society of America*, 102(5):3054, 1997.

[54] C. D. Geisler. A cochlear model using feedback from motile outer hair cells. *Hearing Research*, 54:105–117, 1991.

[55] A. Hubbard. A traveling-wave amplifier of the cochlea. *Science*, 259:68–71, 1993.

[56] S. T. Neely. A model of cochlear mechanics with outer hair cell motility. *Journal of the Acoustical Society of America*, 94(1):137–146, 1993.

[57] C. D. Geisler. A realizable cochlear model using feedback from motile outer hair cells. *Hearing Research*, 68:253–262, 1993.

[58] P. J. Kolston, M. A. Viergever, E. de Boer, and R. J. Diependaal. Realistic mechanical tuning in a micromechanical cochlear model. *Journal of the Acoustical Society of America*, 86(1):133–140, 1989.

[59] C. R. Steele, G. Baker, J. Tolomeo, and D. Zetes. Electro-mechanical models of the outer hair cell. In H. Duifhuis, J. W. Horst, P. van Dijk, and S. M. van Netten, editors, *Proceedings of International Symposium on Biophysics of Hair Cell Sensory Systems*. World Scientific, Singapore, 1993.

[60] E. de Boer. On equivalence of locally active models of the cochlea. *Journal of the Acoustical Society of America*, 98:1400–1409, 1995.

[61] L. Voldrich. Mechanical properties of basilar membrane. *Acta Otolaryngologica*, 86(5-6):331–335, 1978.

[62] R. C. Naidu and D. C. Mountain. Longitudinal coupling in the basilar membrane. *Journal of Association for Research in Otolaryngology*, 2(3):257–267, 2001.

[63] T. S. A. Jaffer, H. Kunov, and W. Wong. A model cochlear partition involving longitudinal elasticity. *Journal of the Acoustical Society of America*, 112(2):576–589, 2002.

[64] L. Voldrich. Experimental and topographical morphology in cochlear mechanics. In E. de Boer and M. A. Viergever, editors, *Mechanics of Hearing*. Delft University Press, Delft, Netherlands, 1983.

[65] K. M. Lim. *Physical and Mathematical Cochlear Models.* Ph.D. thesis, Stanford University, Stanford, California, 2000.

[66] K. D. Karavitaki and D. C. Mountain. Experimental evidence does not support feed-forward outer hair cell forces. In *Association for Research in Otolaryngology MidWinter Meeting Abstracts*, 1999.

[67] Y. Raphael, M. Lenoir, R. Wroblewski, and R. Pujol. The sensory epithelium and its innervation in the mole rat cochlea. *Journal of Comparative Neurology*, 314:367–382, 1991.

[68] G. K. Yates. The basilar membrane nonlinear input-output function. In P. Dallos, C. D. Geisler, J. W. Matthews, M. A. Ruggero, and C. R. Steele, editors, *The Mechanics and Biophysics of Hearing*. Springer-Verlag, Berlin, 1990.

[69] A. E. Hubbard and C. D. Geisler. A hybrid-computer model of the cochlea partition. *Journal of the Acoustical Society of America*, 51:1895–1903, 1972.

[70] D. O. Kim, C. E. Molnar, and R. R. Pfeiffer. A system of nonlinear differential equations modeling basilar-membrane motion. *Journal of the Acoustical Society of America*, 54(6):1517–1529, 1973.

[71] J. B. Allen and M. M. Sondhi. Cochlear macromechanics—time domain solutions. *Journal of the Acoustical Society of America,* 66(1):123–132, 1979.

[72] C. D. Geisler and S. Greenberg. A two-stage nonlinear cochlear model possesses automatic gain control. *Journal of the Acoustical Society of America,* 80(5):1359–1363, 1986.

[73] R. J. Diependaal, H. Duifhuis, H. W. Hoogstraten, and M. A. Viergever. Numerical methods for solving one-dimensional cochlear models in the time domain. *Journal of the Acoustical Society of America,* 82(5):1655–1666, 1987.

[74] R. J. Diependaal and M. A. Viergever. Nonlinear and active two-dimensional cochlear models—Time-domain solution. *Journal of Acoustical Society of America,* 85(2):803–812, 1989.

[75] T. Fukazawa and Y. Tanaka. Spontaneous otoacoustic emissions in an active feed-forward models of the cochlea. *Hearing Research,* 95:135–143, 1996.

[76] J. L. Hall. Two-tone suppression in a nonlinear model of basilar membrane. *Journal of the Acoustical Society of America,* 61(3):802–810, 1977.

[77] C. D. Geisler. Two-tone suppression by a saturating feedback model of the cochlear partition. *Hearing Research,* 63(1-2):203–211, 1992.

[78] Y. D. Cai and C. D. Geisler. Suppression in auditory-nerve fibers of cats using low-side suppressors I: Temporal aspects. *Hearing Research,* 96(1-2):94–112, 1996.

[79] K. G. Hill. Basilar membrane motion in relation to two-tone suppression. *Hearing Research,* 115(1-2):129–142, 1998.

[80] C. Toumazou, J. Ngarmnil, and T. S. Lande. Micropower log-domain filter for electronic cochlea. *Electronics Letters,* 30(22):1839–1841, 1994.

[81] C. A. Mead. *Analog VLSI and Neural Systems*. Addison-Wesley, Reading, Massachusetts, 1989.

[82] A. van Schaik, E. Fragniére, and E. A. Vittoz. Improved silicon cochlea using compatible lateral bipolar transistors. In D. S Touretky, M. C. Mozer, and M. E. Hasselmo, editors, *Advances in Neural Information Processing Systems*, volume 8, pages 671–677. MIT Press, Cambridge, Massachusetts, 1996.

[83] E. Fragniére, A. van Schaik, and E. A. Vittoz. Design of an analogue VLSI model of an active cochlea. *Analog Integrated Circuits and Signal Processing*, 13(1-2):19–35, 1997.

[84] W. Germanovix and C. Toumazou. Design of a micropower current-mode log-domain analog cochlear implant. *IEEE Transactions on Circuits and Systems II: Analog and Digital Signal Processing*, 47(10):1023–1046, 2000.

[85] E. Fragniére. *Analogue VLSI Emulation of the Cochlea*. Ph. D. thesis, Swiss Federal Institute of Technology, Lausanne, Switzerland, 1998.

[86] A. van Schaik and E. Fragniére. Pseudo-voltage-domain implementation of a design of two-dimensional silicon cochlea. In *Proceedings of the IEEE International Symposium on Circuits and Systems*, volume 3, pages 185–188, 2001.

[87] H. Schmid. Why the terms current mode and voltage mode neither divide nor qualify circuits. In *Proceedings of the International Symposium on Circuits and Systems*, volume 2, pages 29–32, 2002.

[88] F. Kalinec and B. Kachar. Structure of the electromechanical transduction mechanism in mammalian outer hair cells. In Å. Flock, D. Ottoson, and M. Ulfendahl, editors, *Active Hearing*, pages 181–193. Pergamon, Kidlington, UK, 1995.

[89] B. Wen and K. A. Boahen. A linear cochlear model with active bi-directional coupling. In *IEEE Proceedings of the Engineering in Medicine and Biology Society Annual Conference*, pages 2013–2016, 2003.

[90] F. Mammano and J. F. Ashmore. Reverse transduction measured in the isolated cochlea by laser interferometry. *Nature*, 365:838–841, 1993.

[91] S. T. Neely. Finite-difference solution of a two-dimensional mathematical model of the cochlea. *Journal of the Acoustical Society of America*, 69(5):1386–1393, 1981.

[92] E. de Boer and E. Vanbienema. Solving cochlear mechanics problems with higher-order differential-equations. *Journal of the Acoustical Society of America*, 72(5):1427–1434, 1982.

[93] J. B. Allen. Two-dimensional cochlear fluid model: New results. *Journal of the Acoustical Society of America*, 61:110–119, 1977.

[94] M. M. Sondhi. Method for computing motion in a two-dimensional cochlear model. *Journal of the Acoustical Society of America*, 63:1468–1477, 1978.

[95] D. D. Greenwood. A cochlea frequency-position function for several species—29 years later. *Journal of the Acoustical Society of America*, 87(6):2592–2605, 1990.

[96] C. E. Liberman. The cochlear frequency map for the cat: Labeling auditory-nerve fibers of known characteristic frequency. *Journal of the Acoustical Society of America*, 72:1441–1449, 1982.

[97] N. Y. S. Kiang, T. Watanabe, E. C. Thomas, and L. F. Clark. *Discharge Patterns of Single Fibers in the Cat's Auditory Nerve.* MIT Press, Cambridge, Massachusetts, 1965.

[98] J. B. Allen and P. F. Fahey. A second cochlear-frequency map that correlates distortion product and neural tuning measurements. *Journal of the Acoustical Society of America*, 94:809–816, 1993.

[99] C. R. Steele and L. A. Taber. Comparison of WKB and finite-difference calculations for a two-dimensional cochlear model. *Journal of the Acoustical Society of America*, 65(4):1001–1006, 1979.

[100] E. de Boer and M. A. Viergever. Validity of the Liouville-Green (or WKB) method for cochlear mechanics. *Hearing Research*, 8(2):131–155, 1982.

[101] C. R. Steele and C. E. Miller. An improved WKB calculation for a two-dimensional cochlear model. *Journal of the Acoustical Society of America*, 68(1):147–148, 1980.

[102] G. Zweig, R. Lipes, and J. R. Pierce. Cochlear compromise. *Journal of the Acoustical Society of America*, 59(4):975–982, 1976.

[103] J. E. Gale and J. F. Ashmore. An intrinsic frequency limit to the cochlear amplifier. *Nature*, 389:63–66, 1997.

[104] E.-S. Hassan. A theoretical basis for the high-frequency performance of the outer hair cell's receptor potential. *Journal of the Acoustical Society of America*, 101:2129–2134, 1997.

[105] P. K. Legan, V. A. Lukashkina, R. J. Goodyear, M. Kossi, I. J. Russell, and G. P. Richardson. A targeted deletion in alpha-tectorin reveals that the tectorial membrane is required for the gain and timing of cochlear feedback. *Neuron*, 28(1):273–85, 2000.

[106] R. Pujol, M. Lenoir, S. Ladrech, F. Tribillac, and G. Rebillard. Correlation between the length of outer hair cells and the frequency coding of the cochlea. *Advances in the Biosciences*, 83:45–51, 1992.

[107] H. Spoendlin. Innervation densities of the cochlea. *Acta Otolaryngologica*, 73(2):235–248, 1972.

[108] T. L. Deliyannis, Y. Sun, and J. K. Filder. *Continuous-time Active Filter Design*. CRC Press, Boca Raton, Florida, 1999.

[109] G. W. Roberts and V. W. Leung. *Design and analysis of integrator-based log-domain filter circuits*. Kluwer Academic Publishers, Norwell, Massachusetts, 1999.

[110] W. K. Chen. *The VLSI Handbook*. CRC Press, Boca Raton, Florida, 2000.

[111] R. Sarpeshkar, R. F. Lyon, and C. Mead. A low-power wide-linear-range transconductance amplifier. *Analog Integrated Circuits and Signal Processing*, 13(1-2):123–151, 1997.

[112] D. R. Frey. Log-domain filtering: an approach to current-mode filtering. *IEE Proceedings - Part G: Electronic Circuits and Systems*, 140(6):406–416, 1993.

[113] O. Shana'a and R. Schaumann. Low-voltage high-speed current-mode continuous-time IC filters with orthogonal ω_0-Q tuning. *IEEE Transactions on Circuits and Systems II: Analog and Digital Signal Processing*, 46(4):390–400, 1999.

[114] C. Enz, M. Punzenberger, and D. Python. Low-voltage log-domain signal processing in CMOS and BiCMOS. *IEEE Transactions on Circuits and Systems II: Analog and Digital Signal Processing*, 46(3):279–289, 1999.

[115] P. R. Kinget. Device mismatch and tradeoffs in the design of analog circuits. *IEEE Journal of Solid-State Circuits*, 40(6):1212–1224, 2005.

[116] A. G. Andreou and K. A. Boahen. Translinear circuits in subthreshold MOS. *Analog Integrated Circuits and Signal Processing*, 9:141–166, 1996.

[117] M. Slaney. Lyon's cochlear model. Technical report, Apple Computer, Inc., 1988.

[118] J. C. Saunders, C. E. Ventetuolo, S. K.-R. Plontke, and B. A. Weiss. Coding of sound intensity in the chick cochlear nerve. *Journal of Neurophysiology*, 88:2887–2898, 2002.

[119] K. A. Boahen. Point-to-point connectivity between neuromorphic chips using address-events. *IEEE Transactions on Circuits and Systems II: Analog and Digital Signal Processing*, 47:416–434, 2000.

[120] K. A. Boahen. A burst-mode word-serial address-event channel-I: Transmitter design. *IEEE Transactions on Circuits and Systems I: Regular Papers*, 51(7):1269–1280, 2004.

[121] C. A. Mead and T. Delbrück. Scanners for visualizing activity of analog VLSI circuitry. *Analog Integrated Circuits and Signal Processing*, 1:93–106, 1991.

[122] M. Müller, D. Robertson, and G. K. Yates. Rate-versus-level functions of primary auditory nerve fibers: Evidence for square law behavior of all fiber categories in the guinea pig. *Hearing Research*, 55:50–56, 1991.

[123] A. Rodriguez-Vazquez, G. Linan, S. Espejo, and R. Dominguez-Castro. Mismatch-induced trade-offs and scalability of analog preprocessing visual microprocessor chips. *Analog Integrated Circuits and Signal Processing*, 37(2):73–83, 2003.

[124] S. Dusan and L. R. Rabiner. Can automatic speech recognition learn more from human speech perception? In C. Burileanu, editor, *Processdings of the 3rd Romanian*

Academy Conference on Speech Technology and Human-Computer Dialogue, pages 21–36, 2005.